Die approbierte Originalversion dieser Dissertation ist in der Hauptbibliothek der Technischen Universität Wien aufgestellt und zugänglich.
http://www.ub.tuwien.ac.at

The approved original version of this thesis is available at the main library of the Vienna University of Technology.
http://www.ub.tuwien.ac.at/eng

DISSERTATION

Sub-eutectic synthesis of epitaxial Si-nanowires using octachlorotrisilane as precursor

ausgeführt zum Zwecke der Erlangung des akademischen Grades eines
Doktors der technischen Wissenschaften

an der Technischen Universität Wien
Fakultät für Elektrotechnik und Informationstechnik
Institut für Festkörperelektronik, E 362
unter der Leitung von
O. Univ. Prof. Dr.phil. Emmerich Bertagnolli
und
Ao. Prof. Dipl.-Ing. Dr.techn. Alois Lugstein
durch
Dipl.-Ing. Wolfgang Molnar
Mat. Nr. 0225193
Wienerstraße 80b/2/42
2604 Theresienfeld

Wien, Mai 2014

I declare in the lieu of oath that I did this dissertation in hand by myself using only literature cited at the end of this volume.

Vienna, May 2014

. . . . . .Wolfgang Molnar

Abstract

Over the last decade demands from the electronic industry and its customers to create smaller and more powerful devices, have driven electronics into the nano scale. Nanowires (NW) provide an attractive possibility to meet requirements as building blocks for this rather new field of nano-electronics. Besides their tiny geometrical features, NWs also feature altered physical and chemical properties due to their high share of surface atoms. Specifically changes in light absorption, super paramagnetic behaviour, a lowered melting point and an altered chemical potential can be expected when producing NWs with diameters below 10 nm. Of course tailoring materials properties by adjusting its size can be an attractive way to design devices with novel properties.

Therefore the present work focuses on synthesis and characterisation of Si-NWs by atmospheric pressure chemical vapour deposition (APCVD) by using Si_3Cl_8 (OCTS) as a novel precursor. OCTS is a rather new precursor compared to the well established SiH_4, $SiCl_4$ or Si_2H_6, but it is doubtful that all of the future requirements will be met by only one of these precursors. Furthermore alternative catalysts to replace the most common and versatile Au are investigated as it introduces deep level traps into silicon, which deteriorates device performance considerably. Namely Al, Ag, Cu, In, Ni, Pt and Ti were tested with varying success.

In general an approach analogous to the well established Vapour-Liquid-Solid (VLS) mechanism was applied, although some catalysts like Cu and Ni tend to produce NWs via a Vapour-Solid-Solid (VSS) mechanism. Growth parameters like temperature, partial pressure of the precursor, gas feed composition, flow rates and sample preparation were investigated. Afterwards the NWs were examined by SEM and HRTEM, which included a crystallographic investigation of defects and growth orientation. All NWs grew along the [111] direction except for the Ni catalysed ones, which grew along [100] and [110], with Au, Pt and Ni also featuring epitaxy.

In later experiments also BBr_3 and PCl_3 were added to the precursor for growing in situ doped NWs. The addition of B accelerated precursor decomposition and resulted in deposition of a thick amorphous shell wrapped around the NW. Up to two third of a NW's diameters grown this way consisted of amorphous Si. Also the growth direction was changed to [112]. P on the other side reduced growth speed by blocking absorption spots on the catalyst, but also epitaxial NWs growing along the [112] direction were

achieved. Other catalysts were more severely affected by dopants than Au, thus either suppressed NW growth completely or at least prevented epitaxy.

In the last stages of this work NWs were characterized electrically. The resistivity strongly depends on the used catalyst: Cu ($7.8*10^4$ Ωcm) and Ni catalysed ($1.57*10^4$ Ωcm) NWs feature the highest resistivity, while Au lead to a resistivity of $5.96*10^3$ Ωcm, which is in range of values obtained in literature. Ag ($4.23*10^3$ Ωcm) and Pt ($9.72*10^2$ Ωcm) produced NWs with even lower resistivities. As expected doped NWs' resistivities were even lower with $1.98*10^{-1}$ Ωcm for B doped and $2.4*10^{-3}$ Ωcm for P doped ones.

Kurzfassung

Während der letzten 10 Jahre haben Forderungen der Elektronik-Branche und ihrer Kunden nach kleineren und leistungsfähigeren Geräten zur Erschließung des Nanometerbereichs geführt. Nanodrähte versprechen eine attraktive Möglichkeit zu sein den Anforderungen als Bausteine für diesen relativ neuen Bereich der Elektronik zu entsprechen. Neben ihrer geringen Größe verfügen NWs aufgrund ihres hohen Anteils an Oberflächen-Atomen über veränderte physikalische und chemische Eigenschaften. Im Detail können bei der Herstellung von NWs mit Durchmessern von 10 nm oder weniger Veränderungen bei Lichtabsorption, super paramagnetischem Verhalten, verringertem Schmelzpunkttemperaturen und geändertem chemischen Potentials erwartet werden. Natürlich ist es eine attraktive Möglichkeit, die Eigenschaften eines Materials anhand seiner Größe und Geometrie anzupassen und damit Bauteile mit sehr definiertem Verhalten zu erzeugen.

Daher konzentriert sich die vorliegende Arbeit auf Synthese und Charakterisierung von Si-NWs, die durch chemische Gasphasenabscheidung bei Atmosphärendruck (APCVD) mit Si_3Cl_8 (OCTS) als neuartigem Precursor erfolgt. OCTS ist im Vergleich zu den etablierten Precursorn SiH_4, $SiCl_4$ oder Si_2H_6 ein relativ neuer Precursor, aber es ist noch ungeklärt, ob alle zukünftigen Eigenschaften von einer einzigen dieser Chemikalien optimiert werden können. Außerdem werden in dieser Arbeit alternative Katalysatoren untersucht, um das vielseitige und bereits etablierte Au zu ersetzen, da dieses so genannte Deep Leevel Traps in Si induziert, was die Geräteeigenschaften eines Bauteils erheblich verschlechtert. Namentlich wurden Al, Ag, Cu, In, Ni, Pt und Ti untersucht.

Im Allgemeinen wird ein Ansatz analog zum populären Vapor-Solid-Solid (VLS) angewendet, einige Katalysatoren wie Cu und Ni tendieren aber dazu NWs über einen Vapor-Solid-Solid (VSS)-Mechanismus zu generieren. Wachstums Parameter wie Temperatur, Precursor-Partialdruck, H_2-Durchflussmengen und Probenvorbereitung werden untersucht. Danach werden die NWs mittels SEM und HRTEM charakterisiert, was eine kristallographische Untersuchung von Defekten und Wachstumsorientierung miteinschließt. Alle NWs, mit Ausnahme der Ni katalysierten, welche entlang [100] und [110] wachsen, wachsen in [111] Richtung; mit Au, Pt und Ni wurde auch epitaktisches Wachstum erzielt.

In weiteren Experimenten werden auch BBr_3 und PCl_3 der Wachstums-Atmosphäre für die Produktion von in-situ dotierten NWs hinzugefügt. Der Zusatz von B beschleunigt die Precursorzersetzung und führt zu einer dicken, amorphen Schale um den NW. Bis zu zwei Drittel des NW-Durchmessers besteht hierbei aus amorphem Si. Die Wachstumsrichtung änderte sich ebenfalls zu [112]. P andererseits reduziert die Wachstums-Geschwindigkeit durch die Blockierung von Absorptionsstellen. Auch epitaktische NWs in [112]-Richtung werden hier erfolgreich gewachsen. Andere Katalysatoren werden von den Dotierstoffen stärker betroffen als Au, da sie entweder das NW-Wachstum vollständig unterdrücken oder zumindest die Epitaxie verhindern.
In der letzten Phase dieser Arbeit werden die NWs elektrisch charakterisiert. Es ergiebt sich, daß der elektrische Widerstand stark vom verwendeten Katalysator abhängt. Cu ($7{,}8*10^4$ Ωcm) und Ni ($1{,}57*10^4$ Ωcm) katalysierte NWs verfügen über den höchsten elektrischen Widerstand, während Au einen Wert von $5.96*10^3$ Ωcm zur Folge hat, was sich im Bereich von Literaturwerten befindet. Ag ($4.23*10^3$ Ωcm) und Pt ($9{,}72*10^2$ Ωcm) produzierten NWs mit noch niedrigerem elektrischem Widerstand. Dotierte NWs weisen mit $1{,}98*10^{-1}$ Ωcm für B und $2{,}4*10^{-3}$ Ωcm für P den niedrigeren elektrischen Widerstand auf.

Acknowledgement

I would like to thank Dr. Alois Lugstein and Univ.-Prof. Dr. Emmerich Bertagnolli, Institute of Solid State Electronics, for let me work in the field of nanotechnology and their guidance during this work.

I would also like to thank the people in the research group who tried to help with their practical and theoretical repertoire, namely: DI Amra Avdic, DI Clemens Zeiner, Dr. DI Thomas Burchhart, DI Martin Hetzel, DI Johannes Greil, DI Ruppert Langegger, DI Markus Glaser, DI Karl Winkler, Florian Schmid, DI Florian Smecka and DI Stephan Wagesreither, which helped me a lot acquiring results and explanations.

Of course my thank goes also to every other member and staff of the TU Vienna, who assisted me.

Thank you!!!

Contents

1 Introduction 8
2 Theory 11
2.1 NW-Synthesis 11
2.1.1 Si-NW-synthesis techniques 11
2.1.2 VLS – growth mechanism 13
2.1.2 Phase diagrams 20
2.1.3 Solubility and catalyst incorporation in Si-NWs 24
2.1.4 Epitaxy and Orientation of VLS grown Si-NWs 26
2.1.5 Dependancy of a Si-NW's orientation and size on growth parameters 27
2.1.6 The precursor – Octachlorotrisilane (OCTS) 29
2.1.7 Doping of NWs 30
2.2 Electrical properties and characterisation of NWs 32
2.2.1 Schottky contact 32
2.2.2 p-n-junction 35
2.2.3 Real diode 38
2.2.4 Surface effects 40
2.2.5 In-situ doping of NWs 43
2.2.6 Electrical characterisation of Si-NWs 45
2.3 Transmission Electron Microscopy (TEM) 49
2.3.1 Principles of TEM 49
2.3.2 Thickness effects 53
2.3.3 Stacking faults 54
2.3.4 Twinning 55
3 Experimental setup 57
3.1 Atmospheric Pressure Chemical Vapor Deposition (APCVD) 57
3.1.1 APCVD-setup 57
3.1.2 APCVD-growth process 58
3.2 Sample preparation for TEM imagining 59
3.3 Electrical Characterization 60
3.4 Device processing of an in situ grown NW-diode 62
4 Results and Discussion 64
4.1 Au, Ag, Cu and Pt-catalysed Si-NW synthesis grown with OCTS 64
4.1.1 Au catalysed Si-NWs 64
4.1.2 Ag catalysed Si-NWs 71
4.1.3 Cu catalysed Si-NWs 73
4.1.4 Pt catalysed Si-NWs 75
4.1.5 Discussion of NW synthesis via Au, Ag, Cu and Pt mediated VLS-growth 77
4.1.6 NW synthesis via Au, Ag, Cu and Pt mediated VSS-growth 78
4.1.7 Al catalysed Si-NWs 80
4.1.8 Ti catalysed Si-NWs 81
4.1.9 In catalysed Si-NWs 82
4.1.9 Summary of OCTS grown and with Al, Ti and In catalysed Si-NWs 83
4.2 $NiSi_2$ catalysed Si-NWs grown with OCTS 84
4.2.1 Prismatic $NiSi_2$ catalysed NWs 87
4.3 Au, Cu, Ni and Pt catalysed Si-NW synthesis with BBr_3-doped OCTS 94
4.3.1 In-situ B doped Au catalysed Si-NWs with OCTS as precursor 94
4.3.2 In-situ B doped Cu catalysed Si-NWs 98
4.3.4 In-situ B doped Ni catalysed Si-NWs 102

4.4 Au, Pt and Ni catalysed NW synthesis with PCl_3-doped OCTS 104
4.4.1 In-situ P doped Au catalysed Si-NWs 104
4.4.2 In-situ P doped Pt catalysed Si-NWs 108
4.4.3 In-situ P doped Ni catalysed Si-NWs 110
4.5 Electrical properties of VLS-grown Si-NWs 113
4.5.1 Resistance and contact resistance of Si-NWs grown with pure OCTS 113
4.5.2 Specific resistivity and mobility of Si-NWs grown with pure OCTS 115
4.5.4 Electrical characterisation of Si-NWs grown with doped OCTS 119
4.5.5 Characterisation of an in-situ grown pn-diode 121
5 Conclusion 123
6 References 127

1 Introduction

Since the invention of the first transistor in 1947, customers and industry have continuously nourished the need for smaller and more powerful electronic devices of that kind. 1947 also marks the starting point of semiconductors as electronic materials, among which Si is the most prominent one today. Ten years later, in 1957, Treuting and Arnold [1] reported for the first time the growth of Si-NWs, called whiskers then. Although the NWs in their work were in the macroscopic range, it pushed open the door of nanosized semiconductor devices. Hence in 1964 Wagner and Ellis [2] discovered the Vapor-Liquid-Solid (VLS)-mechanism and achieved NWs as small as 100 nm. This strongly contributed to trigger an increased interest in whisker science (Figure 1, [3]).

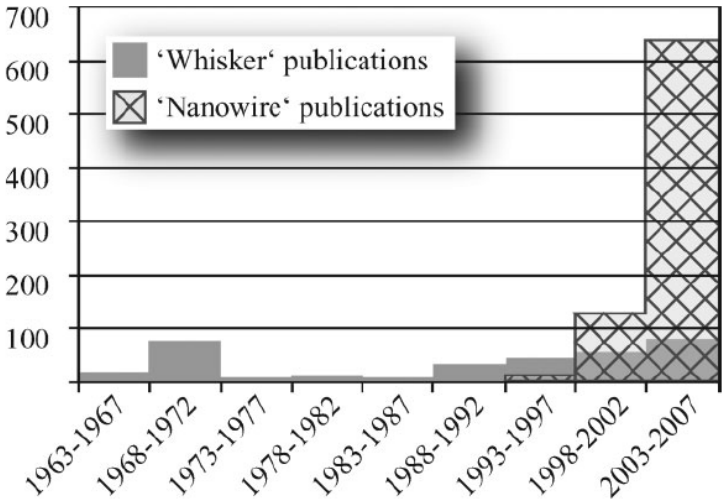

Figure 1: Histogram of NW and whisker related publications over the years [3].

The interest in NWs dropped in the following years and was revitalized in the mid 1990s by the electronic industry's new advances in microelectronics. Since then NWs have been a science topic with increasing grade of interest and although they are mainly valued for their electronic properties, which can be applied at nanoscale electronics [4], photonic devices [5] and solar cells [6]. NWs are today also attractive as potential materials for sensors [7], batteries [8] and catalysts [9] as well as applications in life science [10].

Currently electronic semiconductor devices are produced by top down techniques using optical lithography (down to 22 nm by 2012 on the commercial level). When reaching the nanoscale VIS (Visual spectrum)-lithography approaches its physical limits and the costs increase exponentially.

Another very attractive argument for NWs, or nanostructures in general, is a widening band gap at diameters below 10 nm. This leads to changes in physical and chemical properties such as absorption, fluorescence, electric properties and magnetic properties [11]. Needless to say such materials, whose properties depend on its size, can be tuned to a wide variety of applications. Up until now NW based electronics are just produced on the laboratory level, but nonetheless field-effect transistors, p-n junctions, bipolar junction transistors, complementary inverters and resonant tunneling diodes [12] have already been realized as prototypes to name a few examples.

To synthesize Si-NWs a wide range of methods is available. Among them are bottom up methods like chemical vapor deposition (CVD) [13], annealing in reactive atmosphere [14], thermal evaporation of SiO [15], Molecular Beam Epitaxy (MBE) [16], laser-ablation [17] and solution-based methods [18] as well as top down methods like catalytic etching [19] for example. Among these techniques CVD was chosen to produce NWs in this work, because of its extensive possibilities to tune growth parameters and the possibility to grow NWs at predesigned locations by utilizing the VLS mechanism.

When synthesizing a NW, its growth direction as well as its electrical and optical properties strongly depend on diameter [20], crystallographic orientation [21] as well as defect structure [22]. These characteristics on their part heavily depend on catalyst and precursor and it is therefore necessary to investigate a broad spectrum of both to achieve optimized NWs growth. Au for example, because of its low eutectic temperature with Si and its chemical inertness, the most common and best suitable catalyst for VLS growth causes undesirable deep level traps, which deteriorate NWs electrical and optoelectrical properties. So, alternative catalysts are also a subject of interest and various metals like Fe or Al [3] have so far successfully replaced Au as growth promoting catalyst. The same goes for new precursors, where SiH_4 [23], Si_2H_6 [24] and $SiCl_4$ [25] are currently the most common, but new precursors, like octachlorotrisilane (OCTS) are desired to broaden the spectrum of available NWs and to reduce costs and effort.

As already mentioned NWs are highly valued due to their electrical properties, which can be tuned in situ or ex situ, mostly by doping. For the VLS growth, doping agents can be introduced either by adding a dopant to the catalyst particle or to the precursor. A combination of Au/Sb has already been used to create p-doped Si-NWs for FETs [26], although it proved hard to control the dopant distribution in the NW. Much more common and effective it is to add a gaseous dopant, such as PH_3, B_2H_6 or $B(CH_3)_3$, to

the precursor gas during growth. For example p-i-n^+-type doped Si-NW-heterostructures have been achieved [27] with a resistivity of a few mΩ*cm. Unfortunately adding a dopand agent influences the growth behaviour. B for example accelerates the precursor decomposition, which causes an amorphous shell [28], whereas P decelerates the NW's growth rates or inhibits it completely at higher concentration [29]. Furthermore the doping often appears to be radially inhomogeneous and diameter dependent [30]. Although a lot of problems come along when doping NWs Cui et al. [31], T. Noda et al. [32] and J. R. Heath et al. [33] have successfully conducted electrical characterisations of SiH_4 or Si_2H_6 grown NWs, intrinsic as well as doped. Their work revealed a resistivity of 10^3 Ω*cm for intrinsic, unannealed NWs and much lower resistivity for doped ones. Some NW's resistivity was reduced to 10^{-3} Ω*cm. Considering all the possibilities outlined above, it is possible to tailor a NW's properties to an intended application and achieve the optimum solution for an electronic device.

2 Theory

2.1 NW-Synthesis

2.1.1 Si-NW-synthesis techniques

Numerous methods have proven to be suitable to grow Si-NWs. Such as chemical vapor deposition (CVD) [13], annealing in reactive atmosphere [14], thermal evaporation of SiO [15], Molecular Beam Epitaxy (MBE) [16], laser-ablation [17] and solution-based methods [18].

When working with a CVD process, a volatile precursor is intentionally decomposed by heat on a substrate to produce a desired deposit. The position of the deposit extends to all surfaces of the substrate and is therefore no directional process. Annealing in reactive atmosphere relies on a similar principle. The main difference between this method and classical CVD is that the substance intended for deposition forms in the atmosphere and then deposits on the substrate. Another related technique is thermal evaporation. In this case a solid precursor is thermally evaporated and then transported either by diffusion or convection to the desired place of deposition. MBE takes place in high or ultra high vacuum conditions, where a material e.g. gallium and arsenic is thermally heated in a Knudsen effusion cell until it sublimes. The resulting beam of gas then condenses onto the substrate forming NWs. The deposition rate allows epitaxial growth of single crystals or layers. Laser ablation is very similar to thermal evaporation, except that the evaporation is realized by a laser instead of a conventional heater. Solution based methods take place in liquids, where the precursor is deposited directly onto the substrate through guided chemical or electro-chemical reactions.

Schematics of these methods can be found in Figure 2.

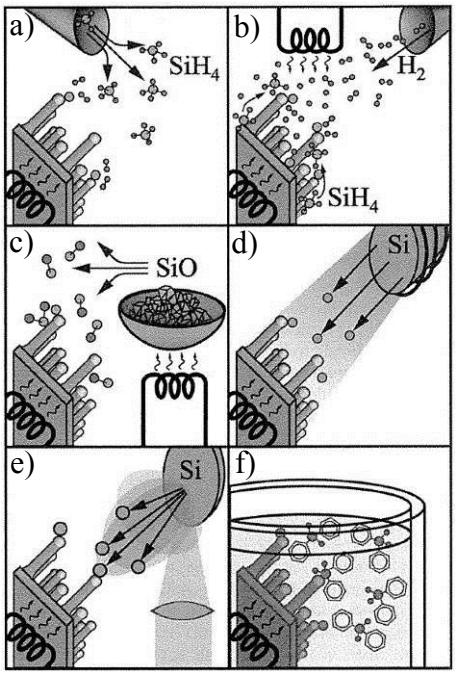

Figure 2: Schematics of experimental setups for Si-NW growth [3]:

a) CVD

b) Annealing in reactive atmosphere

c) evaporation of SiO

d) MBE

e) laser ablation

f) solution-based growth.

Among these approaches CVD was the method of choice for this work. CVD can be used to exploit several mechanism like: Vapor-Liquid-Solid (VLS) [2], Solid-Liquid-Solid (SLS) [34], the Solution-Solid-Solid (SSS) [35], the Vapor-Solid-Solid (VSS) [36], and the Oxide-Assisted-Growth (OAG) mechanism [37].

The VLS-mechanism is described later in detail as it is the primary focus for NW-growth in this work.

During the SLS-mechanism a liquid particle is utilized as catalyst, which absorbs Si from a solid substrate and subsequently a NW grows from this particle. No gas feed is necessary when using this mechanism, although it may improve the result.

The SSS-mechanism works very similar compared to the VLS-growth. The only difference is, that the gaseous precursor, which provides Si for the reaction in the VLS-mechanism, is replaces by a supercritical fluid.

In case of the VSS the catalyst remains in a solid state, from which then a NW precipitates. Otherwise it works analogously to the VLS-mechanism.

The OAG mechanism does not involve a metallic catalyst at all, but utilizes an oxide close to its solidification point to mediate precipitation of Si, what result in a Si-NW capped in an oxide shell.

2.1.2 VLS – growth mechanism

The VLS mechanism was discovered in 1964 by Wagner and Ellis to synthesise Si-NWs. The VLS-mechanism utilizes a liquid metal particle, which catalyses the decomposition of a Si containing precursor gas. Si is then dissolved into the droplet and subsequently a NW precipitates upon supersaturation. Concerning the catalyst, Au has been the most common choice for this approach as it provides a low eutectic temperature (363°C) and also low solubility of Si (18.6 % at eutectic point). The most common precursor gases for this purpose are SiH_4 [23] $SiCl_4$ [2] and Si_2H_6 [24], while Ag, Cu, In, Ni, Pt [38], Al [39], Au [2], Bi, Pb, Te, Zn [40], Cd, Gd, Mg, Mn, Os [41], Co, Pd [42], Dy, Fe [43], Ga [44] and Ti [45] have proven successful as catalysts so far. Determining the location of the NW by placing the particle at a desired position [46] is another advantage of the VLS-mechanism, thus offering great potential in matters of device integration. Another advantage of growing Si-NWs via VLS with a catalyst is the ability to control diameter and length by growth time and catalyst particle size [3].

The VLS-mechanism comprises mainly 3 steps (Figure 3):

a. Placing the metal particle on a suitable substrate at a desired location
b. Diffusion of the precursor to the liquid metal particle, discomposure and adsorption
c. Supersaturation and nucleation, followed by growth of the NW

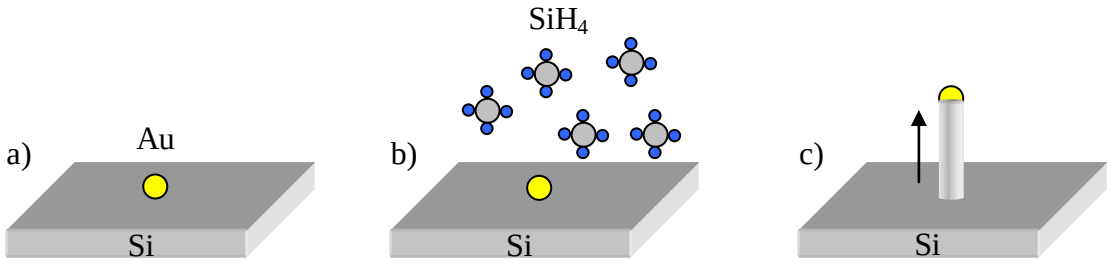

Figure 3: Schematic of the main steps of the VLS-mechanism:

a) Placing a metal particle on the substrate

b) Introducing Si-containing precursor gas, which dissolves into the particle

c) NW growth after supersaturation and nucleation.

2.1.2.1 Properties of the catalyst particle

In the first stage a metal particle is placed on the substrate by either using colloids with distinct diameters or applying a thin metal film which de-wets and forms droplets during heating. In the latter case surface tension (γ_{LV}) at the liquid-vapour-interface, molar volume (V_L), temperature (T) and gas saturation (p/p_{Eq}) are the determining factors for the size of the droplets to form (Equation {1}) [47], what determines the minimum radius (r_{min}) of the catalyst particle.

$$r_{\min} = \frac{2\gamma_{LV} V_L}{RT \ln\left(\frac{p}{p_{Eq}}\right)} \qquad \{1\}$$

Alternatively metal colloids can be used to secure a defined size for the catalyst particles. Irrespective of whether the VLS-mechanism is performed with an initial metal layer or with colloids, an alloy droplet will be formed due to increased temperature for growth. The angle between droplet and substrate will be established according to Equation {2} and Figure 4. The surface tension at the three interfaces (SV- Solid – Vapor, LS – Liquid – Solid and LV – Liquid – Vapor) determine the contact angle θ_C and therefore the size of the particle.

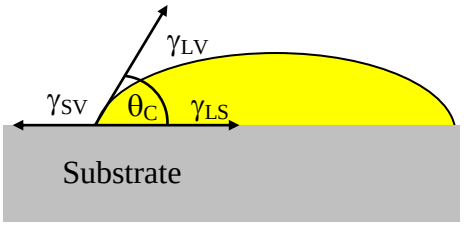

$$\gamma_{SV} = \gamma_{LS} + \gamma_{LV} * \cos\theta_C \qquad \{2\}$$

Figure 4: Contact angle θ_C, which is determined by surface tensions at the three interfaces close to the catalyst particle during VLS-growth.

If $0 < \theta_C < 90°$ ($\gamma_{LS} < \gamma_{SV}$) the droplet will wet the substrate and cover an area defined by Equation {2}. In case of $\theta_C > 90°$ ($\gamma_{LS} > \gamma_{SV}$), no wetting occurs and the droplet would practically roll over the substrate. Mercury on glass ($\theta_C = 140°$) is an example for that.

2.1.2.2 Gibbs-Thomson-Effect

For VLS synthesis of NWs, precursor gas is introduced into the CVD chamber, thermally cracked up and dissolved into the liquid catalyst particle. In case of the VLS-mechanism this happens above the eutectic temperature. For lower temperatures the particle remains solid, or softens up close to the melting point (T_m), and the process is then called Vapor-Solid-Solid (VSS) [36].

A very important aspect in this stage of the VLS-mechanism is the altered pressure within the metal droplet. When a droplet is in equilibrium with its ambience (p_{ex}) there is a certain pressure inside the droplet. This inner pressure (p_{in}), or sometimes called Kelvin pressure, thereby depends on the droplet's curvature. Since a droplet always tends to form a sphere the curvature indirectly depends on its radius (r). The Laplace equation (Equation {3}) describes this relation, what is usually referred to as the Gibbs-Thomson-effect.

$$p_{in} = p_{ex} + \frac{2\gamma}{r} \qquad \{3\}$$

The work of Nordiek [48] shows the difference between two extreme cases and is schematically explained in Figure 5. In the case of a plain boundary surface, or a very big droplet, the radius becomes practically infinite, what results in $p_{in} = p_{ex}$. A substance meeting these criteria exhibits a certain boiling point. When reducing this droplet's radius, the $2\gamma/r$ term increases and cannot be neglected anymore, what results in an

increased Kelvin pressure and as Figure 5 shows a decreased boiling point. So the increase in pressure can be extracted from Equation {3} as $\Delta p = 2\gamma/r$.

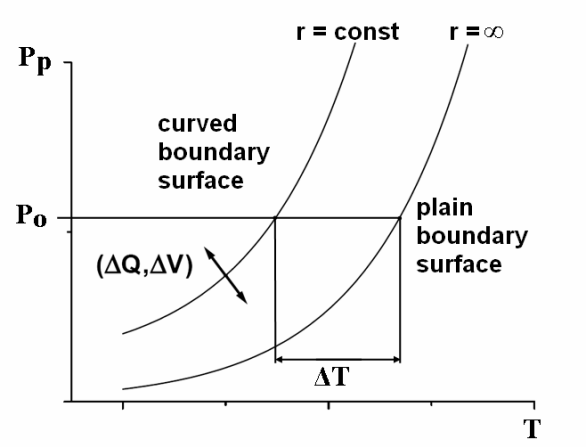

Figure 5: Illustration of the difference between a droplet and a plain boundary surface considering their inner pressures depending on temperature [48].

Another description of this phenomenon is Equation {4}; the Kelvin-equation. A special case of the Kelvin-equation is Equation {5} where $r_1 = r_2 = r$ describes a droplet encountered during the VLS-mechanism.

In practice p_{in}, often exceeds the value calculated by the Kelvin equation as it uses the ideal gas theory and is modelled for an incompressible liquid. Therefore $2\gamma/r >> \Delta p$ should be expected.

In case of the VLS-mechanism this also means, that the increased pressure inside the droplet impedes the solution of precursor material into the droplet. Hence the growth rate of smaller NWs is reduced because of the droplet's smaller size.

$$p_{in} = p_{ex} * e^{\frac{V_m \gamma \left(\frac{1}{r_1} + \frac{1}{r_2} \right)}{RT}} \quad \{4\} \qquad p_{in} = p_{ex} * e^{\frac{2\gamma V_m}{rRT}} \quad \{5\}$$

V_m	molecular Volume [m³/mol]
R	8.3144621 [J/K*mol]
r_1, r_2	principal radii of curvature [m]
γ	surface tension [N/m]

2.1.2.3 Nucleation and surface energies

During the third step Si is still dissolving into the metal droplet from the gas phase and until supersaturation is reached. After supersaturation nucleation is necessary to initiate NW-growth. The classic nucleation theory [49] offers a simple model to explain this process. Although microscopic particles are credited with the same properties as their macroscopic counterparts in this model, it is still very convenient to explain the process in general.

Like for every other process, nucleation only occurs spontaneously when the free Gibbs energy (ΔG) is negative. For spherical particles this is determined by two additive terms as depicted in Equation {6}. The first term describes the energy released by the addition of molecules/atoms to a nucleus by its shape ($4/3\pi r^3$ for spheres) and the difference in free energy between the liquid and solid state G_V, the volume free energy. The second term defines the energy that is needed to increase the nucleus' interface by its surface ($4\pi r^2$ for spheres) and surface tension γ, the interfacial energy. See also Figure 6 for a graphic illustration.

$$\Delta G = -\frac{4}{3}\pi r^3 G_V + 4\pi r^2 \gamma \qquad \{6\}$$

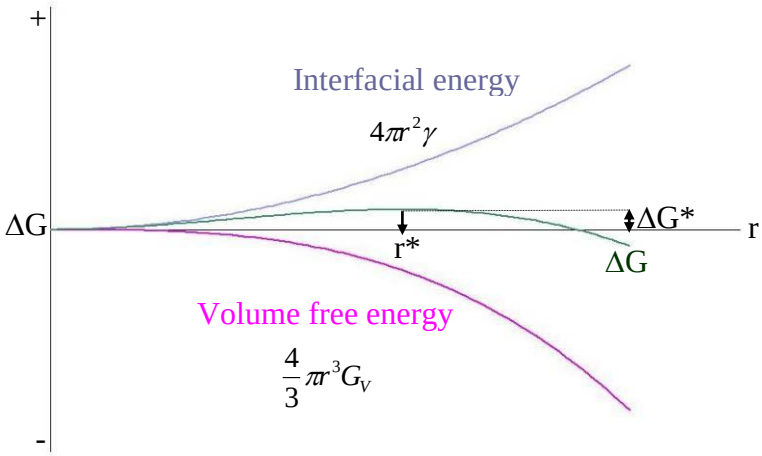

Figure 6: Critical nucleation radius in dependence of the Gibbs free energy after the classic nucleation theory for spheres.

At the onset of supersaturation the nuclei are very small and energy must be appended to add new molecules/atoms because dG/dr > 0. This applies until the particle reaches

the critical radius r*, when dG/dr = 0. r* is therefore defined by Equation {7} and the free energy ΔG_V needed to form a nucleus of that size is given by Equation {8}. At this point the probability for a nucleus to transform into a crystal is equal to that to collapse.

$$r^* = \frac{2\gamma}{G_V} \quad \{7\} \qquad \Delta G^* = \frac{16\pi\gamma^3}{3G_V^2} \quad \{8\}$$

When finally reaching the equilibrium point, ΔG becomes 0. In this case the free volume energy ΔG_V can be thermodynamically described as $\Delta G_V = \Delta H_V - T\Delta S_V$; with H_V (Enthalpy of fusion) and S_V (Entropy of fusion). When setting $T = T_m$ (melting temperature), ΔS_V is equal to $\Delta H_V/T_m$. If this is applied to Equation {7} and {8}, r* and G* can be described by the Equations {9} and {10}, with $\Delta T = T_m - T$.

$$r^* = \frac{2\gamma T_m}{\Delta H_V \Delta T} \quad \{9\} \qquad \Delta G^* = \frac{16\pi\gamma^3 T_m^2}{3\Delta H_V^2 \Delta T^2} \quad \{10\}$$

According to these equations, cooling to lower temperatures allows progressively smaller nuclei to become viable and hence smaller particles or NWs can precipitate.

The determining factor for deciding a NWs shape and orientation on a thermo dynamical base is its surface energy (γ) [50]. Taking into account a NWs length (L) and radius (r) γ can be described by Equation {11}.

$$\gamma = 2Lr\pi * \gamma_{SV} + r^2\pi * \gamma_{LS} + r^2\pi * \gamma_{SS} \quad \{11\}$$

Obviously γ depends strongly on the surface tensions of the 3 interfaces shown in Figure 7. Surface tension again depends heavily on temperature, as well as on the kind and concentration of molecules in the interface region [51, 52]. Therefore not only the chosen temperature, but also the substrate, the metal particle as well as pressure and composition of the growth atmosphere affect γ.

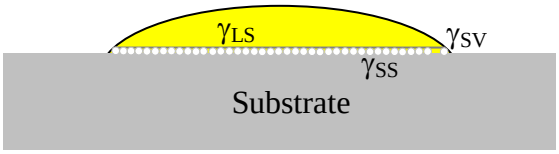

Figure 7: Schematic interface energies between a NW and the droplet with the first atomic layer of the NW precipitating. LS, SV and SS denote the three interface between the Vapor, Liquid and Solid parts of the system.

Possibilities to quantify the dependence of surface tension are represented by the Gibbs equation of surface tension and the Eötvös rule [51] (Equations {12} and {13}).

$$d\gamma = -\sum_J \Gamma_J d\mu_J \qquad \{12\}$$

$$\gamma = k(T_C - T - 6) * V^{-\frac{2}{3}} \qquad \{13\}$$

The Gibbs equation of surface tension considers the effect of surface active molecules on the interface by taking their concentration (Γ) and change in chemical potential (μ) into account. For the VLS-mechanism this means that molecules in the growth atmosphere can alter the surface tension of the metal droplet and therefore alter the surface energy of a NW by changing γ_{SV}. Equation {13} shows the dependency of γ on the temperature (T) by using the Eötvös-constant (k = $2.1*10^{-7}$ J K^{-1} $mol^{-2/3}$), critical temperature (T_C) and the molar volume (V).

2.1.2 Phase diagrams

It is generally accepted that the conditions for VLS growth of Si-NWs can be deduced from the binary phase diagrams involving the catalyst and Si. The Au/Si phase diagram (PD) in Figure 10a [53] represents a typical example. During VLS growth Si from a gaseous precursor is subsequently introduced into an initially pure droplet of Au. The exact process concerning phase transitions [51] is explained according to Figure 10b, a magnification of the relevant region in Figure 8a.

a_1:	At 500°C (typical for SiH_4 as precursor) the droplet still consists of pure Au.
a_1 to a_2:	Si dissolves into the droplet, what causes a part of it to melt. In this state the droplet consists of Au (s) and a liquid Au/Si mixture.
Slightly right of a_2:	The whole droplet is now a liquid mixture of Au and Si.
Slightly right of a_3:	Upon further incorporation of precursor gas solid Si precipitates from the droplet and forms a NW.

Alternative catalysts like Ag, Cu, Ni or Pt feature different phase diagrams like depicted in Figure 11 and Figure 10, which offer a more complicated mechanism and a high number of phases and transitions.

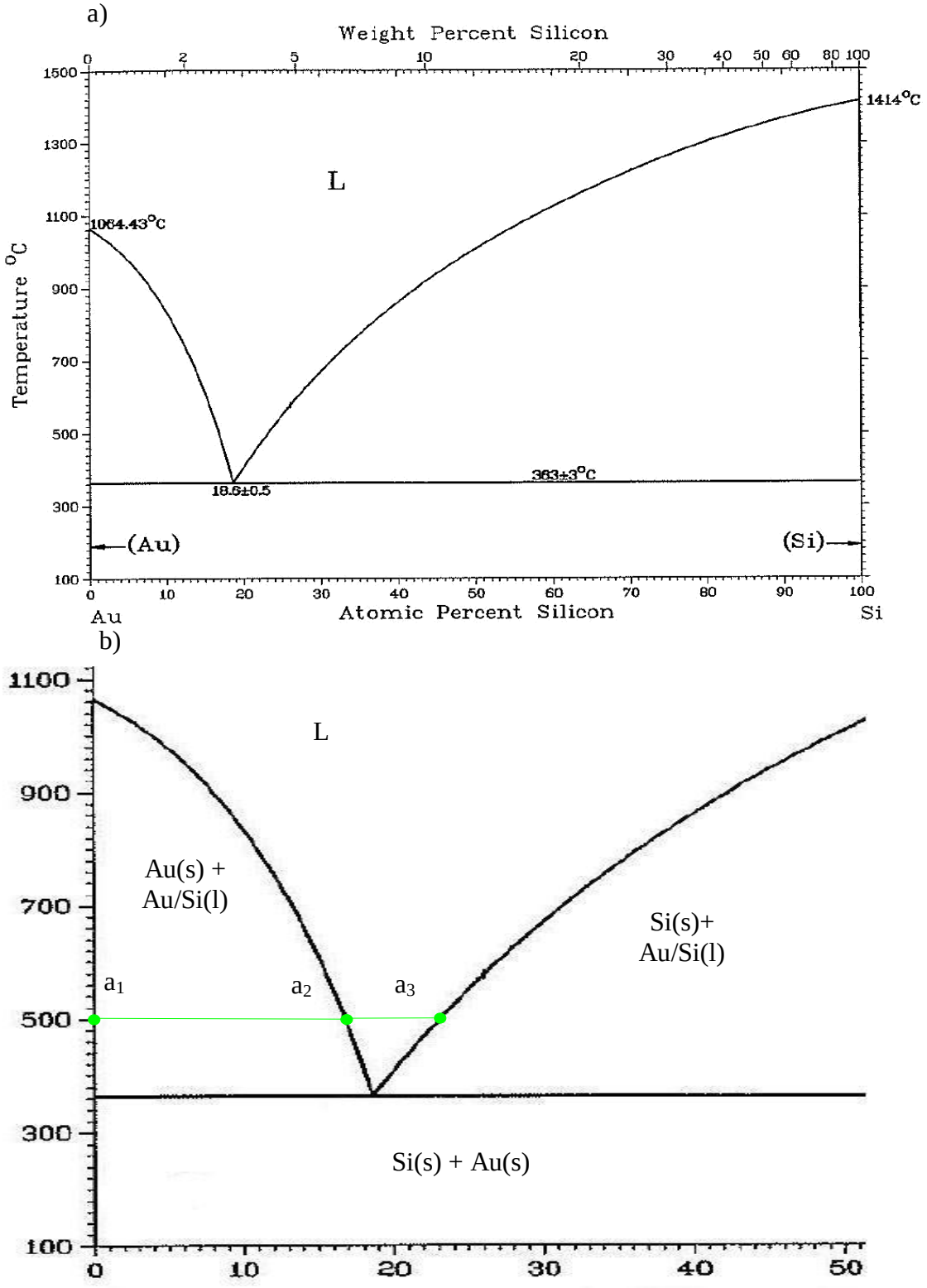

Figure 8: Binary phase diagrams of the system Au/Si (a) [53], which was investigated in this work. Diagram (b), an enlarged section of the Au/Si phase diagram serves for explanatory reasons.

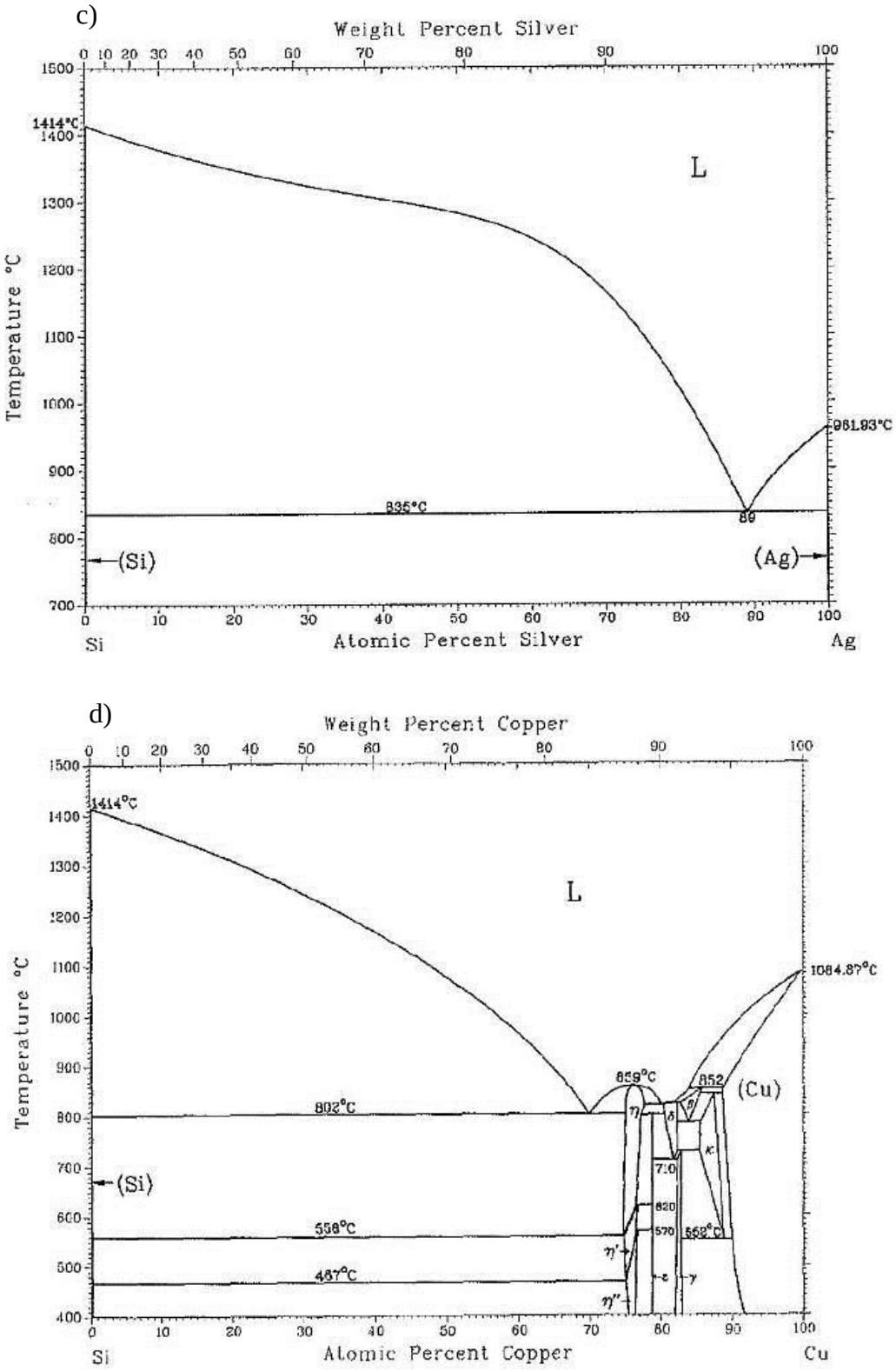

Figure 9: Binary phase diagrams of the systems Ag/Si (c) and Cu/Si (d) [53], which were investigated in this work.

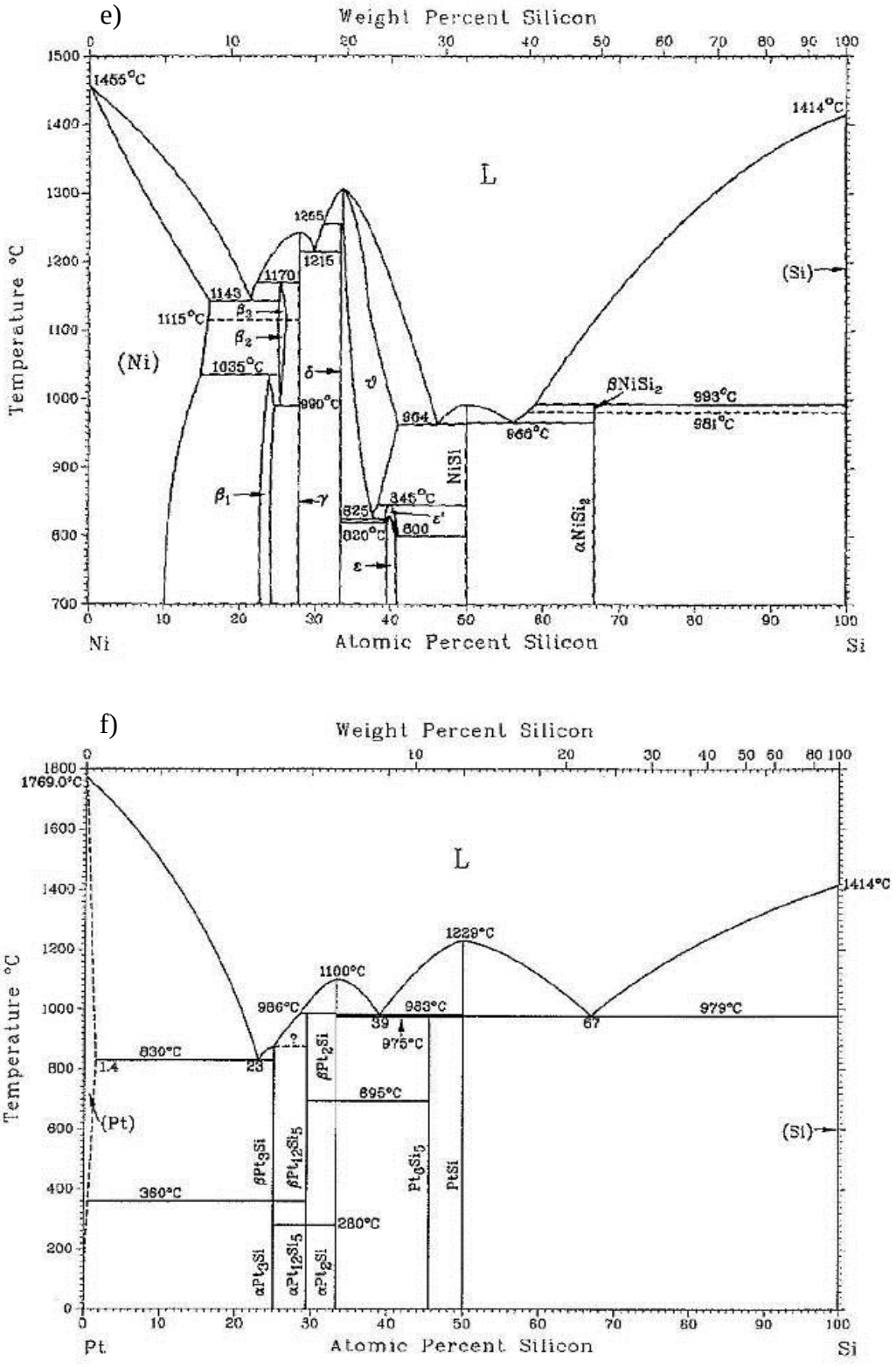

Figure 10: Binary phase diagrams of the systems Au/Si (a+b), Ag/Si (c), Cu/Si (d), Ni/Si (e) and Pt/Si (f) [53], which were investigated in this work.

When using a PD to explain or understand what happens to the catalytic droplet during VLS growth one should always keep in mind that it just concerns thermodynamic processes. Therefore kinetic and reaction state cannot be derived from a PD, but affect NW growth in nearly all practical experiments.

2.1.3 Solubility and catalyst incorporation in Si-NWs

During VLS growth it is inevitable that at least some metal from the catalyst particle gets incorporated into the NW during growth at elevated temperatures. Depending on the kind of impurity this can cause deep level defects with high charge carrier recombination rates. Figure 11 gives an impression of ionization energies of different catalyst materials in Si with respect to the band gap. The closer an impurity level is to the center of the band gap the more efficient it is as a recombination centre [3]. Unfortunately the most common VLS catalyst Au is one of that kind. For example, a concentration of 10^{17} Au atoms/cm³ decreases the lifetime of minority-carriers from $2*10^{-6}$ s to 10^{-10} s [54]. Therefore it is incompatible with complementary metal oxide semiconductor (CMOS) devices and most other electronic or opto-electronic devices. Nonetheless Au is still the most common VLS promoting catalyst due to:

- Chemical inertness
- Low solubility of Si
- Low vapour pressure at growth temperature
- Low eutectic point with Si
- Catalytic activity for precursor decomposition

Another important aspect for a catalyst is its solubility in Si as it determines the incorporated amount in the NW. Since the metal's solubility in Si rises with increasing temperature - except for very high temperatures above 1300°C [55] - lower growth temperatures are favoured. Furthermore, low grow temperatures are beneficial for device integration. Table 1 gives the solubility of Au in Si according to the temperature in the region from 600°C to 900°C.

Table 1: Solubility of Au in Si at temperatures between 600°C and 900°C [55]

T [°C]	Solubility [cm^{-3}]
600	$5.4*10^{12}$
700	$6.9*10^{13}$
800	$5.8*10^{14}$
900	$3.4*10^{15}$

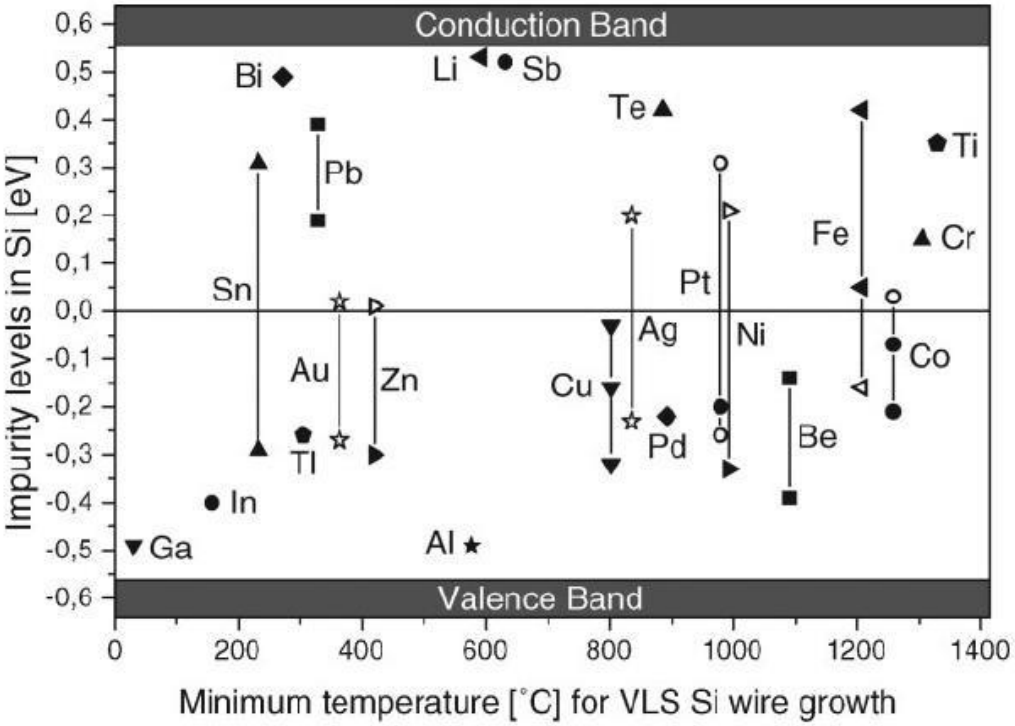

Figure 11: Ionization energies of various impurities in Si with respect to the midgap of the band gap (Si =1.12 eV). On the x-axis the minimum temperature necessary for VLS growth is displayed. Solid symbols above the band gap middle represent donor levels, while open symbols represent acceptor levels. Below the band gap middle solid symbols denote acceptor and open symbols denote donor levels [3].

2.1.4 Epitaxy and Orientation of VLS grown Si-NWs

Controlling epitaxy, crystallographic orientation and location of a NW have drawn considerable attention during the last decade as it offers a great potential in device integration. Epitaxy basically means that a NW adopts an orientation of the crystalline substrate. Via the VLS-growth this has been another point of interest as it provides an interesting possibility to arrange NWs on a crystal substrate in desired orientations for device integration [56]. Figure 12 shows in this context the orientations of the most common Si-NWs grown on a (111) oriented Si-substrate synthesized via VLS growth. Crucial parameters to determine a NW's orientation and epitaxy are total pressure [57], partial pressure of the precursor [58], the NW's diameter [59], growth direction and pre-treatment of the substrate [60, 61] and of course temperature [60]. Of course all of these parameters are directly influencing the surface tension γ, what makes it a determining factor in NW-synthesis.

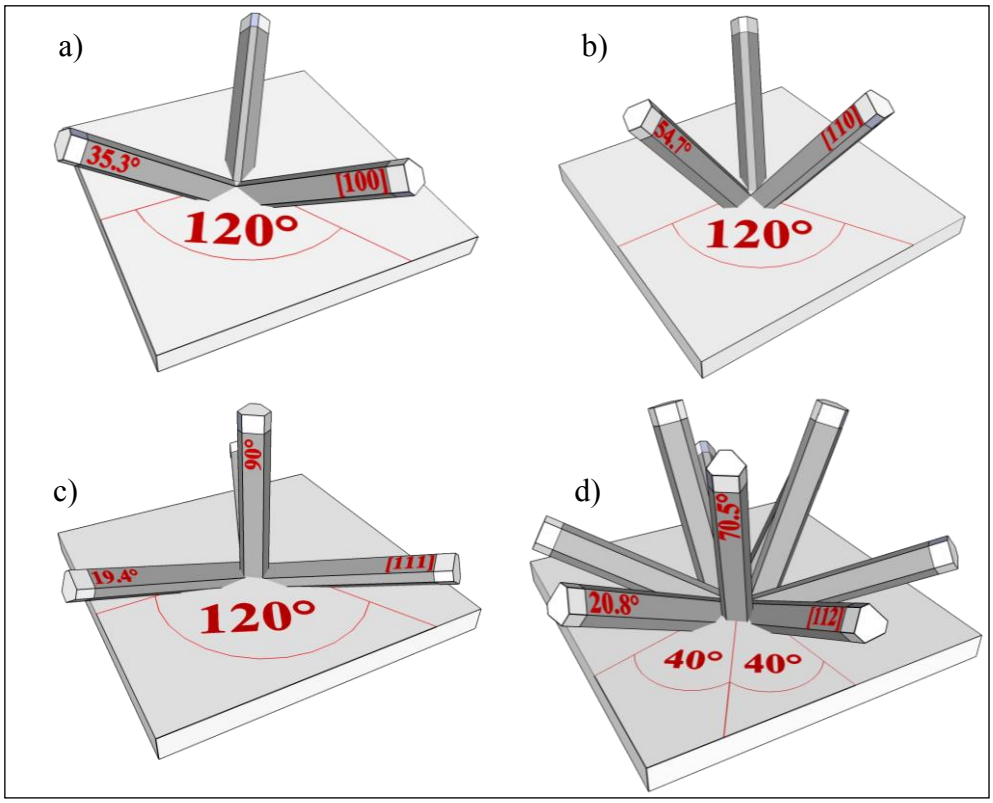

Figure 12: Calculated orientations of epitaxially grown Si-NWs grown a (111)-Si-substrate with their respective angles and azimuths:

a) [100] b) [110]

c) [111] c) [112]

Figure 12a shows the [100] oriented Si-NWs on a (111) substrate with an azimuth of 120° between the wires and an angle of 35.3° to the substrate. The [110] oriented Si-NWs (Figure 12b) show the same azimuth of 120° as the [100] oriented ones, but an angle of 54.7° with respect to the substrate. [111] oriented Si-NWs (Figure 12c) feature 4 growth directions. 3 of these directions are aligned with an azimuth of 120° to each other and an angle of 19.4° to the substrate, while the fourth grows perpendicular to the substrate in an angle of 90°. The [111] growth orientation is the only possibility to grow upright Si-NWs on a (111) substrate. Finally the [112] orientation (Figure 12d) exhibits 9 growth directions with an azimuth of 40° between the NWs. 3 direction show an angle of 70.5° to the substrate and 6 are aligned at an angle of 20.8° to the substrate; distributed according to Figure 12d.

2.1.5 Dependancy of a Si-NW's orientation and size on growth parameters

Figure 13 gives a good impression of the dependence of a NW's orientation on diameter, temperature and partial pressure of the precursor. Schmidt et al. [59] showed that the orientation the NW obtains during growth is dependent on its diameter (Figure 13a). At diameters from 10 to 20 nm [110] oriented NWs are dominating, although [112] and [111] oriented NWs can still be found. At higher diameters [111] oriented NWs are increasingly favoured. [112] NWs are present at diameters up to 35 nm, but are not dominating the numbers at any diameter. It should be noted, that these results were taken under certain conditions and therefore should not be generalised.

Another important relationship was investigated by Westwater et al. [13], which is displayed in Figure 13b. This figure displays the habitus of a Si-NW depending on partial pressure of the precursor, in this case silane, and growth temperature. High silane partial pressures favour the formation of kinks, as do low temperatures. To produce a straight NW, high temperatures and low partial pressure are necessary, although these results should not be generalised as they were obtained under certain conditions. This dependence was exploited by Tian et al. [62], who produced zig-zag Si-NWs by variation of the partial pressure and therefore forced the NW to change growth orientation during. The thickness of the NWs indicated in Figure 13b does not directly depends on the amount of precursor available during the process. Otherwise the NWs at

600°C with the lowest partial pressure would be the thinnest. The diameter of a NW is directly determined by the size of the catalyst particle, from which the NW nucleates. The particle size on the other hand is determined by its contacts angle, which depends on the surface tension γ. Like discussed before γ depends on temperature, the molecules on the three interfaces and of course, the chemical composition of the catalyst particle itself. So therefore a NW's shape and orientation mainly depend on the surface tension γ.

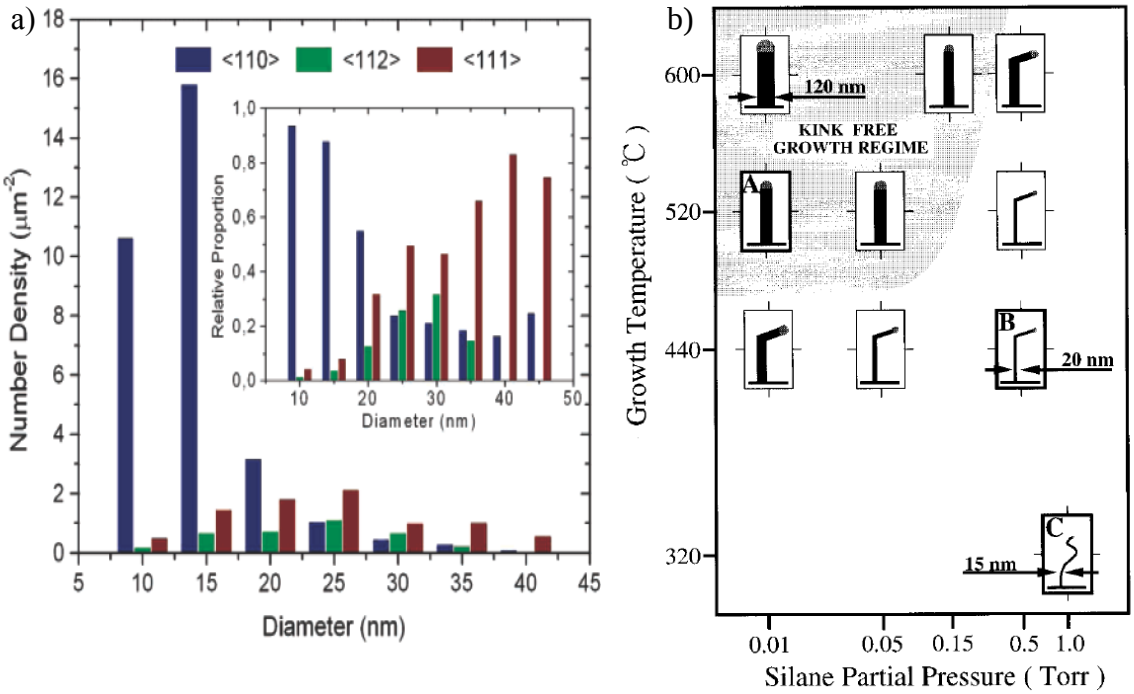

Figure 13: a) Orientation dependence and frequency of occurrence on a NW's diameter of Si-NWs grown on Si (111) substrate [59].
b) Dependance of a Si-NW's morphology on temperature and partial pressure of the precursor [13].

For practical growth applications, it should be mentioned that even the condition of the reaction tube can alter growth behaviour. In case of a new, clean reaction tube, more precursor would be deposited on the sidewall and the precursor's partial pressure would be lower in comparison to later experiments, where the sidewall is already covered [63]. Also metallic remainders on the tube wall, like In, have been reported to influence growth during subsequent runs [64].

Although so many parameters, of which some are hard to quantify, make it difficult to choose the right setup, it offers an excellent chance of tuning a NWs' properties. In this context Sunkara et al. [65] have shown that Ga catalyses the growth of [100] oriented

Si-NWs by utilizing the VLS mechanism in a microwave plasma reactor. Gösele et al. [39] achieved growth of [111] oriented Si-NWs with Al via VSS growth; however requiring UHV conditions. An approach with Pt was shown by Baron et al. [66] leading also to [111] oriented Si-NWs catalysed by PtSi islands. Using Ag particles of different size Wittemann et al. [67] achieved Si-NWs of [110], [111] and [112] orientation on a (100) oriented substrate. Finally Morral et al. [68] have utilized Cu, leading to VSS-grown [110] and [1210] oriented Si-NWs with diamond and even wurtzite structure within the same NW.

2.1.6 The precursor – Octachlorotrisilane (OCTS)

Many precursors, like the before mentioned SiH_4 [23], $SiCl_4$ [2] and Si_2H_6 [24], are currently used in CVD related Si-NW synthesis methods, but for this work octachlorotrisilane (OCTS, Si_3Cl_8) was chosen. In comparison to other common precursors, OCTS offers 3 Si-atoms per molecule, thus promising high growth rates at low partial pressures. It also features a more easily to break Si-Si bond (74.8 kcal/mol) than SiH_4 with its stronger Si-H bond (91.8 kcal/mol) or $SiCl_4$ with the even stronger Si-Cl bond (110 kcal/mol) [69]. Even Si_2H_6 features slightly higher dissociation energy (76.7 kcal/mol) than OCTS (see Figure 14).

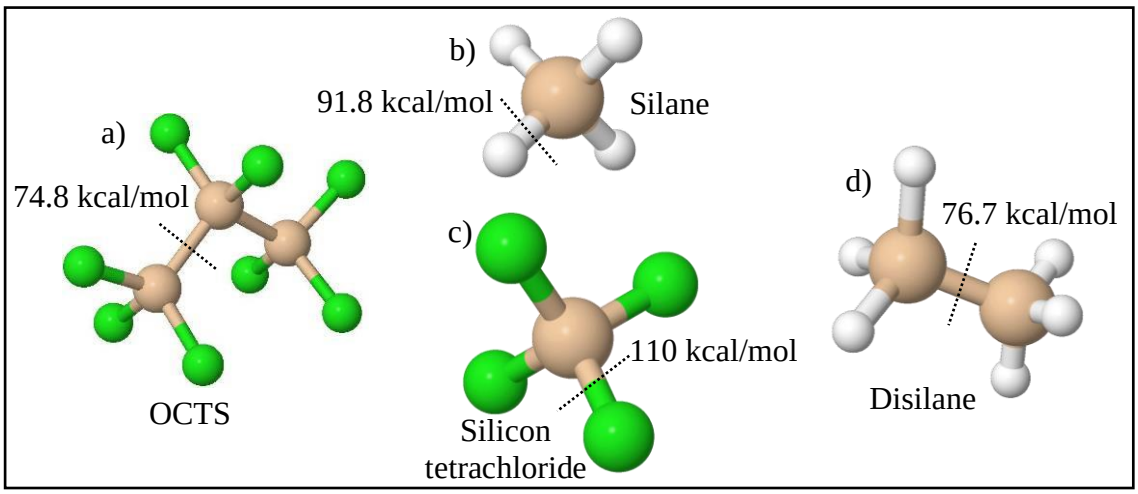

Figure 14: Schematics and dissociation energies of some Si-precursor molecules after Walsh et al. [69]. a) OCTS, b) SiH_4, c) $SiCl_4$ and d) Si_2H_6; drawn in ChemSketch.

Thermodynamic simulations concerning the stability of OCTS were conducted by Ezhov et al. [70] and revealed that OCTS is already decomposing at 550 K, although noticeable decomposition does not start until 900-1000 K. According to dissociation energies and the work of Ezhov the following decomposition mechanism is proposed.

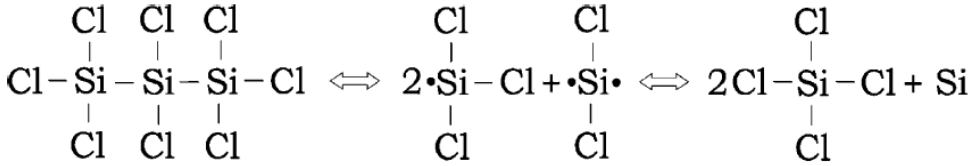

Also in contrast to more common precursors, OCTS is a liquid at room temperature (T_B = 487 K). Hence a saturator with carrier gas is necessary to introduce it into the growth atmosphere, as it shows sufficient partial pressure at room temperature (~0.03 mbar, Figure 15) [71].

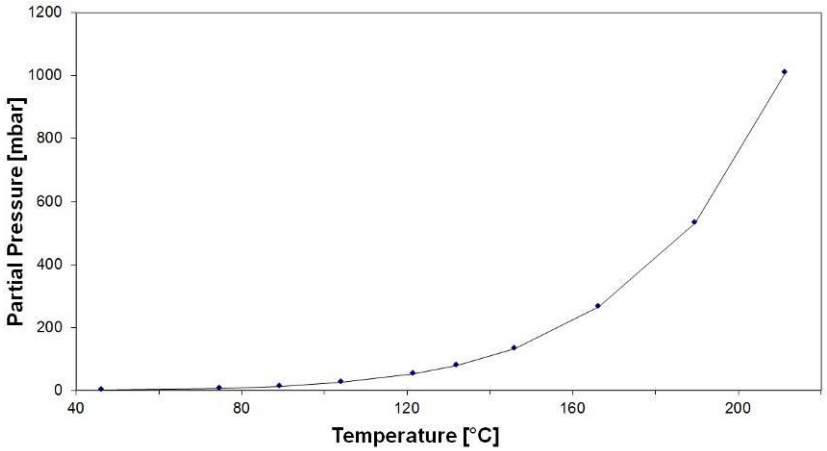

Figure 15: Partial pressure of OCTS as a function of temperature after Martin [71].

2.1.7 Doping of NWs

Doping of Si generally means the introduction of impurities of group III (B)- or V-elements (P, As) to alter its electrical properties. This can be done in-situ (during growth) or ex-situ (after growth) by implantation or diffusion doping. Ion implantation is a technique, which is usually used ex-situ and will therefore not be discussed in this context. In-situ doping of impurities into the NW can happen in several ways. One way would be to use a metal catalyst like In [72], Al [72] or Ga [44], which typically incorporates itself during growth and works as a p-type dopant. Also adding a small amount of dopant to the catalyst particle can serve the purpose [33], although it is problematic to control the dopant distribution. Other methods attempt to incorporate the

dopant by co-evaporation during MBE [73] or co-ablation for NW growth via laser ablation [74]. For the APCVD-method used in this work the most common doping method is to introduce the dopant via an additional gaseous precursor during growth. Theoretically doping using donors and acceptors can cause concentrations ranging from 10^{13} up to 10^{21} atoms/cm³. However, in situ doping can not only alter electrical properties, but also growth behaviour considerably. With Si-NWs the addition of B_2H_6 results in an amorphous Si-shell, which can account for up to 2/3 of the NW's diameter [75]. In classical CVD n-dopants like P block the free surface sites on the silicon substrates, where usually SiH_4 molecules would be absorbed [76], and therefore reduce growth rates. Schmid et al. [58] have determined that PH_3 reduces a NW's growth rate by roughly 8% independently of its diameter. At a PH_3/SiH_4 ratio of $2*10^{-3}$, epitaxy is affected and a further increase of the PH_3 concentration leads to a total inhibition of Si-NW nucleation. Similar observations of growth rate reduction were made by Schmid when using AsH_3 as dopant. In this case also a change in surface tension of the Au droplet was observable, so the reduction in growth rate may not be solely attributed to As blocking absorption spots on the catalyst droplet.

Another important aspect of in situ doped NWs is the dopant distribution. Therefore Koren et al. [77] have investigated the radial donor concentration of a Si-NW by subsequent etching and Kelvin probe force microscopy (KPFM, Figure 16). KPFM is a variation of atomic force microscopy to determine the work function of surfaces. A tendency of dopant atoms, like B and P, to diffuse to the surface was confirmed this way. In another work Peelaers et al. [78] calculated this phenomenon by using ab initio studies. They revealed a segregation of dopant atoms close to the surface, where dopant atoms can be trapped and even electrically inactivated. This effect intensifies for thinner NWs as the ratio of surface to bulk atoms increases.

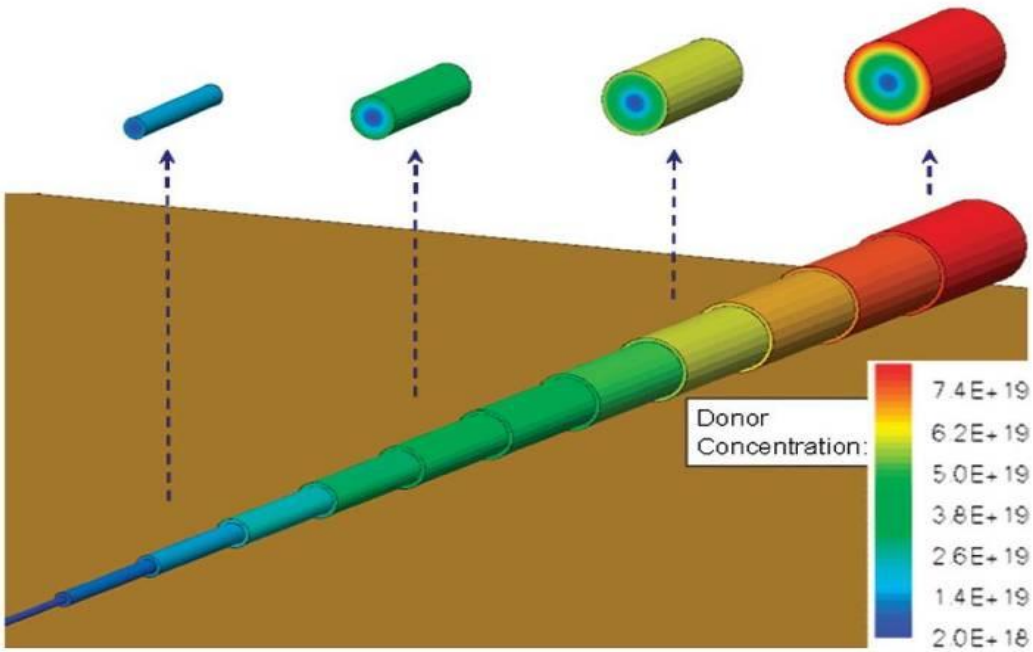

Figure 16: Inhomogeneous dopant distribution in a Si-NW [77] determined by KPFM. The NW was prepared by a combination of etching and lithography to create a stepwise thinning for dopant concentration investigation.

2.2 Electrical properties and characterisation of NWs

2.2.1 Schottky contact

If a metal and a semiconductor are brought in close contact a barrier will form. To explain this phenomenon Schottky [79] proposed a model for calculating the barrier height and shape (see Figure 17). When the length of the space charge region δ is infinite (as depicted in Figure 17a), metal and semiconductor are defined by their work functions $q\phi_m$ and $q\phi_S$ ($=qV_n+q\chi$) respectively. Here qV_n represents the difference of Fermi level and conduction band (E_C), while $q\chi$ (electron affinity) is the difference between E_C and the vacuum E_{VAC}. The difference between ϕ_m and ϕ_S is called contact potential. If δ decreases, an increasing negative charge is built up on the metal surface and a corresponding positive charge in the semiconductor. As there is a low carrier concentration in the semiconductor to begin with, electrons from the metal start to recombine with positive charge carriers close to the contact interface. So a depletion zone (W) forms and the energy bands are bent according to Figure 17b. Also E_F of metal and semiconductor align to each other due to diffusion of electrons. If δ decreases further to atomic distances, the gap becomes transparent for electrons. In this case the

barrier height for electrons can be defined by Equation {14} (n-type) or Equation {15} (p-type), and therefore $q\phi_B$ solely depends on ϕ_m.

$$q\phi_{Bn} = q(\phi_m - \chi) \quad \{14\} \qquad q\phi_{Bp} = E_g - (\phi_m - \chi) \quad \{15\}$$

δ	Length of the space charge region [m]
ϕ_m	Work function of the metal [J]
ϕ_S	Work function of the semiconductor [J]
V_n	Difference between conduction band and Fermi Level [J]
χ	Electron affinity [J]
E_C	Conduction band [J]
E_{VAC}	Energy of the vacuum level [J]
E_F	Fermi energy level [J]
E_V	Energy of the valence band [J]
W	Length of the depletion zone [m]

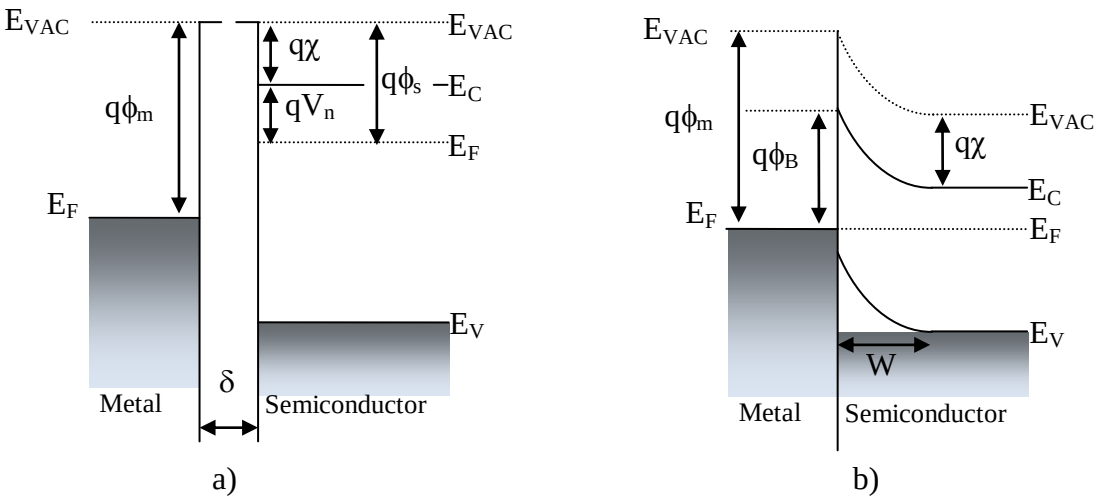

Figure 17: a) Energy band positions in a metal and semiconductor with $\delta = \infty$.

b) When δ reaches atomic scale a metal/semiconductor contact is established, leading to the formation of a Schottky barrier. In an ideal contact, $q\phi_B$ denotes the Schottky barrier height and W the length of the depletion zone.

In this context the minimum energy for an electron at the Fermi level to escape into the vacuum is defined by the metal's work function $q\phi_m$, usually 2 to 6 eV for metals. If this electron is brought to a distance x from the metal, a positive charge will be induced on the metal's surface, the image charge. The attractive force, the image force, that exists between electron and image charge is given by Equation {16}, where ε_0 is the permittivity of free space.

$$F = -\frac{q^2}{16\pi\varepsilon_0 x^2} \qquad \{16\}$$

The work of an electron that is transferred from infinity to a distance x from the metal is thus given by Equation {17}.

$$E(x) = \int_{\infty}^{x} F dx = \frac{q}{16\pi\varepsilon_0 x} \qquad \{17\}$$

If an external field ξ is present the total potential energy is given by Equation {18}.

$$E_P(x) = \frac{q^2}{16\pi\varepsilon_0 x} + q\xi x \qquad \{18\}$$

When an electron is approaching the metal-semiconductor interface, an image charge builds up. The potential associated with these charges reduces the effective barrier height, what is called Schottky barrier lowering or sometimes image force lowering. In this case the potential energy can be altered considerable by a single electron, although the depletion region contains more charge. The reason for this lies in the distribution of the charges inside the depletion layer. A single electron is far enough away from the other charges in the semiconductor to be considerably influenced by the potential energy of all the other charges.

In this case the maximum potential energy of a single electron reaches its maximum, due to the ionized donors, at x_{max} (Equation {19}). The Schottky barrier height lowering ($\Delta\phi_B$) in this case can be calculated by Equation {20}.

$$x_{\max} = \sqrt{\frac{q}{16\pi\varepsilon_0\xi}} \quad \{19\} \qquad \Delta\phi_B = \sqrt{\frac{q\xi}{4\pi\varepsilon_0}} = 2\xi x_{\max} \quad \{20\}$$

All this is valid for an ideal Schottky contact, what is not well supported by experimental data due to surface effects on the semiconductor like dangling bonds, defects or impurities. This deviation from ideal Schottky behaviour is usually described as "Fermi level pinning". In this case the barrier height is no longer solely dependent on ϕ_m, it is also affected by the charge neutrality level (ϕ_{CNL}) according to $q\phi_B=(d\phi_B/d\phi_m)*(\phi_m-\phi_{CNL})+(\phi_{CNL}-\chi_S)$ [80]. Depending whether the CNL is positioned above or below E_F, a negative or positive charge is built up at the interface respectively. In most cases E_F is located above CNL and a large negative charge is generated, what degrades NMOS technology performance by Coulomb scattering and charge trapping [81].

2.2.2 p-n-junction

Because of its rectifying behaviour, a p-n-junction is one of the basic elements of semiconductor technology. Applied in diodes, transistors and solar cells, it basically consists of a p-doped region adjacent to an n-doped region (Figure 18). Depending on the doping technique the profile can be continuous (diffusion) or abrupt (MBE, alloying). Due to the high difference of electric carrier concentrations between these regions, a gradient forms at the border by diffusion currents; the space charge region δ. As the total charge of the space charge region is 0, there has to exist an electric field, that induces a current equal to the diffusion current: the drift current.

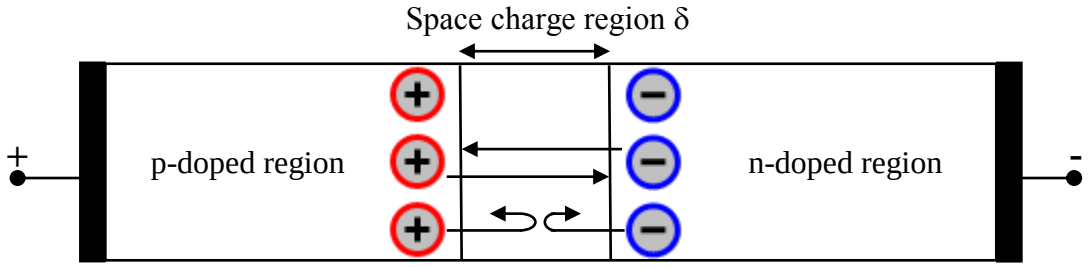

Figure 18: Schematic illustration of a p-n-junction with space charge region δ; U=0 V. The charge carriers experience a dynamic equilibrium.

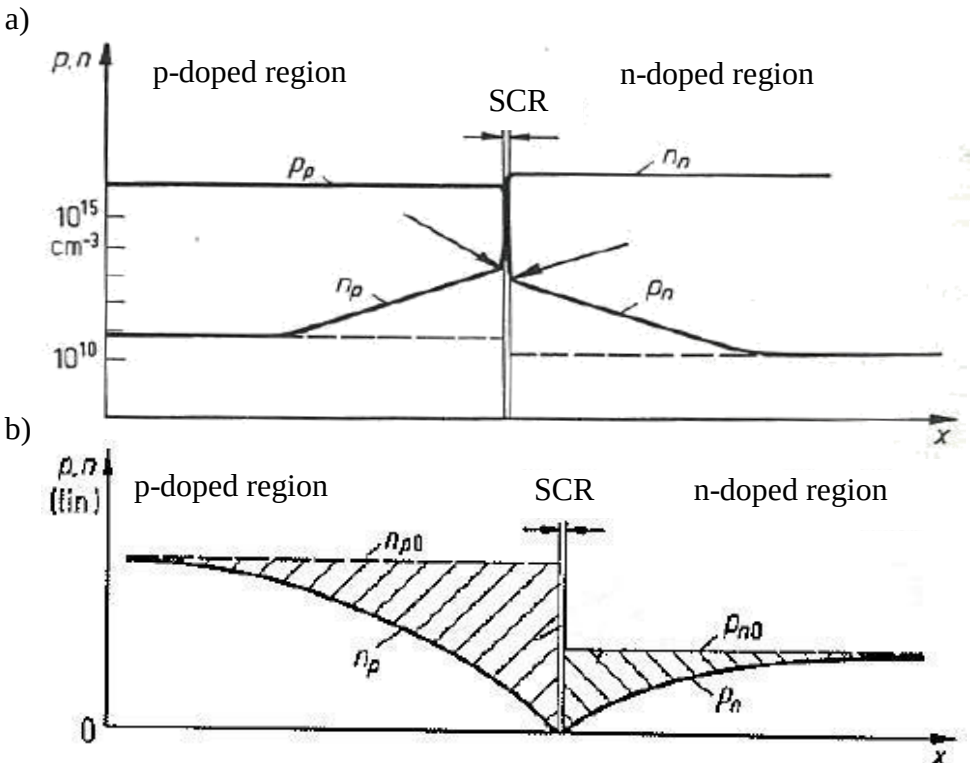

Figure 19: Charge carrier densities in a p-n-junction [54]:

a) forward bias

b) reverse bias

Under 0 bias condition, the diffusion voltage (U_D) is naturally applied to the space charge region. For U>0 V (forward bias) the voltage at the junction is U_D-U. The voltage is therefore reduced and electrons are induced into the p-region, while holes are induced in the n-region. As there are plenty of minority carriers injected from the majority carrier reservoirs, a comparatively large current can be expected.

For U<0 V (reverse bias) both majority carrier flows are prohibited by the bias, although a small amount of minority carriers transits the space charge region. These generate the cut-off current, which is very small. Also the minority carrier concentration is reduced at the borders of the space charge region, which leads to a voltage independent saturation current. For a better understanding the charge carrier densities for p-n-junctions in forward bias and reverse bias are illustrated in Figure 19a and b respectively.

Using the depletion approximation, the length l of the space charge region can be calculated by Equation {21}. In this model the space charge density ρ is defined by $\rho=e*(N_D-N_A)$, hence solely by the concentrations of the dopant atoms.

$$l = \sqrt{\frac{2\varepsilon}{e} * \left(U_D - U\right) * \left(\frac{1}{N_A} + \frac{1}{N_D}\right)} \qquad \{21\}$$

Equation {21} shows that the space charge region shrinks with increasing dopant concentration and bias voltage. Therefore a voltage change (ΔU) causes a charge alteration (ΔQ) at constant dopant concentrations by shifting the border of the space charge region. The quotient ΔQ/ΔU represents the junction capacitance C_S, which can be calculated by Equation {22}. This is comparable to the capacitance of a plate-type capacitor with a distance l between the plates, while A denotes the cross section and ε_0 and ε_r the dielectric permittivity in vacuum and the relative dielectric permittivity respectively.

$$C_S = \frac{A}{l} \varepsilon_0 \varepsilon_r \qquad \{22\}$$

If a forward bias is applied to a p-n-diode, holes are injected from the p-doped region into the space charge region. Therefore hole concentration at the border to the n-doped region surpasses the equilibrium concentration and a hole diffusion current is generated. These holes diffuse into the n-doped region and recombine with the surplus of electrons there. As the electrons are eliminated by recombination, a flow of electrons is generated, which decreases in the direction of the p-doped region. Accordingly a flow of holes is generated in the p-doped region by the recombination of electrons flowing from the n-doped region. The amount of holes and electron, which combine with each other in the space charge region is neglected here. The total current can be calculated by Equations {23} and {24}, where I_S and I_D are the currents measured at the source and drain respectively, n the emission parameter, U_T the thermal voltage, A the cross section of the p-n-junction, p_{n0} the hole density in the n-doped region at thermal equilibrium, L_p the diffusion length of holes in the n-doped region and τ_p the minority carrier life time in the n-doped region; the values for electrons in the p-doped region are named analogously.

$$I_D = I_S * \left(e^{\frac{U_D}{nU_T}} - 1\right) \quad \{23\} \qquad I_S = Ae * \left(p_{n0} \frac{L_p}{\tau_p} + n_{p0} \frac{L_n}{\tau_n}\right) \quad \{24\}$$

2.2.3 Real diode

The Shockley diode model (Equation {21}) is an extension to the ideal diode model (I/U characteristics are shown in Figure 20) and sufficiently describes most diodes encountered in practise, while conducting in forward bias.

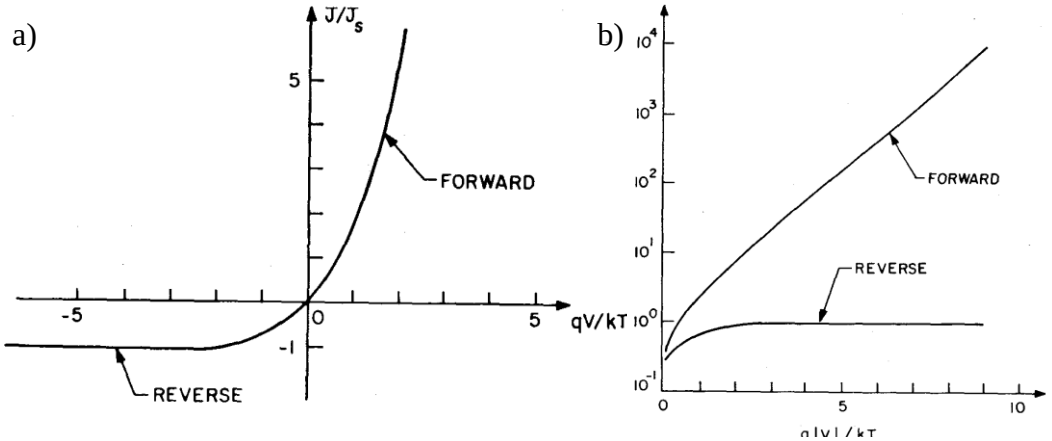

Figure 20: Ideal I/U characteristics of a diode [54]:

a) linear plot
b) semi- logarithmic plot

Nonetheless there are several effects which make a real diode differ from the values calculated with the Shockley model. These effects are shown in Figure 21 and subsequently explained.

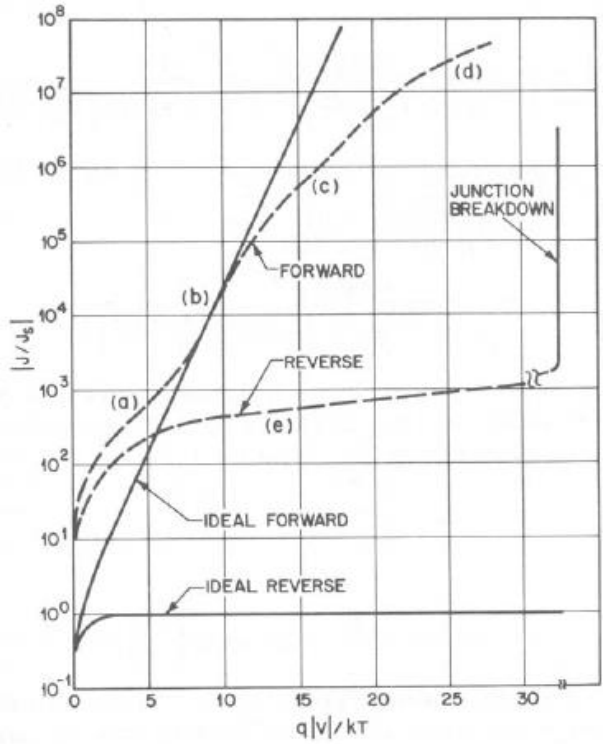

Figure 21: I/U characteristics of an ideal diode model in contrast to the Shockley model [54].

In total there are five effects, which make I/U curves differ from ideal:

(a) Generation-recombination current region
(b) Diffusion current region
(c) High-injection region
(d) Series resistance effect
(e) Reverse leakage current due to generation-recombination and surface effects

In region (a) the generation and recombination of excitons (electron-hole pair) dominates the current. An excition, or electron-hole-pair, is formed when an electron from the valence band is excited into the conduction band either by a photon or a phonon. This process is also called generation. Once excited, the electron has three options to relaxate. The first is by emitting a photon, what is normally encountered in LED. The excited electron can also fall back to a recombination level (between valence and conductance band) and then recombine with the hole in the valence band. This is accompanied by generation of a phonon and therefore emission of thermal energy. This option is strongly promoted when defects are inserted into the crystal lattice. The third

option is called Auger recombination and happens, when an excited electron recombines with a hole in the valence band and transfers its lost energy to second electron in the conductance band. The latter electron is then ionized.

Region (b) is influenced by the diffusion current. The diffusion current is induced by an unbalanced distribution of charge carriers, what is sought to be balanced by thermal fluctuation. The charge carriers are therefore diffusing to areas of lower concentration and causing the diffusion current.

High injection (region (c)) is encountered when the excess minority charge carrier density exceeds the doping density of the material. At the same time the majority carrier density also increases. For charge neutrality to exist, the excess electron density has to equal the excess hole-density. If this results in a net charge, a electric field is generated to restore charge neutrality.

At very high injections (region (d)), series resistance starts to play a role, what can mainly be attributed to the metal contacts at the end of the diode.

2.2.4 Surface effects

Because of their small size a considerable portion of a NW consists of surface atoms, which have different properties compared to bulk atoms. These surface atoms play a crucial role in charge carrier transport. Basically two effects can differ.

2.2.4.1 Surface scattering

Several sources can function as scattering centers for charge carriers in NWs, thus reducing their mobility. Quantitatively, the mobility of the charge carriers is determined by the rule of Matthiessen (Equation 25). According to this rule the different kinds of scattering, μ_I (Scattering due to impurities), μ_L (lattice phonon scattering), μ_D (scattering on defects) and μ_S (surface scattering), are only considered as if just their specific scattering occurs. The correlations between the scattering sources are not taken into account by the Matthiessen rule, but delivers a rather good approximation.

$$\mu^{-1} = \left(\frac{1}{\mu_I} + \frac{1}{\mu_L} + \frac{1}{\mu_D} + \frac{1}{\mu_S} + \ldots \right) \quad \{25\}$$

For NWs, a high portion consists of surface atoms, thus increasing surface scattering and decreasing the overall charge carrier mobility. As surface defects can reduce the electron mobility considerably, a lower dopant concentration can be calculated than actually present in a NW, if this is not taken into account.

2.2.4.2 Surface charges

When getting in contact with air a Si-NW inevitably gets covered with native oxide. At the interface between the oxide and the remaining Si body, traps with energy states within the Si band gap are may be formed. These states are generated by excess silicon, dangling Si bonds, excess oxygen or impurities [82]. Typically, this results in a positive charge region near the interface [83], and a depletion region is formed to compensate this surface charge (Figure 22). Aside of enhanced scattering, this reduces the effective conducting cross section of a NW.

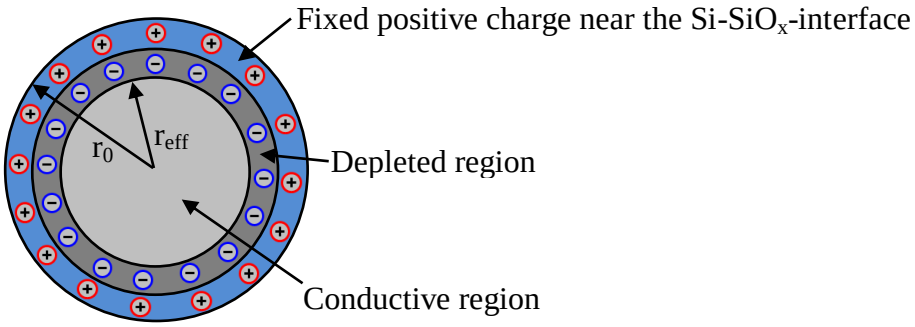

Figure 22: Schematic of a p-type NW cross section, with a depletion region due to the presence of positive charges at the Si-SiO_X-interface. The conducting portion of the NW is therefore reduced with respect to the geometric dimensions; After Wolf et al. [83]

The effective radius of the conductive region r_{eff} is described by Equations {26} and {27}, with interface charge density N_S, electrically active dopant concentration N_a, the NW's radius r_0, the radius of the unaffected NW r_{eff} and the length of the NW L.

This condition is called charge balance equilibrium, when the total charge at the interface is completely balanced by the charge in the depletion region inside the NW [84]. The area for the remaining conductive region A_{eff} can be calculated from Equation {27} and Equation {28}.

$$N_S 2\pi r_0 L = N_a \pi \left(r_0^2 - r_{eff}^2 \right) L \quad \{26\}$$

$$r_{eff}^2 = r_0^2\left(1-\frac{2N_S}{r_0 N_a}\right) \quad \{27\}$$

$$A_{eff} = \pi r_{eff}^2 = \pi r_0^2\left(1-\frac{2N_S}{r_0 N_a}\right) \quad \{28\}$$

Equation {28} can be further combined with Ohm's law R=ρ*(L/A) to calculate a NW's resistance (Equation {29}).

$$R = \rho L\left[\pi r_0^2\left(1-\frac{2N_S}{r_0 N_a}\right)\right] \quad \{29\}$$

It obvious from Equation {28}, that a high dopant concentration N_a increases A_{eff}. In this case the electrons that are necessary to compensate the positive interface charge are available in huge numbers and therefore the depletion region is negligible. An intense investigation and quantification of the size of A_{eff} has been conducted by Schmidt et al. [85]. They stated that a critical radius can be calculated in dependence of surface potential, surface charge density and trap level densities. According to this work a NW with 50 nm in diameter, a medium trap level density of 10^{11} $eV^{-1}cm^{-2}$ and fixed oxide charge density of zero should have at least an active dopant concentration (N_A) of $3*10^{16}cm^{-3}$ or it would be fully depleted.

In this context it should be mentioned that Kamins et al. [86] discovered the ability of surface adsorbed molecules to modulate a NW's conductivity due to their inductive effect. The inductive effect describes the phenomenon, that molecules can change the electron distribution within the molecule by their electronegativity. This results, depending on the nature of the atoms in the molecule, in an increased or decreased electron density across the molecule. These molecules can then adsorb to a NW's surface and influence surface charges. Dependent on whether the molecules experience a +I or –I (charging or de-charging of electrons into the NW's surface) effect the induced surface charges can either repel or attract mobile charges and thus decrease or increase its conductivity.

2.2.5 In-situ doping of NWs

A NW's electrical properties, habitus and defects strongly depend on the growth process. Although the theoretic aspects of this theme has been discussed earlier, the appliance to a practical growth process is far from simple; especially when doping agents are intentionally - or even unintentionally - involved.

A good example for unintentional doping is the work of S. M. Eichfeld et al. [87], where Si-NWs were grown in Al templates. The intrinsic NWs experienced an unusual low resistivity of roughly 2.7 Ω*cm compared to bulk Si, which exhibits ~10^5 Ω*cm. Later investigations revealed Al doping, which was incorporated from the templates during growth. In CVD related methods other metal catalysts, like In and Ga, have similar effects on a NW's resistivity and usually cause p-type doping.

Another possibility to insert dopants into a NW during growth is to add them to the catalyst particle. Schmidt et al. [26] added a small amount of Sb to the catalyst particle of Au to achieve in-situ doping of a Si-NW, which was later integrated into a vertical surround-gate FET. Although this methods works in principal, it was found to be inefficient in this work.

Perhaps the most common method to introduce doping atoms during growth is to add a gaseous dopant; an overview of the effects on resistivity is shown in Figure 23. Investigations on this theme were made by Cui et al. [31] and J. R. Heath et al. [33], who received intrinsic Si-NWs with specific resistivities of at least 3.9*10^2 Ω*cm.

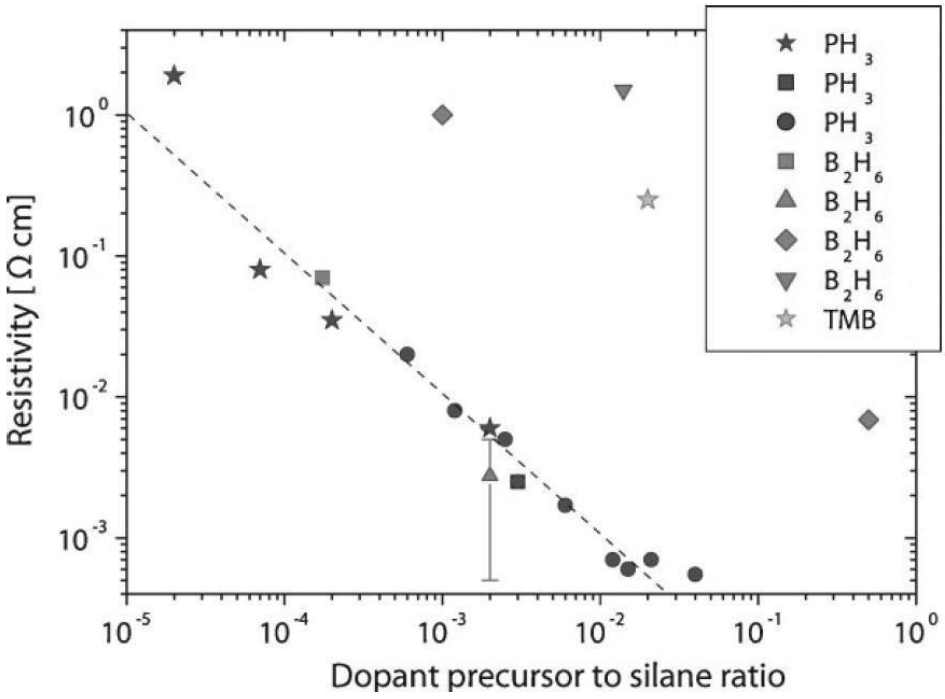

Figure 23: Si-NW resistivity versus dopant/silane ratio after Schmidt et al. [3]. Three phosphorus dopants and five boron dopants were plotted (TMB – tetramethylboron). The P-doped NWs show a practical linear dependency between resistivity and amount of added dopant.

When these NWs are doped with P (from PH_3) the specific resistivity dropped down as far as $2.3*10^{-2}$ Ω*cm. Björk et al. [27] also found out, that there is almost linear dependency between resistivity and dopant/silane ratio when using PH_3, as long as no PH_3:SiH_4 ratio greater than $2*10^2$ is applied. In this case, NW nucleation seems to be inhibited [29].

Unlike P dopants, B dopants severely alter the growth process and therefore do not apply to such a simple dependency. Lauhon et al. [75] discovered, that the presence of B accelerates the decomposition process of the precursor and a thick amorphous shell is deposited around the NW, what impedes proper contact formation. As amorphous Si also features a larger resistivity than crystalline Si, this is a good explanation for the rather high resistivity encountered for p-type Si-NWs by Lew et al. [28] and Cui et al [31]. In some cases, the presence of B is also responsible for a strong NW tapering. Nonetheless the acceleration of precursor decomposition usually shifts growth temperatures downwards.

Cui et al. [31] also investigated Si-NWs via back gated measurements (Figure 24).

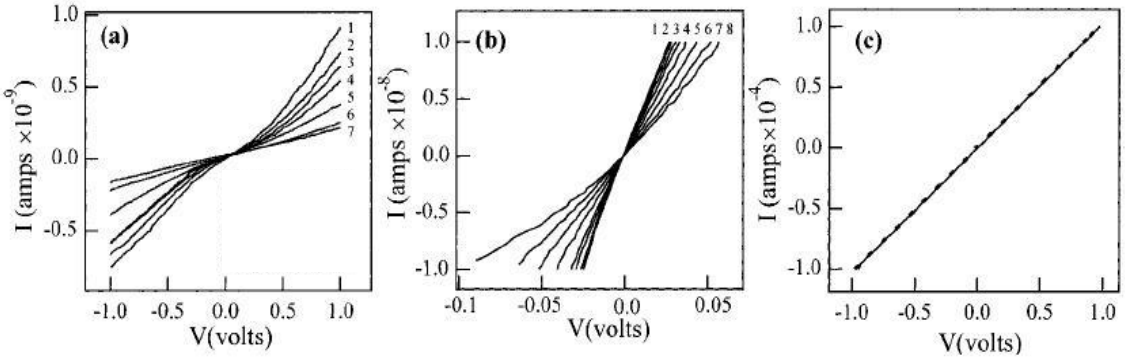

Figure 24:

a) I/V recorded on a 70 nm diameter intrinsic Si-NW at different gate voltages (V_G). Curves 1, 2, 3, 4, 5, 6, and 7 correspond to V_G = -30, -20, -10, 0, 10, 20 and 30 V, respectively.

b) I/V data recorded on a 150 nm diameter B-doped Si NW; curves 1-8 correspond to V_G = -20, -10, -5, 0, 5, 10, 15 and 20 V, respectively.

c) I/V curves recorded on a 150 nm diameter heavily B-doped Si NW; V_G = 20 V (solid line) and 0 V (heavy dashed line) [31].

Figure 24a shows the electric behaviour of intrinsic NWs at different gate voltages (V_G). When decreasing V_G, the resistivity also decreases what is typical for a p-type semiconductor. The I/V relation is mostly linear, although curving at voltages around V_G=0 indicates non-ohmic contacts. When doping the NWs even slightly the contacts become ohmic and also experience stronger p-type behaviour (Figure 24b). In contrast, highly B-doped NWs could not be modulated anymore as the conducting channel could not be closed (Figure 24c).

2.2.6 Electrical characterisation of Si-NWs

When measuring a NW's resistivity, the probably most common method is to apply a voltage between two contacts and to measure the current. This measurement setup is known as a 2-point measurement, where the calculated resistance according to Ohm's law (U = R*I) consists of the actual resistance of the NW (R_{NW}) and a parasitic serial resistance (R_C) originating from the contacts (Equation {30}).

$$\frac{U}{I} = 2R_C + R_{NW} = R_T \qquad \{30\}$$

The contact resistance in case of a Si-NW, where contact areas are small and Schottky contacts are encountered, can be considerably high.

To avoid this problem a 4 point measurement setup can be used according to Figure 25. The current at contact 2 and contact 3 is set to 0 A, while a defined voltage U_{SD} is applied between contacts 1 and 4. As current and voltage electrodes are separated in this setup, the voltage drop ΔU can be measured currentless and therefore independent from the contact resistance.

Using ΔU and the current between contact 1 and contact 4, I_{SD}, the NW's specific resistivity ρ can be calculated by equation {31} when the NW's geometry (radius = r, length between contacts 2 and 3 = l) is known. This makes the 4-point measurement setup a convenient choice for measuring a NW's resistance (R_{NW}).

$$\rho = \frac{\Delta U * r^2 \pi}{I_{SD} * l} \quad \{31\}$$

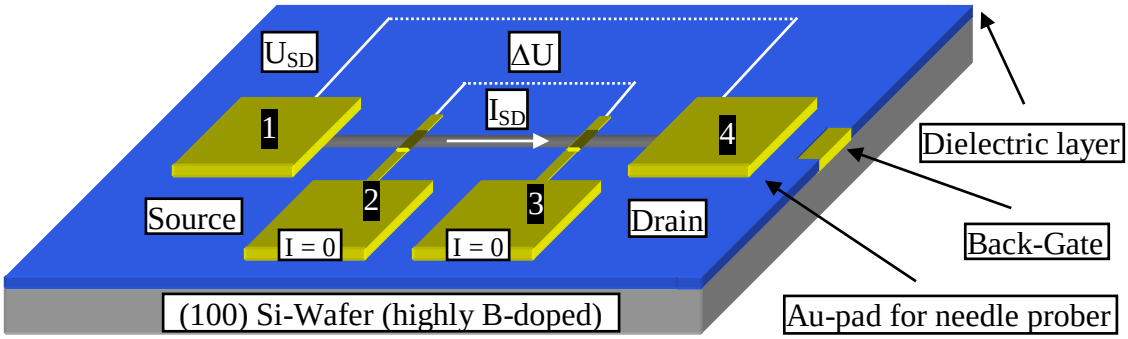

Figure 25: Schematic for a 4-point measurement of a NW with an isolation layer and back gating possibilities. This setup allows measuring R_{NW} by separation of current and voltage electrodes.

2.2.7 Backgated Schottky-Barrier NW-FET

One of the most convenient ways to build a NW-FET is to remove the NWs from their substrate by ultrasonication, disperse them on a highly conductive Si-wafer with an dielectric layer atop and contact them via electronic beam lithography, metal deposition and lift off techniques. In this setup, the NW works as the channel of a FET device and the Schottky-contacts as source/drain p-n junctions. Subsequently the substrate was

contacted through the dielectric layer. Hence the highly doped Si-substrate functions as a back gate (Figure 26).

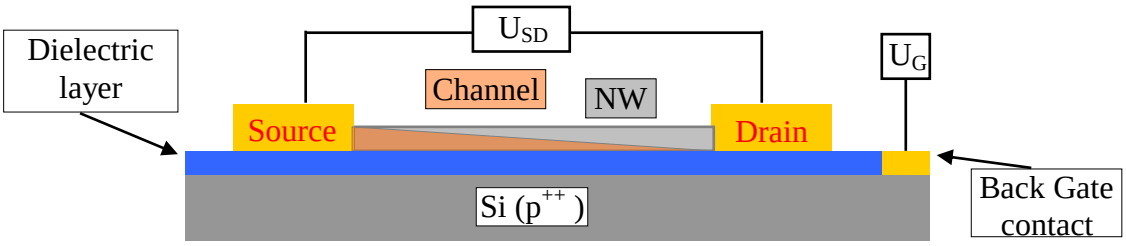

Figure 26: Schematic setup of a NW-FET. A constant voltage is applied between source and drain (U_{SD}), while modulation of U_G causes a channel to be formed along the NW by either injection or removal of electrons. The dielectric layer electrically separates the NW from the substrate.

One of the major effects when measuring such a NW-FET is that the applied gate voltage strongly influences the band structure of the NW. When a negative voltage is applied at the gate the NW's band bends upwards. Vice versa the band bends downwards when U_G becomes positive [88]. This behaviour is described in Figure 27.

If there is strong upwards bending holes are accumulated at the NW's surface. Because of the Schottky barrier height, the carrier injection through the source barrier predominantly consists of tunnelling holes as depicted in Figure 27a. If U_G is set to 0 V, the charge carrier transport becomes dominated by thermoionic emissionthrough the source barrier, because the barrier width increases due to weak downward bending of the band structure (Figure 27b). So the Schottky barrier for the holes increases when U_G becomes increasingly positive. In the case of a positive gate potential (Figure 27 c), the charge carrier transport is dominated by electrons tunnelling through the drain barrier. In literature, where more electrons are accumulated at the NW's surface than there are holes in the NW, this phenomenon is called inversion.

The schematic in Figure 27d shows a semi-logarithmic plot describing the transfer characteristics for the three cases in Figure 27a, b and c. In the dark red region the current transport is dominated by thermoionic emission of holes. In this ohmic regime the relation between U_G and I_D is exponential. The inclination peaks in this region, which extent strongly, depend on the overall resistance of the device. The remaining

two regions are dominated by the tunnelling of holes (light red) and electrons (blue), what depends on the Schottky barrier height.

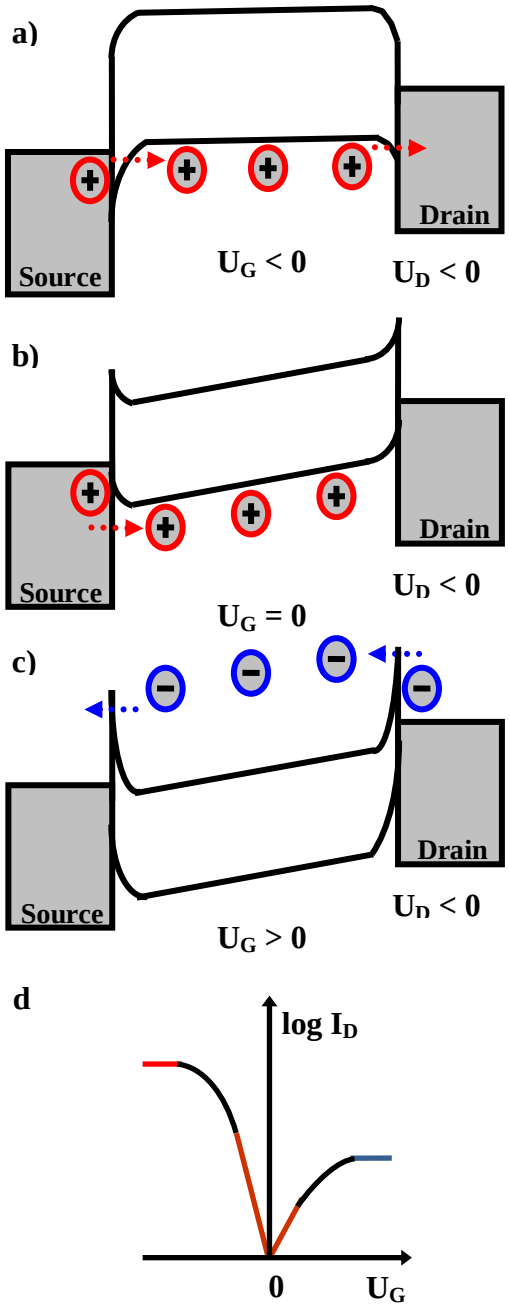

Figure 27: Schematic illustration of band structures of a Schottky-Barrier FET.

a) V_G<0V; The bands are bent upwards, thus resulting in a tunneling current of holes through the source barrier.

b) V_G=0; Holes flow from source to drain by thermo-ionic emission.

c) V_G>0V; Electrons tunnel through the drain barrier

d) Expected transfer characteristics are illustrated by a schematic

2.3 Transmission Electron Microscopy (TEM)

2.3.1 Principles of TEM

As mentioned before crucial factors for a NWs quality are its crystallinity, growth orientation and composition. To analyze these properties on the nanoscale, TEM is the ideal tool. TEM offers the possibility to visualize even the tiniest defects like stacking faults, twin crystals, substituted or missing atoms, growth orientation, strain and thickness effects. It is also possible to analyze compositions in nano scale volumes [89], when using energy dispersive detectors. Respective methods are called Electron Energy Loss Spectroscopy (EELS), where the energy loss of inelastic scattered electrons is determined, and Energy dispersive X-ray Difraction (EDX), where X-ray emission from the sample is measured after being excited by an incoming electron. One disadvantage of TEM is the sometimes extensive sample preparation, in most cases sufficient thinning, as electrons must be able to pass through the specimen to be analysed. Luckily this part is not necessary with NWs as they are already transmissible at their tiny sizes.

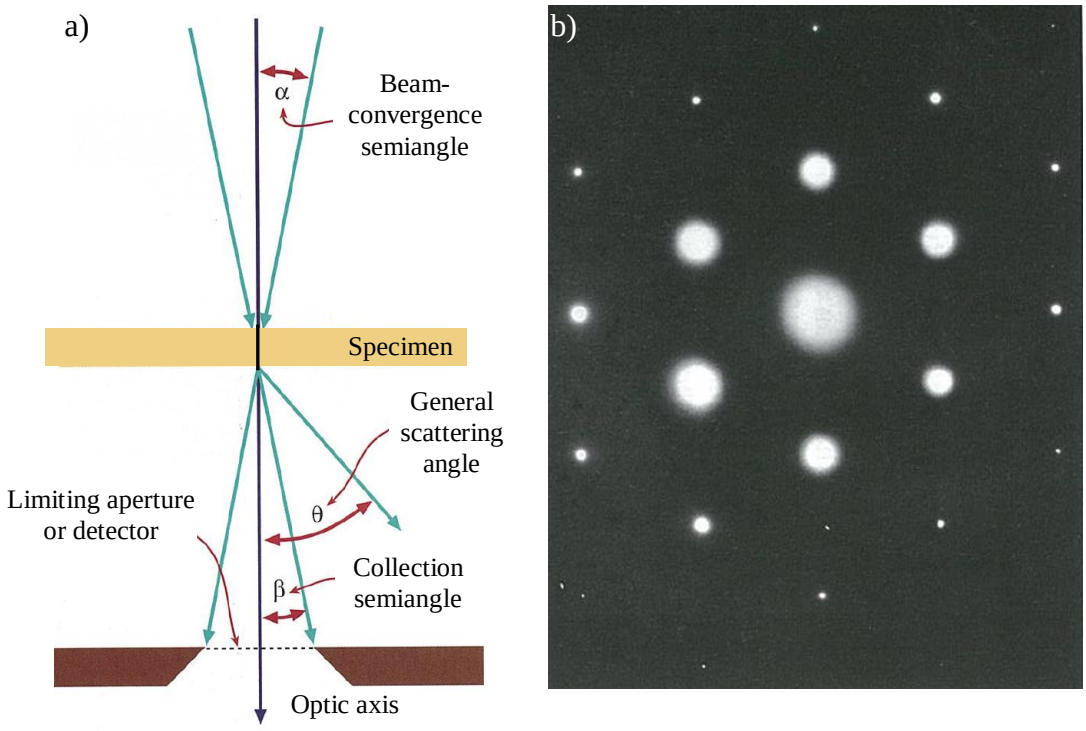

Figure 28: a) Schematic illustration of TEM principle, where the inclined electron beam is focused on the sample and scattered in discrete angles depending on the sample's crystallographic properties.
b) Diffraction pattern (DP) of a Si (111) plane (DP) generated by this method [89].

The principal operating mode of a TEM is shown in Figure 28a. The acceleration voltage is an important feature of a TEM and usually ranges from 80 to 400 kV, although there are also TEMs in the MV region for conducting special analysis. The thickness of the sample can range from the nanometer-scale up to some micrometers. Atoms with high atomic numbers cause greater back scattering rates of the electrons and therefore such samples need to be thinner.

The electron beam is focused by condenser lenses on the area of interest so that practically all electrons incline parallel to each other. The electrons are then scattered in certain angles by the atoms in the sample according to the crystallographic properties of the sample. The scatter mechanism proceeds according to Rutherford scattering.

After the electrons have passed the sample, the diffracted electrons are analysed by a CCD camera, which analyses the distribution of the reflexes and converts it into a 2D-diffraction pattern (DP, Figure 28b). For exact analyses on increasingly small areas, monochromators are used to reduce the energy spread of electrons. Modern devices are capable of reducing the spread to 0.15 eV.

Similar to a light microscope, also a TEM can be operated in bright field or dark field mode. When using the bright field mode, the whole beam is used for imaging. Thicker regions or regions with heavier atoms appear dark as fewer electrons are able to pass through and reach the detector. If the un-scattered beam is blinded out by an aperture, the sample will appear dark wherever no electron scattering is present, this is called dark field mode and usually employed to enhance contrast.

In theory these reflexes only appear if the Bragg condition is fulfilled as only then constructive interference occurs (white spots in a DP). Otherwise no reflexes should be observable due to destructive interference (see Figure 29 for illustration and subsequent derivation).

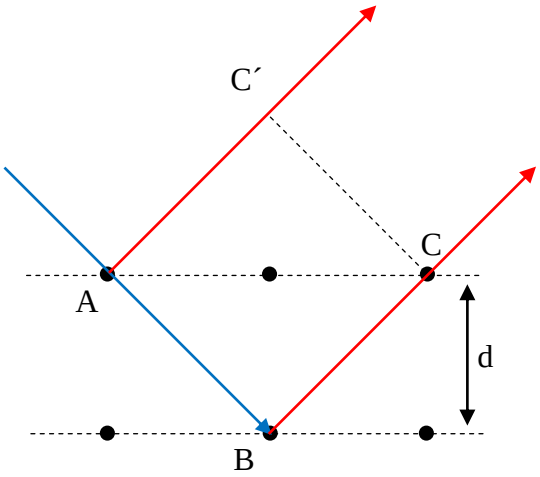

Figure 29: Schematic of electron scattering at 2 different atoms on different atomic layers. If the Bragg condition is fulfilled constructive interference leads to a bright spot in the DP [89].

The following derivation will explain why there is only constructive interference when the Bragg condition is met.

There is a path difference between the ray reflected at A and the ray, that transmits first and is then reflected at B (path AB and AC). The latter one of those two exhibits a path difference, which can be written as:

$$(AB + BC) - (AC')$$

Eventually these two rays are in the same phase and conduct constructive interference only when λ (wavelength) is an equal to any integer of d (lattice constant), or vice versa.

$$(AB + BC) - (AC') = n\lambda$$

By using trigonometric functions, the paths can be written as:

$$AB = BC = \frac{d}{\sin\theta} \quad \text{and} \quad AC = \frac{2d}{\tan\theta}$$

The path AC' can also be written by using trigonometric functions as:

$$AC' = AC * \cos\theta = \frac{2d}{\tan\theta}\cos\theta = \left(\frac{2d}{\sin\theta}\cos\theta\right)\cos\theta = \frac{2d}{\sin\theta}con^2\theta$$

Combining these equations finally leads to:

$$n\lambda = \frac{2d}{\sin\theta}\left(1-\cos^2\theta\right) = \frac{2d}{\sin\theta}\sin^2\theta$$

This can be simplified to:

$$\boxed{n\lambda = 2d * \sin\theta}$$ Bragg's law

In practise there are reflexes observable even though the Bragg condition is not met. To correct this problem, the Ewald sphere was introduced (Figure 30).

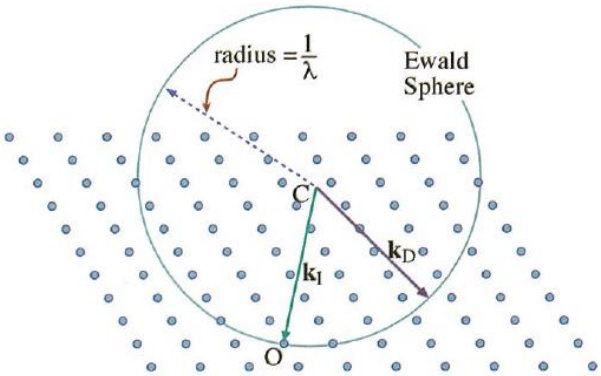

Figure 30: Ewald sphere intersected in an array of reciprocal lattice points [89] with k_I and k_D representing the wave vectors of the incident and the diffracted beam.

If the Ewald sphere cuts through a reciprocal lattice point (fourier transform of the spatial wavefunction of the original lattice) the Bragg condition is met and a reflex appears. Nonetheless reflexes are present even if the Ewald sphere is not intersected. The reason for this is that diffraction at reduced intensity can still occur, if the reciprocal lattice point is close enough to the Ewald sphere. To quantify this deviation an excitation error or deviation parameter s has been introduced, which describes the distance between a lattice point and the Ewald sphere. A further correction of s is done by considering the extinction distance ξ_g (Equation {32}), which is defined as the distance the beam travels as its intensity changes from I = 1 to I = 0 and back to I = 1 while passing through in the specimen.

$$s_{eff} = \sqrt{s^2 + \frac{1}{\xi_g^2}} \quad \{32\} \qquad \left|\Phi_g\right|^2 = \left(\frac{t\pi}{\xi_g}\right)^2 \frac{\sin^2\left(ts_{eff}\pi\right)}{\left(ts_{eff}\pi\right)^2} \quad \{33\}$$

Thus it is possible to calculate the thickness (t) dependant intensity ϕ_g by the Howie-Whelan equations (Equation {33}).

As the radius of the Ewald sphere is inversely proportional to the wave length λ of the irradiated electrons the sphere extends with increasing acceleration voltage. A flatter sphere can intersect more lattice points and so higher voltages are favored for TEM analysis; i. e. 200 kV to 1300 kV in practice.

The angles and distances between these reflexes in a DP can be attributed to scattering angles of electrons passing through the sample. Every crystal scatters electrons in a characteristic way and therefore its crystal structure, crystal orientation and composition can be identified. Therefore depending on the angle and distance of the reflexes to the center, a DP can be indicated. Figure 31 gives an example of (111) and (112) plains of a cubic-fcc crystal like Si or Ge. In practice, the resulting DP also depends on the tilt and turn angles of the sample relatively to the incident beam, so mostly specialized software is used to reduce time and effort when indicating a DP.

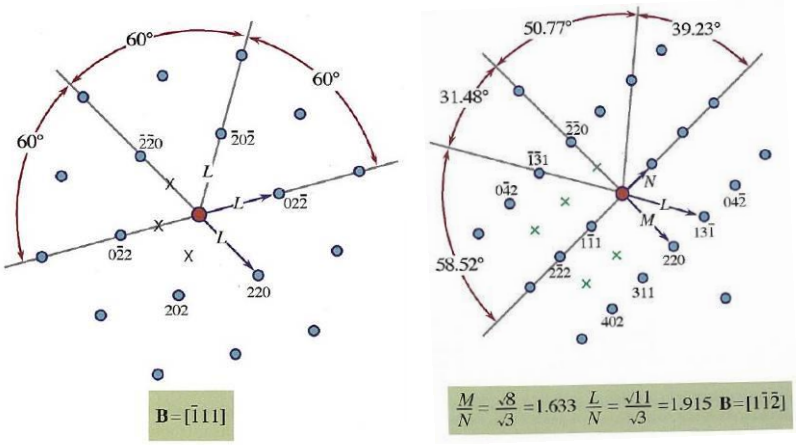

Figure 31: Diffraction patterns with crystallographic orientations and their respective angles to each other already indicated [89].

a) cubic-fcc (111) plane

b) cubic-fcc (112) plane

2.3.2 Thickness effects

Another important feature of TEM is the determination of the thickness fringes, sometimes also called thickness contours. This phenomenon can be explained by means of Figure 32a, which shows a thin, etched MgO film with holes in it. The direct and the diffracted beam's intensity oscillate in a complementary way (Figure 32b), what causes an intensity fluctuation along a thickness gradient. If the sample is very thin, the

intensity of the direct beam is high and these regions appear white in a bright field image. Analogously the very same regions would appear black in a dark field image as the intensity of the diffracted beam is next to zero. The exact difference in fluctuation is given by ξ_g, the extinction distance, what causes the diffracted beam's intensity to peak at integer values of ½ of ξ_g. In practice this causes an alternating pattern of bright and dark region as seen in Figure 32a.

This phenomenon is also highly dependent on the angle, what reduces the validity to very small areas. With increasing thickness of the sample, the percentage of absorbed electrons naturally increases and the contrast is less pronounced, what results in a more dimmed image (lower left of Figure 32a).

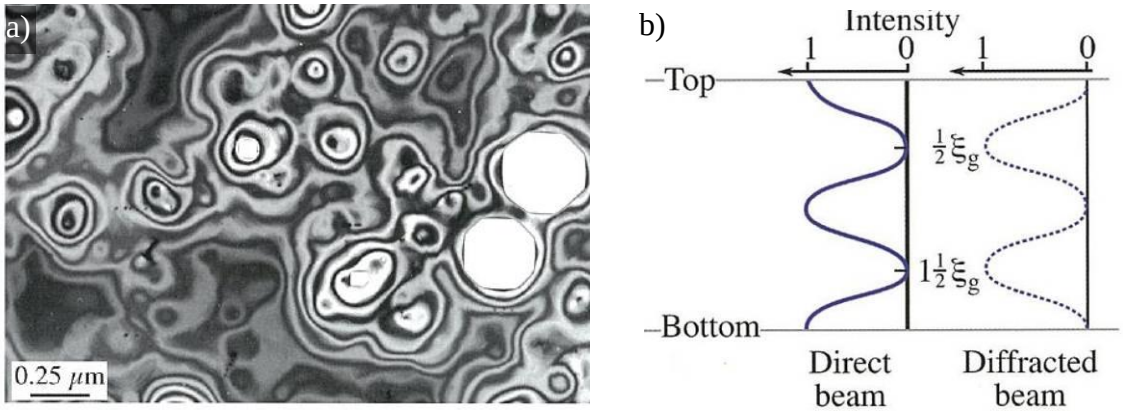

Figure 32: a) Bright-field image of an etched MgO film. The white regions represent holes.

b) shows the dependence of the direct and diffracted beam's intensity. At certain values of ξ_g the intensity of the beam either reaches a maximum, or diminishes completely, what is caused by constructive or destructive interference. ξ_g depends on the distance the electron travels through the sample [89].

2.3.3 Stacking faults

Principally a stacking fault occurs when a crystallographic plane is terminated during growth and the adjacent planes bend into the now available space (Figure 33a). Figure 33b shows a bright field TEM of stacking faults as fringes with alternating intensity. The reason for this alternating pattern is that due to the bended planes the crystal deforms and the excitation error s_{eff} differs. This affects intensity and results in a striped pattern. Figure 33c shows this also in a High resolution TEM on the nano-scale [90].

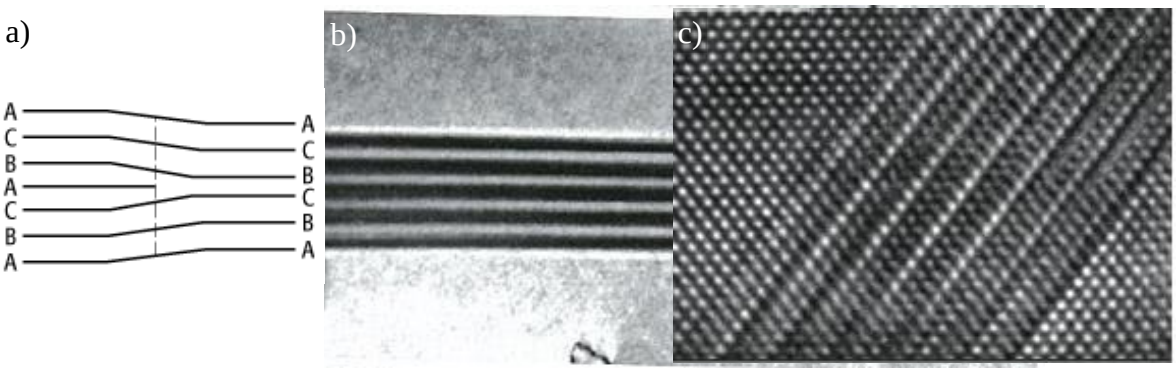

Figure 33: a) Schematic illustration of a stacking fault where one crystallographic plain cedes to exist and two adjacent planes bend into the available space.
b) Bright field TEM-image of stacking faults in an fcc material [89].
c) A High resolution TEM can reveal stacking faults in Si [90].

2.3.4 Twinning

A crystallographic twin is usually encountered, when two crystals of the same species join together by a definite, mutual orientation. There are three kinds of singular twin crystals known.

Contact twins are aligned via a single composition surface across a mirror surface. Quartz or plagioclase often exhibits such twins. Merohedral twins occur when contact twins are 3-dimensionaly aligned, such as relative rotation of one twin to the other. Penetration twins appear as passing through each other in a symmetrical manner. Of course each kind of twinning can occurs in a single sample, what is known as multiple or repeated twins.

When analyzing such an interface with TEM, the twin interface can be seen as a thin platelet (Figure 34a) or parallelepiped, which is inclined to the samples' parallelepiped. Therefore each parallelepiped has a relrod. These can be intersected by the Ewald sphere, one normal to the surface sample and a second one normal to the twin boundary, what leads to a double spot in the SAED pattern linked by a thin line (Figure 34b). The space between the two spots increases with increasing s and is of course dependent on the beam's angle.

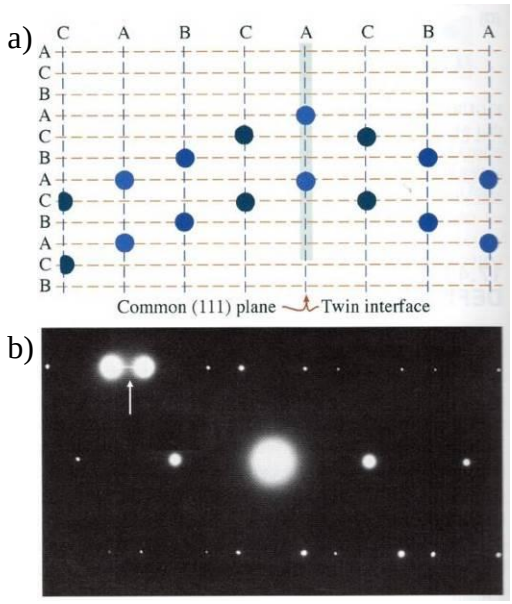

Figure 34: a) Schematic of a twin boundary interface represented by a thin platelet.
b) The DP shows two spots linked by a line. The spots originate from the sample and the twin boundary [89].

3 Experimental setup

3.1 Atmospheric Pressure Chemical Vapor Deposition (APCVD)

3.1.1 APCVD-setup

Figure 35 shows the main components of the growth apparatus; a horizontal tube furnace with three separately controlled heating zones, a quartz tube connected to a gas supply and a pumping unit.

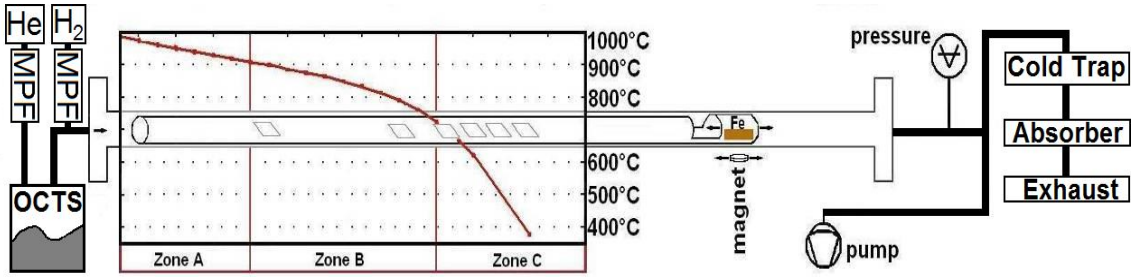

Figure 35: Schematic of the atmospheric pressure CVD system used for the growth of Si-NWs with OCTS. Helium is dosed by a Mass Flow Controller (MFC) as carrier gas and routed through an OCTS filled saturator. H_2 is also dosed by an MFC, but does not pass the saturator. Heating zones A, B and C are regulated so that the temperature of the sample can be adjusted by positioning the samples along the temperature gradient. The Fe piece in the sample holder allows placing the sample at the desired temperature even during growth. To clean and purge the system prior to the experiment, a pump is used along with a manometer. Finally gaseous byproducts and remainders of the growth process are collected in a N_2 (l) filled cold trap and an absorber to reduce waste and hazard.

To provide the furnace with gaseous OCTS precursor a saturator is utilized with He as feed gas. A Mass Flow Controller (MFC) regulates the amount of gas directed through the saturator. Via a second pipe, H_2 is introduced into the system, to adjust growth parameters. The amount of H_2 added is controlled by a second, separate MFC. The combined gas feed is then routed through a quartz tube inside a furnace with three heating zones. Each zone can be controlled separately, thus a defined temperature

profile can be adjusted. By using this profile several samples can be grown at different temperatures in one batch. A small piece of iron is placed at the rear of the back of a quartz glass sample holder, so that it can be moved freely by a magnet without breaking vacuum or growth atmosphere even during the growth process. So the temperature of the sample can be adjusted by positioning the holder with a magnet. As OCTS is also a harmful chemical and other decomposition products like chlorine gas and different chlorosilanes can be expected to form, a cold trap and an absorber are added before the exhaust to trap dangerous, gaseous species.

3.1.2 APCVD-growth process

Pieces of Si (111) are chosen as substrates, cleaned with acetone, rinsed with propan-2-ol and blown dry with N_2. A following dip into buffered hydrofluoric acid (BHF; $HF:NH_4F=7:1$) removes the native oxide and guarantees a hydrogen terminated silicon surface. Depending on the growth parameters, a 2 nm thick layer of metal catalyst (Ag, Al, Au, Cu, In, Ni, Pt and Ti) is deposited on the substrate either by plasma enhanced sputtering or thermal evaporation. Where possible, colloids dispersed in propan-2-ol replace the deposited layer to offer additional size control. The colloids are deposited onto the sample by an Eppendorf pipette. Afterwards the propan-2-ol evaporates at a hotplate at 50°C. After an additional BHF dip the samples are immediately introduced into the APCVD-growth system. The tube is then alternately evacuated and purged with He three times to remove any remainders of air. The furnace is then heated up with the samples still outside of the heating zones under a flow of 100 sccm He until atmospheric pressure is achieved. Depending on growth parameters, 0 to 40 sccm of H_2 are added to the gas feed. When the furnace reaches the final growth temperature the sample holder is transferred into the growth region with the aid of the magnetic specimen-transport system. The specimen remains at the chosen temperature for 30 minutes to saturate the catalyst with Si from the substrate. The precursor is then introduced by routing He through a saturator creating a gas mixture with a partial pressure of ~0.03 mbar of OCTS. The temperature during growth is determined by the position of the sample holder. Routinely, after 60 min growth the sample holder is pulled out of the heating zone resulting in a very fast cool down of the samples remaining in the growth atmosphere. Afterwards, the precursor flow is stopped and the quartz tube is purged with He. In following experiments the precursor is mixed and subsequently distilled with BBr_3 and alternatively PCl_3 to produce in situ doped NWs.

3.2 Sample preparation for TEM imagining

To determine the crystallographic nature and eventual defects, the as grown samples are immersed in propan-2-ol. The NWs are then removed from the substrate by ultrsonification. Thus a suspension of NWs is created, which is later also used for electrical characterisation. Quantifoil TEM grids (Figure 36) are then used as carriers for TEM investigations. The TEM grids features a perforated carbon film with 2 µm holes separated by 2 µm mounted on a 200 mesh of copper. These grids are put into the NW suspension and used like a fishnet to collect NWs on the support film. Unlike many other bulk sized samples, which need extensive preparation, NWs can be made ready within minutes for analysing by this method. Sometimes organic contaminations, probably originating from the propan-2-ol used as suspending agent, are encountered and have to be removed by plasma cleaning prior to measurement. The NWs are then examined by a TECNAI F20 TEM.

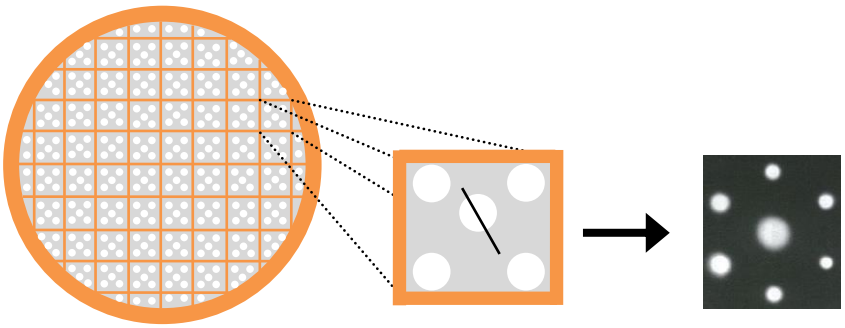

Figure 36: Schematic of a Quantifoil TEM grid made of Cu with a perforated carbon film to handle nanosized samples. The magnification shows a NW caught on the support film ready for TEM investigation. Next to it is a diffraction pattern showing a (111) Si -plane.

3.3 Electrical Characterization

Electrical characterization of the Si-NWs is conducted with a needle prober. All four point probe measurements as well as field effect measurements are performed in a darkbox. Micromanipulators are used to contact pads of about 50x50 µm by aid of a microscope. For characterization a precision semiconductor parameter analyser (HP 4156A) is used.

The processing of the measurement module is schematically shown in Figure 37. As substrate a highly p-doped piece of a (100) Si-wafer, which is cut along the (100) plane (Si^{++} (100)), is covered with 80 nm of Al_2O_3 by atomic layer deposition (ALD). According to Figure 37/step I, the wafer piece is covered with AZ5214E photo resist (microChemicals GmbH). 200x200 µm² sized pads are structured by VIS lithography. Metal deposition is achieved by sputtering of Ti/Au (15 nm/120 nm), followed by a lift off in acetone (step II and III). The suspension of NWs prepared earlier is then dropped onto the prepared substrate (step IV) and covered again with polymethyl methacrylate resist. Electron beam lithography is used to structure the contacts of the NWs and links to the prepared Ti/Au pads (step V).

After resist exposure and a very short dip in BHF, 100 nm Ni are sputtered. This is followed by a lift off through soft ultra-sonic sound in acetone (~50°C). Finally, to get access to the back gate a contact is formed by locally scratching through the Al_2O_3 layer and again sputtering 100 nm of Ni with a shadow mask (step VI).

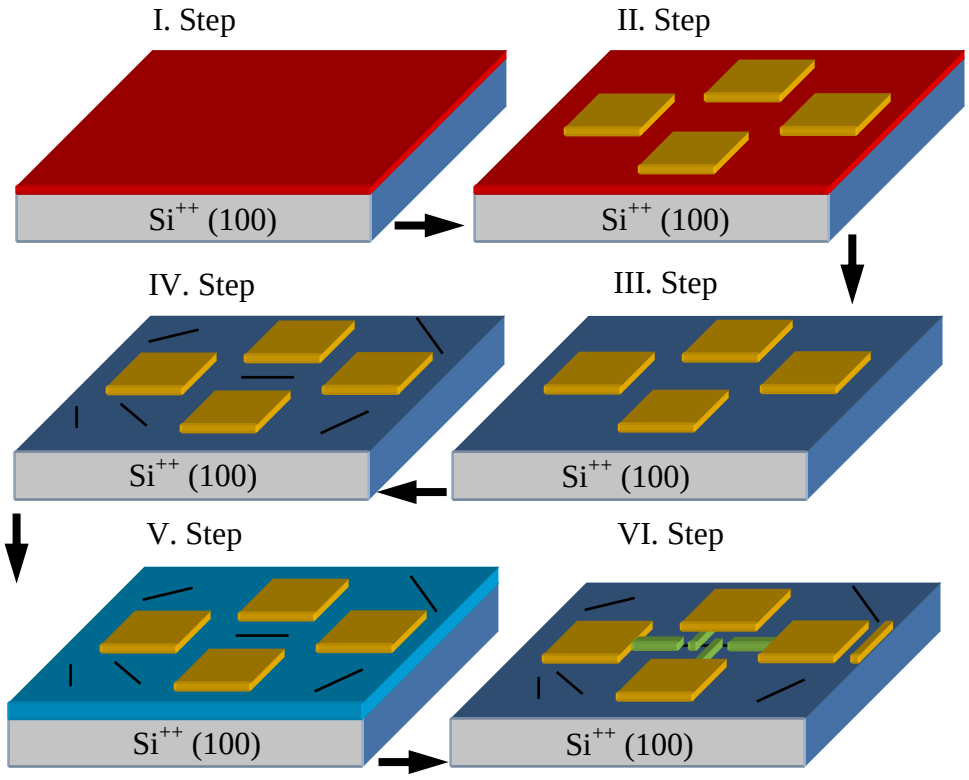

Figure 37: Process flow to realize the measurement setup

Step I: A Si^{++} (100) piece with an 80 nm Al_2O_3 layer atop (ALD) is covered by lithographic resin.

Step II: The resin is structured by VIS-lithography and Ti/Au-pads are sputtered.

Step III: The resin is completely removed by lift off techniques.

Step IV: Distribution of in propan-2-ol dispersed NWs on the sample.

Step V: Distribution of resin on the specimen and subsequent structuring of contacts with e-beam lithography.

Step VI: Sputtering Ni contacts (100 nm thick) and performing a lift off with ultra sound in acetone. Afterwards a back gate was added by locally scratching the Al_2O_3 layer followed by sputtering Ni with a shadow mask.

3.4 Device processing of an in situ grown NW-diode

According to Figure 38 a highly B-doped (111) Si substrate is prepared for growth as described above with 80 nm Au colloids as catalyst. OCTS mixed with PCl_3 is then used to grow highly P-doped, epitaxial NWs to form an in situ grown diode (step I). To measure that diode the as grown NWs are embedded in 3 µm SU8 2002 resist (step II), followed by a hard bake and laid open by RIE (step III). The NWs upper ends are then covered in PMMA, and pads to contact them are structured by e-beam lithography (step IV). Ni contacts are then sputtered and the remaining PMMA removed by acetone. Finally the SU8 2002 layer is locally opened and Ni is sputtered using a shadow mask to form a gate contact for measurement.

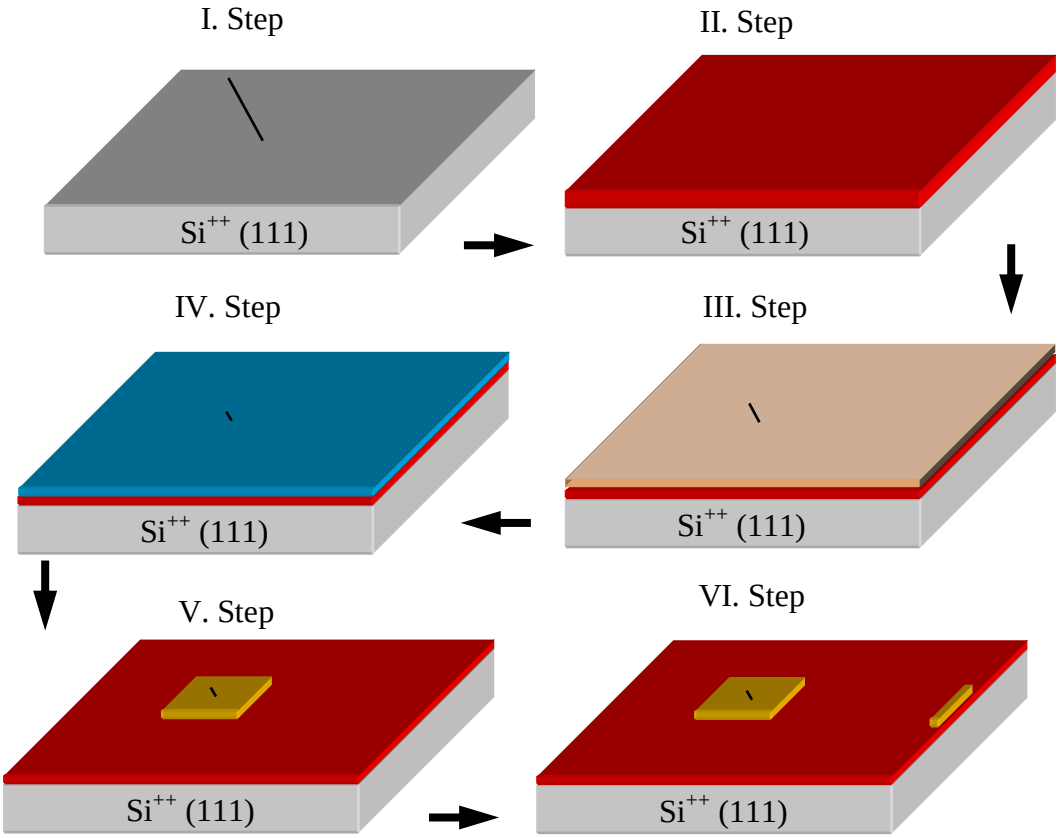

Figure 38: Process flow for in situ growth of a NW diode

Step I: Highly n-doped Si-NWs were grown on a highly p-doped (111) substrate (Si^{++}).

Step II: The substrate was covered by 3 µm of SU8 2002 resin (MicroChem GmbH, step II), followed by a hard bake.

Step III: The resin covered NWs were laid open by reactive ion etching (RIE).

Step IV: The NW's upper ends were covered by PMMA and pads were structured upon them by electron beam lithography.

Step V: Ni pads were sputtered and the PMMA removed by acetone.

Step VI: A back gate was added by locally scratching the SU8 2002 layer followed by sputtering Ni with a shadow mask.

4 Results and Discussion

4.1 Au, Ag, Cu and Pt-catalysed Si-NW synthesis grown with OCTS

For catalysed growth of Si-NWs Au has been the most commonly used catalyst since Wagner and Ellis [2] discovery of the VLS mechanism. Over the years Au was successfully used as catalyst for NWs with different composition at a wide range of process parameters and is therefore practically always the catalyst of choice when NW growth is the main aspect of the experiment. OCTS on the other side is a novel precursor compared to the more established SiH_4, Si_2H_6 or $SiCl_4$. Nonetheless it offers three Si-atoms per molecule, trice as much as SiH_4 or $SiCl_4$, and a very low dissociation energy compared to more established precursors (see chapter 2.1.6).

4.1.1 Au catalysed Si-NWs

According to section 3.1, samples were prepared and grown with OCTS as Si-precursor. 100 sccm of He were used to route the OCTS into the furnace for growth duration of 60 minutes. 80 nm Au colloids are used as catalyst to achieve better control over the NW density. Typical NWs and nanostructures grown this way, but at different growth temperatures, are shown in Figure 39.

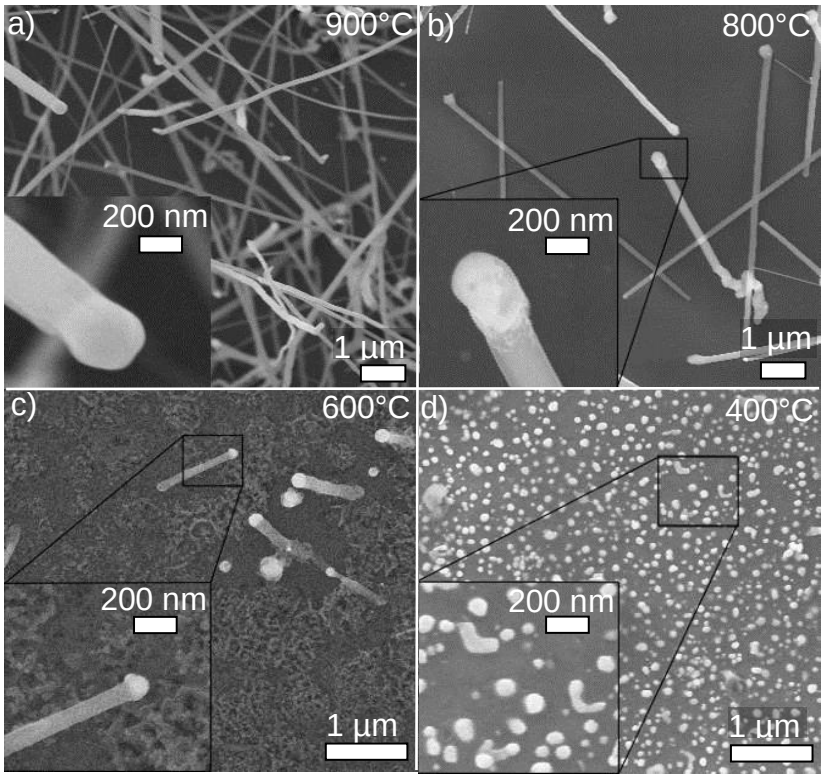

Figure 39: SEM images of nanostructures grown with OCTS as precursor and Au colloids (diameter 80 nm) as catalyst at growth duration of 60 min (enlarged views in the inset) at growth temperatures of:

a) 900°C

b) 800°C

c) 600°C

d) 400°C

At the highest temperature of 900°C (Figure 39a) densely grown NWs with a wide range of diameter from 50 to 500 nm and length up to 20 µm were observed. The appearance also varied strongly exhibiting bent, twisted or even kinked NWs, although the majority were straight.

Downstream at 800°C (Figure 39b) the NWs were more uniform with about 8 µm length and 100-250 nm thickness. The kinks were strongly reduced and nearly all NWs were perfectly rod-like.

Lowering the temperature to 600°C (Figure 39c) resulted in muscoid precipitations and very sparsely distributed NWs. These NWs were much shorter than their counterparts grown at higher temperatures, measuring only 1 µm in length and about

130 nm in diameter. At all temperatures between 600°C and 900°C catalyst particles were observed atop of the NWs, whose composition were verified to be Au/Si by EDX.

At the lowest investigated temperature of 400°C (Figure 39d), just the initiation of NW-growth could be observed, when tail like structures evolved from individual Au-particles.

Here it was possible to grow NWs at temperatures down to 600°C efficiently, what is not possible when using $SiCl_4$ as precursor. There are no examples in literature, where NWs were grown at temperatures below 850°C as it is not thermodynamically possible to break up the precursor below that temperature.

In literature, when working with $SiCl_4$ as precursor [63], the addition of H_2 is often recommended in order to increase growth rates and impede tempering of the NWs. H_2 reacts with the chlorine atoms and forms HCl, which etches the thin native oxide layer on the Si surface presenting a clean crystal surface for epitaxial NW growth. Sometimes HCl is also added intentionally to the SiH_4/H_2 feed gas for improving epitaxy [44]. So the next logical step was to add H_2 (20 sccm) to the feed gas. The samples grown with H_2 addition are shown in Figure 40.

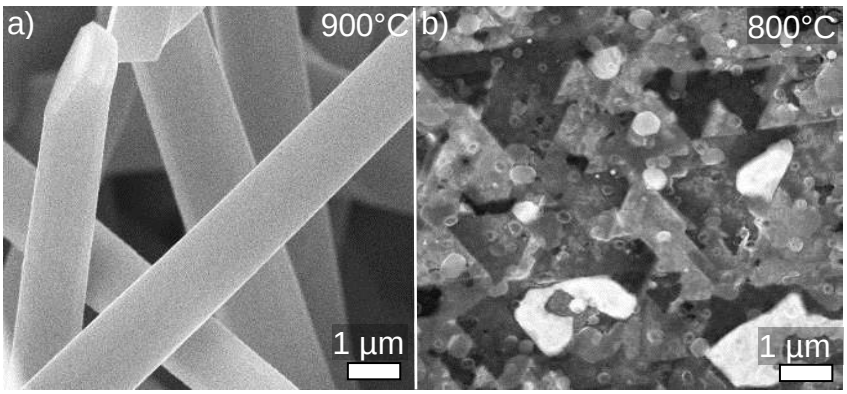

Figure 40: SEM images of nanostructures, which were grown with OCTS as precursor and with the addition of 20 sccm H_2 and a 2 nm Au layer was used as catalyst at growth temperatures of:

a) 900°C

b) 800°C

At the highest temperature of 900°C straight, unusually large NWs with lengths of more than 10 µm and diameters up to 2 µm (Figure 40a) were observed. At lower

temperatures etching is the dominant process. A growth temperature of 800°C leads to triangular shaped etching pits, characteristic for a (111) substrate (Figure 40b).

To understand the changes in growth behaviour it is necessary to investigate the decomposition mechanism of OCTS. As already mentioned in section 2.1.5 the decomposition mechanism can be described as follows.

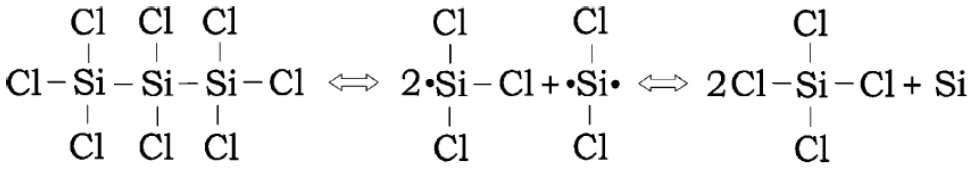

According to Ezhov [70] this decomposition reaction starts at 127°C, but becomes relevant at 627-727°C (Figure 41).

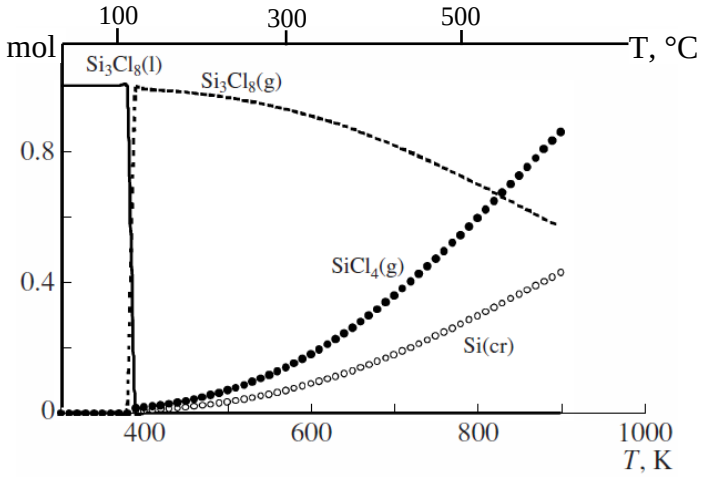

Figure 41: Thermodynamic equilibrium composition during heating of OCTS at p = 1 bar after Ezhov et al. [70]. In parenthesis the state of aggregation is depicted by l, g and cr (liquid, gaseous and crystalline).

Although Ezhov's work does not consider kinetic processes, it explains the trend of increasing growth rate with increasing temperature as more Si is generated at higher temperatures. If H_2 is added to the feed it either results in very thick NWs (900°C) or etching (800°C and below). The reason for the etching is that H_2 reacts with intermediate decomposition products and forms HCl. HCl is highly reactive at such high temperatures and forms volatile chlorosilanes with Si from the substrate, which easily evaporate and cause etching pits. At 900°C the mechanism is reversed and H_2 is mainly used to break up $SiCl_4$, a byproduct of the OCTS decomposition. Most NW growth experiments with $SiCl_4$ in literature [2,91] also take place at 900°C or higher. Therefore the following decomposition mechanism can be assumed at 900°C.

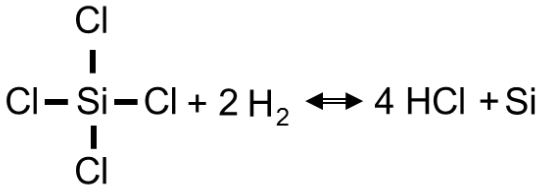

Hence additional Si is available for NW growth, leading to effective NW growth via VLS, but also enhances uncatalytic deposition, what results in extremely thick NWs.

After an extensive variation of temperature and H_2 addition, the optimal conditions for growing epitaxial, single crystalline Si-NWs with OCTS turned out to be:

- 80 nm Au colloids for tighter diameter distribution and better NW density control
- 50 sccm He
- 30 minutes tempering at 700°C
- 60 minutes growth at 800°C

The SEM pictures in Figure 42 show NWs grown at the optimal conditions with a 2 nm sputtered Au layer (a) and 80 nm colloids (b). The NWs are straight and the majority stands upright in both cases, although the diameter is still dependent on the catalyst particles size. Therefore the colloid grown NWs have a tight diameter distribution of about 90 nm, while the NWs grown with catalyst particles from a thermally aggregated layer vary strongly between 50 and 150 nm. Nonetheless the NWs grow epitaxially in both cases. The 30 minute tempering step at 700°C, when Si from the substrate is dissolved into the Au particle until saturation is reached, proved to be crucial to achieve epitaxy at this level. After that the NW growth can start with an already saturated particle in intimate contact with the substrate. The sputtered Au layer also produced shorter NWs (up to 4 µm), while the colloid grown NWs easily exceeded 10 µm. This is due to the larger amount of Au, which was deposited by sputtering, so the precursor had to be distributed among more particles, thus impeding growth of individual NWs. The larger amount of Au also explains the different growth rates of just 66 µm/min (sputtered layer) and 166 µm/min (colloids), as the same amount of precursor had to be distributed among altered amounts of catalyst.

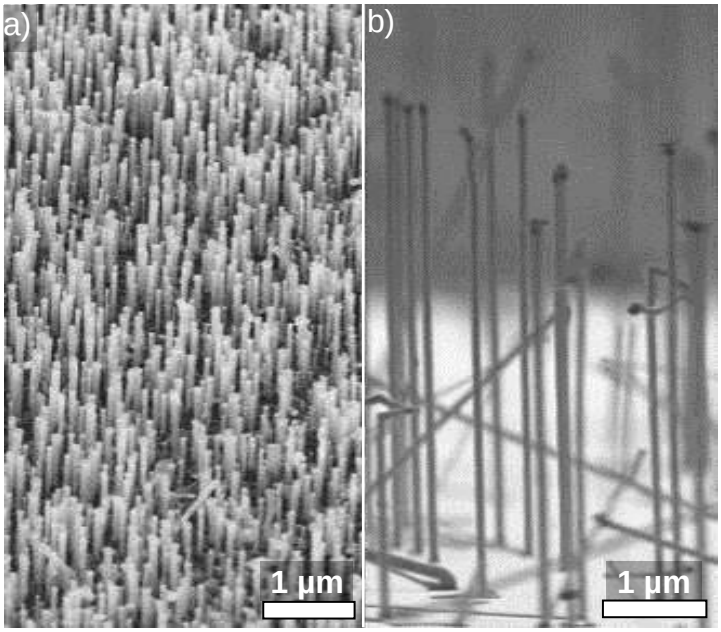

Figure 42: SEM images of Si-NWs grown at the optimal conditions with OCTS as precursor and catalysts as follows:

a) 2 nm sputtered Au layer
b) 80 nm Au colloids

Considering the high growth rates of 31 µm/min Lieber et al. [24] achieved using Si_2H_6, it was also intended to raise growth rates with OCTS. Hence the temperature of the saturator was raised, leading to an increase of the partial pressure of OCTS from 0.03 mbar to 2.9 mbar, the sputtered layer replaced with 80 nm colloids and the flow rate of He doubled to 100 sccm. The results can be seen in Figure 43. The growth rate for the samples grown with a partial pressure of 0.03 mbar was ~8 µm/h, as depicted earlier. When the partial pressure of the precursor was increased, the growth rate practically doubled to ~16 µm/h. Also the number of kinked NWs increased considerably, what can be expected at such large increase in partial pressure [13]. Another important side effect was the elimination of upright growing NWs at the higher partial pressure. This would agree with the work of Schmid et al. [58], where lower partial pressures favour upright NWs, while higher partial pressures surpress their growth.

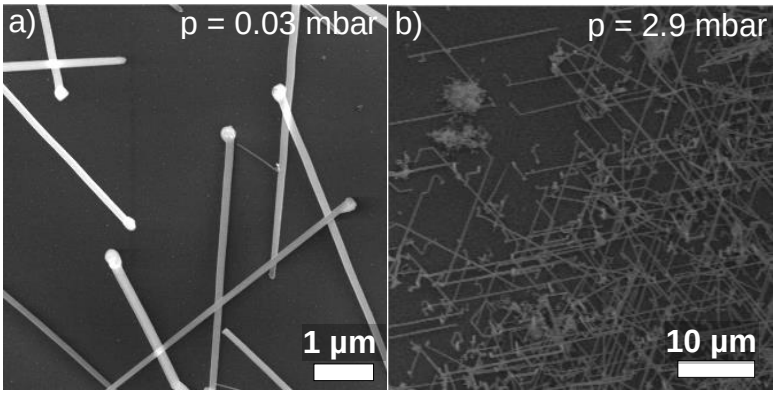

Figure 43: SEM images of OCTS grown NWs at 800°C with different partial pressures of OCTS:

a) $p_{(OCTS)}$ = 0.03 mbar
b) $p_{(OCTS)}$ = 2.90 mbar

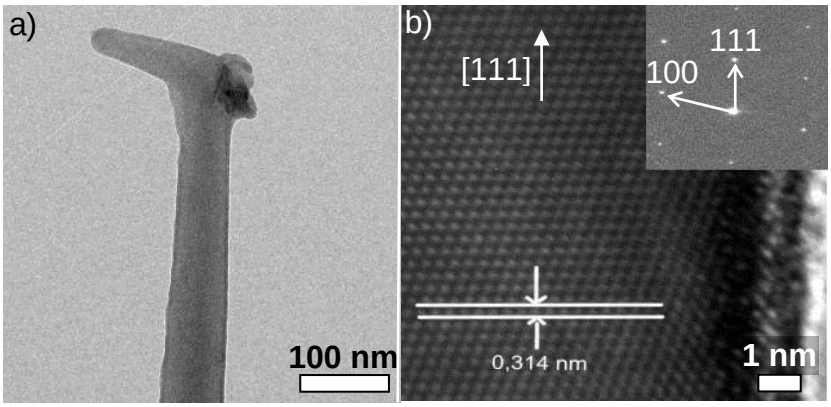

Figure 44: TEM images of an Au catalysed OCTS grown Si NW:

a) HRTEM
b) HRTEM revealing the NW's crystal structure. The inset indictes a [111] growth direction

TEM investigations of the Au catalysed NWs (Figure 44a) showed a slight tapering and an unusual tip shape. This tip may form during cooling, when the precursor's partial pressure drops at the end of the growth step and dissolved Si precipitates from the super-saturated Si/Au droplet. The tips, present on practically all NWs, were later investigated by means of EDX and identified as Au/Si alloys. A change in partial pressure can cause different growth orientation like shown by Lieber et al. [62], where NWs were grow in zig-zag-patterns due to partial pressure changes. Figure 44b shows a HRTEM of the Si NW with no observable defects or stacking faults and a plane spacing

of 3.14 Å, what fits the distance between two Si (111) planes. The SAED in the inset clearly identifies the growth direction to be [111].

4.1.2 Ag catalysed Si-NWs

Although Au is the most common and versatile catalyst for VLS grown NWs, it causes undesirable deep level traps in Si, which may deteriorate an electronic device's performance; e.g. shorten the non-radiative life time of charge carriers. Therefore alternative catalysts are highly preferred. In the following experiments Ag, Al, Cu, In, Ni, Pt and Ti were evaluated as Au replacements using the same setup and growth parameter variance to achieve epitaxial NW growth.

Ag is an attractive alternative to Au as catalyst, what was proven by Schmidt et al. [67]. Its binary phase diagram with Si (Figure 10c) shows no silversilicides, what indicates the same chemical inertness as Au. Unfortunately the eutectic point lies at 835°C, what makes higher growth temperature a necessity. However Ag also features less efficient deep level traps than Au (Figure 11).

For these experiments 2 nm of Ag were deposited as catalyst by thermal evaporation. Otherwise the samples were processed analogously as in case of Au. The growth results can be seen in Figure 45.

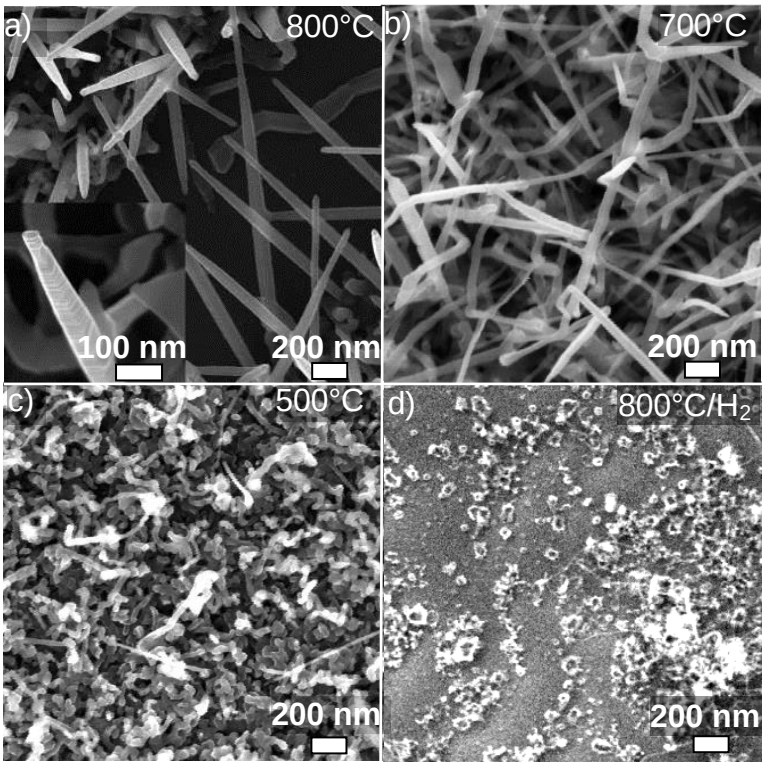

Figure 45: SEM images of Ag catalysed OCTS grown Si-NWs at:

a) 800°C without H_2
b) 700°C without H_2
c) 500°C without H_2
d) 800°C with H_2

Ag catalysed NWs grown at 800°C (Figure 45a) featured a very block like appearance with strong faceting below the tip. The NWs measured 100 to 200 nm in diameter and 1 to 5 µm in length. At 700°C (Figure 45b) the NWs exhibit kinks and are strongly bent with a profound tapering. Their thickness is reduced with 100 nm in diameter, while their length increases to over 10 µm. Further down at 500°C (Figure 45c) NWs still grow, but are by far outnumbered by bulky nanostructures covering the entire sample. Their geometry is further reduced to about 30 nm in diameter and 1 µm in length at most. All this samples were grown without any H_2 as it suppresses NW growth at temperatures between 400 and 900°C. Figure 45d serves as an example for this, because just uncatalytic deposits were found at a growth temperature of 800°C in the presence of H_2.

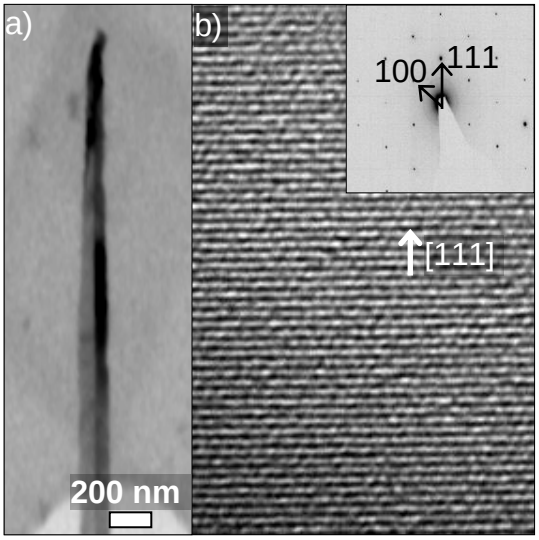

Figure 46: TEM images of a typical Ag catalysed NWs grown at 800°C with OCTS as precursor:

a) HRTEM; A twin crystal runs along the NW's growth direction
b) HRTEM revealing the NW's crystal structure. The inset indictes a [111] growth direction

TEM investigations of Ag catalysed NWs grown at 800°C revealed frequent formation of twin crystals along the NW's growth axis. The grain boundary is clearly visible in the TEM image in Figure 46a. Schmidt et al. [67] yielded similar results in their work, which also revealed that Ag tend to cause twinning in Si-NWs. The dark parts in the TEM originate from thickness contours due to the tapering and faceting, as already deduced from the SEM images (Figure 45a). It is also possible that the dark regions are signs of stress due to the twinning of the NWs. Figure 46b shows a HRTEM image of the {111} planes representing a [111] growth direction, which is confirmed by the indicated SAED in the inset. This image originates from the centre of one of the twins. No observable faults were found in this region of the NW. Hence it can be said, that the twins itself are of good crystallinity.

4.1.3 Cu catalysed Si-NWs

Cu has been implemented for NW growth in several works, such as to grow ZnO-NWs on a Si substrate [92], catalysing In_2O_3-NWs synthesis [93] and of course to grow Si-NWs [94]. Depending on the experimental setup in these works the growth mechanism can be very complex due to the many mixed crystals Cu and Si can form.

Within this work a 2 nm sputtered layer of Cu was deposited on a Si (111) wafer piece and processed analogously to the growth experiments using Au as catalysts. The results can be seen in Figure 47.

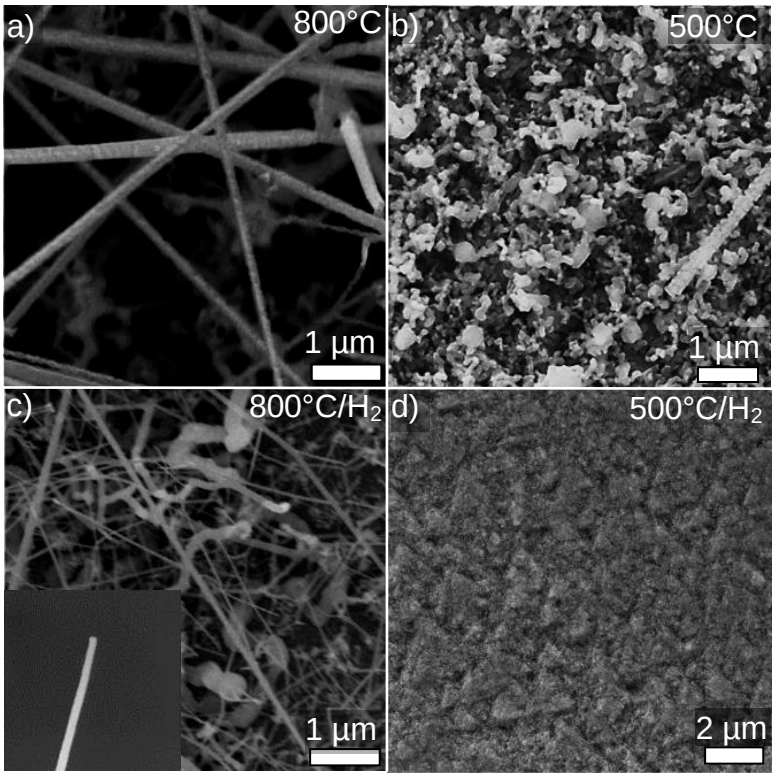

Figure 47: SEM images of Cu catalysed Si-NWs and nanostructures grown with OCTS as precursor at:

a) 800°C; Straight NWs with minor occurrence of uncatalytic deposits
b) 500°C; Mainly uncatalytic deposits
c) 800°C with 20 sccm of H_2 added; densely with NWs populated sample
d) 500°C with 20 sccm of H_2 added; severe etching with characteristic pit formation

At 800°C the NWs were 50 to 200 nm thick and at least 5 µm long (Figure 47a), but strongly facetted. Downward at 500°C (Figure 48b) no etching was observed. Instead uncatalytic deposits covered the whole sample.

The addition of 20 sccm H_2 at 800°C (Figure 47c) resulted in densely populated samples. The NWs were up to 20 µm long and had diameters in the range of 20 to 400 nm. In general the NWs featured a wide length and diameter distribution with most of them bent. Also most of the NWs were tapered and no catalyst particle could be observed atop of them (see inset of Figure 47c). At the lower temperature of 500°C

(Figure 48d) severe etching occurred and produced triangular etching pits. Simultaneously to the etching also uncatalytic deposition of amorphous Si was observed across the sample.

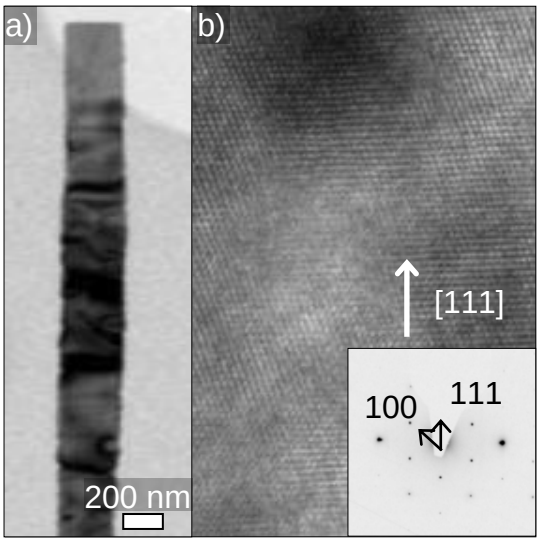

Figure 48: TEM images of a typical Cu catalysed NW with OCTS as precursor:

a) HRTEM; the dark stripes indicates strong stress and tensions inside the NW
b) HRTEM revealing the NW's crystal structure. The inset indictes a [111] growth direction

TEM investigations of Cu catalysed NWs revealed a high level of stress indicated by dark stripes and rough surface in Figure 48a, which can be attributed to mixed crystal formation. The bright and dark regions in Figure 48b are probably originating from coppersilicide inclusions, which cause stress to the lattice. Nonetheless the NW features good crystallinity and clearly a [111] growth direction (inset). Unlike Ag or Au, Cu can form several mixed crystals with Si, like Cu_3Si, the so-called η–modification, (see Figure 10d for details) depending on temperature and the amount of incorporated Cu in the NW.

4.1.4 Pt catalysed Si-NWs

For Pt as catalyst a 2 nm layer was sputter deposited and were investigated analogously to the Au catalysed samples after the same synthesis procedure. The results of these experiments can be observed in Figure 49.

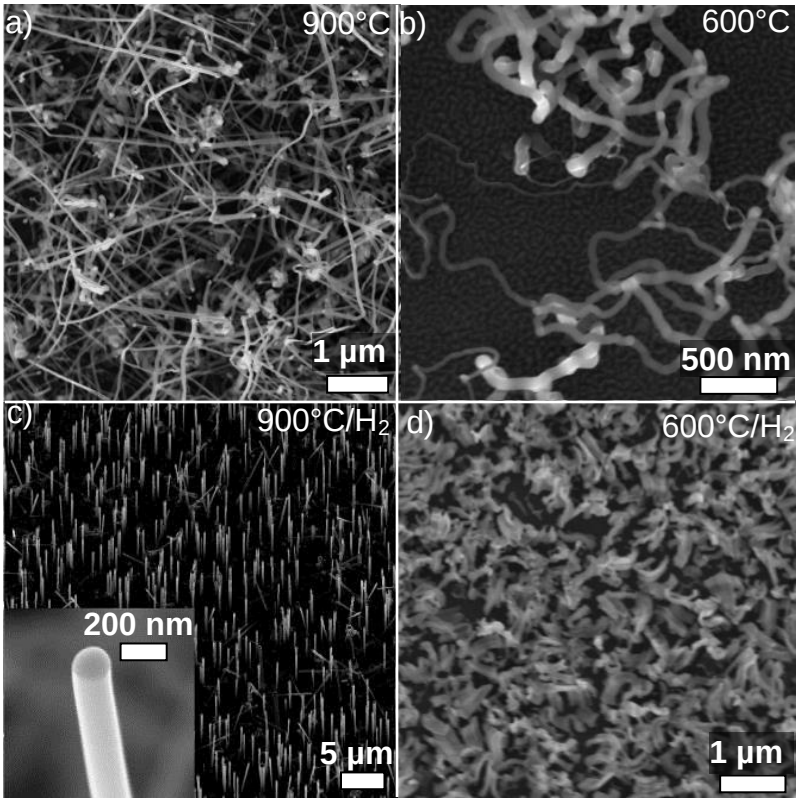

Figure 49: SEM images of Pt catalysed NWs grown with OCTS as precursor at:

a) 900°C
b) 600°C
c) 900°C with 20 sccm H_2 added
d) 600°C with 20 sccm H_2 added

At the highest growth temperature of 900°C (Figure 49a) the samples were densely populated with kinked and bent NWs. Nonetheless a Pt/Si particle was found atop of every NW and their geometry were about 5 µm in length and 30 to 100 nm in diameter. At the lower temperature of 600°C (Figure 49b) the bending was more pronounced with the NWs crawl over the substrate's surface. Diameters from 100 nm down to 10 nm were measured, while the length varied between 0.5 and 3 µm. The addition of 20 sccm H_2 to the growth atmosphere notably improved the NWs' quality. A growth temperature of 900°C (Figure 49c) resulted in epitaxial, straight, upright NWs with a length of about 6 µm and 160 to 200 nm in thickness. The growth perpendicular to the surface of the (111) substrate indicates a [111] growth direction. Atop of these NWs a Pt/Si particle was verified by means of EDX. At 600°C (Figure 50d) the presence of H_2 caused intertwined nanostructures, which were severely bent and covered the whole sample.

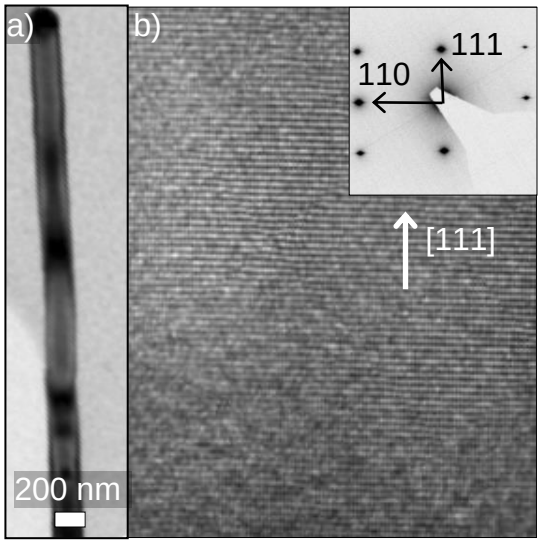

Figure 50: TEM images of a typical Pt catalysed NW grown with OCTS as precursor:

a) HRTEM; the dark spots reveal stress and tension inside the NW as well as thickness contours
b) HRTEM revealing the NW's crystal structure. The inset indictes a [111] growth direction

TEM investigations of Pt catalysed NWs (Figure 50) clearly revealed a [111] growth direction (inset), equal to the Au, Ag and Cu catalysed NWs. The dark spots reveal stress and tension inside the NW as well as thickness contours on the rims of the NWs, what is clearly visible right under the catalyst particle. Otherwise no crystal defects could be detected and the HRTEM images confirm a straight habitus, which was already observed in SEM pictures, and the presence of a Pt/Si particle atop of the NW.

4.1.5 Discussion of NW synthesis via Au, Ag, Cu and Pt mediated VLS-growth

Concluding it can be said, temperatures of at least 700°C are necessary to grow NWs with OCTS in sufficient quality and quantity independently of the catalyst. The very low partial pressure of just 0.03 mbar contributes to this problem, as there is a very low concentration of OCTS in the growth atmosphere, when the saturator is operated at room temperature. Lower temperatures seem to favor uncatalytic deposition, etching of the substrate or deterioration of the NW's quality in general. The reason for this is

complex and depends on a lot of adjustable parameters, but can be mainly attributed to surface energies, which are strongly influenced by temperature. Also the higher conversion rate of the precursor at elevated temperature influences the surface tension (see Equation 12), because more Si and other decomposition products are available to influence the surface energies. Hence higher temperatures and the presence of more surface active molecules at these temperatures cause a decrease of surface tensions at the interfaces between growth atmosphere, NW surface and catalyst particle, which further results in reduced inner pressure (p_{in}). With lower p_{in} the gaseous precursor or its decomposition products can enter the catalyst particle more easily and therefore nucleation and NW growth are highly favored this way.

The addition of H_2 is another parameter which can alter growth behaviour fundamentally. Adding H_2, OCTS and $SiCl_4$ can be converted into Si more easily and results in the formation of gaseous HCl. Thus HCl can etch undesired SiO_2 at low concentrations and provide a clean surface for improved epitaxy. Higher concentrations of HCl on the other side effectively etch the substrate resulting in characteristic triangular etching pits. The change in surface energies that is induced by the presence of H_2 cannot be neglected either.

4.1.6 NW synthesis via Au, Ag, Cu and Pt mediated VSS-growth

It is generally accepted for the VLS mechanism that the growth temperature should be higher than of the lowest eutectic point in the binary phase diagram. With OCTS this applies for Au (363°C eutectic point – 700°C growth with OCTS) and Pt (830°C – 900°C), but not for Cu (802°C – 800°C) and Ag (835°C – 800°C). So reaching the liquid regime is not mandatory to produce NWs when OCTS is used. NW growth can also be achieved through the VSS (Vapour-Solid-Solid)-mechanism.

Taking a closer look at the used catalysts, Ag catalysed single crystalline Si-NWs have already been reported by Wagner and Ellis [95] in 1965 at high temperatures of 950 - 1050°C. Also Nebol'sin et al. [96] reported the successful growth of Ag catalysed Si NWs with growth rates of 1.5 µm/s. Surprisingly the Ag particle did not evaporate in their LPCVD equipments, although the vapor pressure of Ag reaches a value close to 10^{-2} mbar at 1000 °C [97]. Theoretically sub-eutectic NW growth with Ag as catalyst should not be possible as there is no Si solubility in Ag below the eutectic point (see Figure 10c). Nonetheless in this work as well as in the work of Tatsumi et al. (amorphous NWs, [98]) NWs were produced via a VSS mechanism at 700 – 800°C and

650°C respectively. Meanwhile further research on the Ag/Si phase diagram revealed a solubility of 0.2 at% at 650°C and 0.9 at% close to the eutectic point, that also theoretically explains the Ag catalysed VSS growth [99].

Sub-eutectic, Cu catalysed NWs were also reported by Wen et al. [94] and Arbiol et al. [68], although at temperatures between 500 and 650°C. According to Arbiol et al. the Cu particle undergoes several phase transformations before a NW can precipitate. Starting with a pure Cu particle, Cu_5Si forms firstly. Depending on the growth temperature several modifications like the ε, γ, β and κ-phases can form. At the growth temperature in our work the particle would first form κ, then β and subsequently δ coppersilicide. When the Si share rises further Cu_3Si will be generated in the η, η' or η'' modification, depending on the temperature. In this case it will be the η modification (see Figure 10d), from which NWs precipitate. It should be noted, that this mechanism is derived from a binary phase diagram, which applies for bulk material at equilibrium and does not take dynamic influences like surface energy changes or kinetics into account. Arbiol also observed a tapering of NWs starting at 650°C, that he attributed to either the integration of the catalyst into the NW during growth or the migration of the Cu to neighboring NW tips. As there were no catalyst particles found on the NW tips in this work, it was concluded, that the Cu was indeed consumed by the NW during growth and tapering appears as a logical consequence of the subsequently shrinking catalyst particle.

Concerning Pt catalysed Si NWs, successful synthesis under subeutectic conditions has been achieved by Garnett et al. [100] and by Sekhar et al. [101] at temperatures of 1200°C, so definitely involving a liquid phase. The Pt/Si phase diagram (Figure 10f) reveals a very complex sequence of phases the particle undergoes at the growth temperature of 900°C used in this work. Starting with a pure, solid Pt particle, Si is dissolved steadily into it until the Si content reaches 1.4 at%. At this ratio the particle becomes partially liquid and consists of a liquid Pt/Si phase and a solid Pt phase. Meanwhile the Si content rises further and the particle becomes completely liquid at ~22at%. Reaching 25 at% the particle solidifies again and forms β-$Pt_{12}Si_5$. Then after transiting into β-Pt_2Si and Pt_6Si_5, the particle finally turns into PtSi, from which Si NWs can precipitate when the Si content exceeds 50 at%. Also Baron's [66] work identifies PtSi islands as the phase from which Si NWs precipitate. So we can conclude that Pt catalysed Si-NWs grown via the VSS mechanism, although the particle passes through a liquid regime in the initial stage of the growth mechanism.

Also all of the investigated NWs show the most common [111] orientation for which {112} facets were found in a previous work [102]. This is in agreement with the work of Schmidt et al. [59], who revealed a diameter dependence of the NW's crystallographic orientation. NWs of 20 nm thickness and below favor a [110] orientation, while greater diameters tend to grow in [111] direction (Figure 13).

4.1.7 Al catalysed Si-NWs

Al has been successfully used as NW catalyst by Gösele et al. [39]. In this work a 2 nm layer was sputter deposited and investigated analogously to former NW catalysts. The results of the growth experiments are shown in Figure 51.

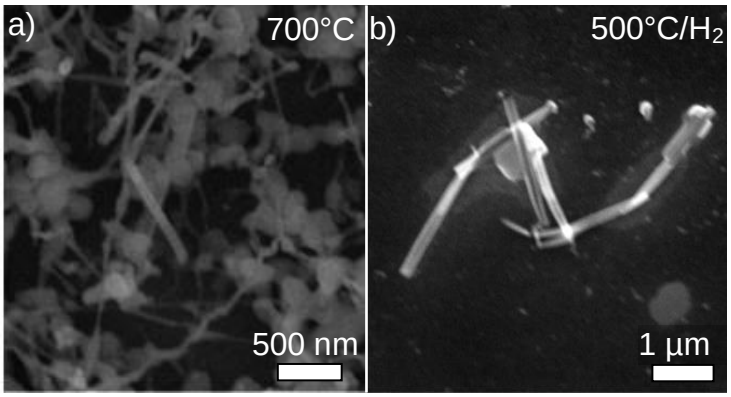

Figure 51: SEM pictures of NW growth experiments with OCTS as precursor and Al as catalyst at:

a) 700°C; very short and irregular shaped NWs, along with uncatalytic depositions are encountered
b) 500°C ; The addition of H_2 resulted in less uncatalytic depositions, but did not affect NW growth itself

The experiments with Al as catalyst lead to very short, 1 µm at most and unevenly shaped NWs at 700°C, which were intertwined with uncatalytic deposits as shown in Figure 51a. The addition of 20 sccm H_2 at 500°C, shown in Figure 51b, suppressed the formation of uncatalytic deposits, but also led to unevenly shaped NWs. With up to 3 µm length and a diameter of about 100 nm they were also no improvement to their counterparts grown without H_2 grown. At higher temperatures (800°C and above) no NWs or catalyst particles were found. This can be attributed to the reaction of Al with Cl from the precursor to form volatile $AlCl_3$, which easily evaporates at such high temperatures.

Successful NW synthesis with Al as catalyst was conducted by Wacaser et al. [103] and Gösele et al. [39]. In both works UHV conditions, according to Wacaser et al. at a maximum pressure of 10^{-6} Torr, were necessary to allow proper NW growth. Otherwise the very stable Al_2O_3 forms an isolating layer around the Al particle and prevents any Si from entering the potential NW seed. Unfortunately it was not possible to reduce the oxygen content to such a level with the APCVD used in this work and the results are a proof, that the O_2 content is too high.

4.1.8 Ti catalysed Si-NWs

Ti was also considered a promising candidate for NW growth with OCTS, as Sharma et al. [45] have already demonstrated Ti's applicability with $SiCl_4$ as precursor. As before, a 2 nm layer was sputter deposited on the substrate. The growth results are shown in Figure 52.

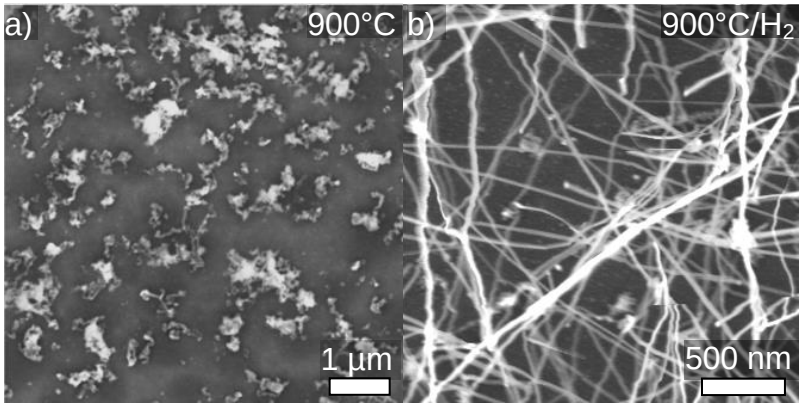

Figure 52: SEM images of Ti catalysed NWs grown with OCTS as precursor at temperatures of 900°C:

a) Without H_2; Only uncatalytic deposits were encountered
b) With 20 sccm H_2 added; densely populated with irregularly shaped and rarely straight NWs

Ti as catalyst delivered quite similar results as Al without the addition of H_2 at 900°C (Figure 52a). In this case uncatalytic deposits were also found in rich quantities. 20 sccm of H_2 improved the growth behaviour considerably (Figure 52b) and led to long (up to 5 µm) and very thin (~50 nm) NWs, which very unfortunately strongly bent, featured zigzagging and generally an uneven habitus.

Ti catalysed Si NWs were produced by Sharma et al. [45]. As Ti, like Al, has also a very strong affinity to O_2, an annealing step in H_2 under low pressure was necessary to eliminate oxides and ensure proper NW growth. In this work Sharma et al. also investigated the importance of HCl for the growth as it removes uncatalytic deposition at the sidewalls of the NWs during growth. Without HCl the NWs became strongly tapered and experienced a rough surface. This agrees with the results in this work. Also the addition of H_2, which subsequently forms HCl with OCTS at 900°C, removes the uncatalytic deposits. Nonetheless the NWs grown in the presence of H_2 still feature a rough surface similar to Sharma's work. So it can be assumed that the uncatalytic deposits have not been removed completely by HCl due the low concentration of precursor used in these experiments. Another reason for the poor quality of our Ti catalysed NWs may be the presence of O_2 during growth. Analogously to Al catalysis one can expect formation of very stable TiO_2, which acts in a similar way as Al_2O_3.

4.1.9 In catalysed Si-NWs

In was also considered a potential NW catalyst, as Yu et al. [104] had demonstrated successful Si-NW growth. A 2 nm layer was sputter deposited on the substrate. The results are displayed in Figure 53.

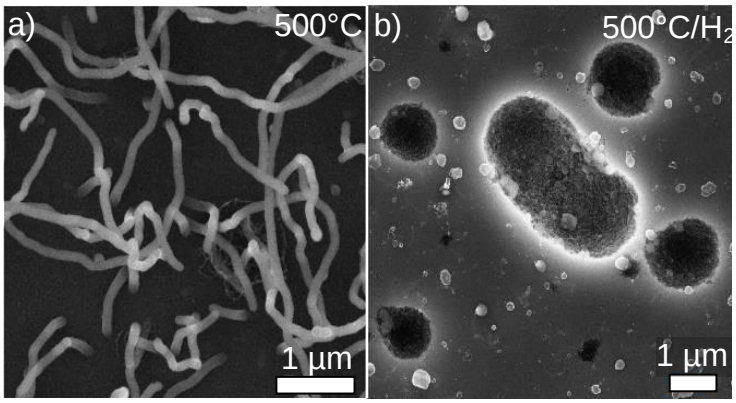

Figure 53: SEM images of In catalysed NWs grown with OCTS as precursor at temperatures of 500°C:

a) Without H_2; Only unevenly shaped NWs were encountered
b) With 20 sccm H_2 added; only round etching pits were found on the substrate

In catalyses strongly bent, worm like NWs at 500°C (Figure 53a) in large numbers. Again the NWs were not very long (up to 4 µm) and featured a diameter of about 80 nm. Analogously to the experiments with Al and Ti, 20 sccm of H_2 were added to improve NW growth, but resulted in round etching pits (Figure 53b) with diameters ranging from 1 µm up to 3 µm.

In as catalyst was thoroughly tested by Yu et al. [104] and Wang et al. [105], both using plasma enhanced CVD. Surprisingly the In droplets in these two works experienced a very large contact angle (140-160°) compared to an Au droplet (95-115°). Such a contact angle leads to unusually large, ball like catalyst particles during growth with NW diameters far smaller than the catalyst particle itself. Wang et al. also conducted extensive TEM investigations with very interesting results on their NWs. Four different crystallographic orientations, namely [100], [111], [211] and [311], were found depending on the size of the In particle. In this work we did not encounter structures similar to the ones Wang and Yu presented. Therefore it can be assumed that there is a severe difference in surface tension, which is due to the utilization of OCTS and the changed pressure during growth and prevents the formation of proper NWs. The addition of 20 sccm H_2 (Figure 53b) resulted in severe etching, covering the substrate with round etching pits, which were up to 3 µm in diameter. Yu [104] also encountered etching of amorphous Si, when using H_2. Therefore we can assume, that the NWs in Figure 53a are also amorphous, which explains their rough habitus.

4.1.9 Summary of OCTS grown and with Al, Ti and In catalysed Si-NWs

To summarize the experiments with Al, Ti and In, neither of these catalysts proved suitable for proper NW growth. Al and Ti are materials with an enormous affinity to oxygen, thus requiring a UHV apparatus to exclude practically all oxygen from the growth atmosphere, what was impossible with the APCVD used in this work. Successful NW synthesis with these catalysts was conducted by Gösele et al. (Al, [39]) and Sharma (Ti, [45]) using UHV conditions. When working with In a plasma enhanced CVD seems necessary as Yu et al. [104] and Wang et al. [105] have demonstrated.

In total the NWs grown with Al, Ti or In were not epitaxial and therefore were not considered in any further experiments as other catalyst provided much more promising results.

4.2 $NiSi_2$ catalysed Si-NWs grown with OCTS

After the fruitful experiments with Au, Ag, Cu and Pt as catalyst for VLS synthesis of Si NWs with OCTS as precursor, Ni was tested as a potential Au replacement. Therefore a 2 nm thick layer of Ni was sputter deposited onto a piece of a Si (111) wafer analogously to the Au experiments. Contrary to previous experiments, the sample was not tempered for 30 minutes at growth time to produce a Si saturated particle. Instead the sample was pushed into the furnace with OCTS already added to the atmosphere. The results can be seen in Figure 54.

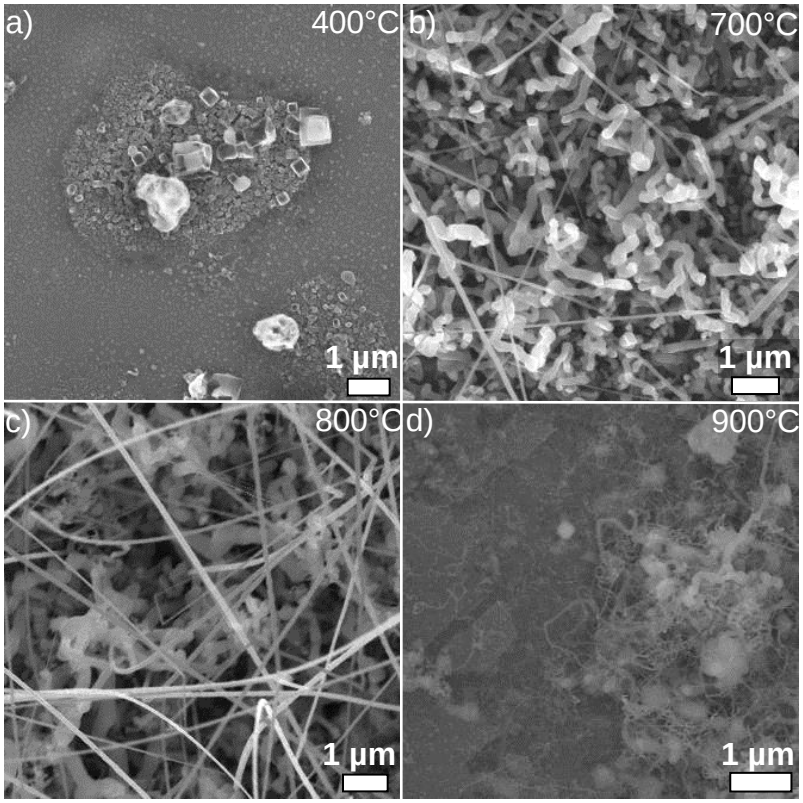

Figure 54: SEM images of OCTS grown NWs catalysed by $NiSi_2$ and nanostructures grown at temperatures of:

a) 400°C
b) 700°C
c) 800°C
d) 900°C

2 nm of sputtered Ni served as initial growth catalyst.

At the lowest investigated growth temperature of 400°C (Figure 54a) no NWs were observed, but instead cubical-shaped structures with edge lengths of 100 nm up to 1µm were sparsely encountered over the sample. EDX investigation confirmed that these nanostructures consisted partially of Ni. At the higher growth temperature of 700°C (Figure 54b) the substrate was covered by entangled, angled nanostructures covering the whole surface, measuring about 100 nm in diameter and a few µm in length. Between these nanostructures several µm long and less than 100 nm in diameter perfect rod-like NWs were encountered. An increase in growth temperature to 800°C (Figure 54c) resulted in a greater number of strongly bent NWs, but the substrate is still mostly covered by intertwined, more bulky structures. The geometry of these NWs is practically equal to those grown at 700°C. At the highest temperature of 900°C (Figure 54d), the substrate became rough due to enhanced etching by Cl_2, a byproduct of OCTS decomposition, and only a few clusters were encountered, which appeared to be covered by ravel-like, very thin nanostructures, with diameters smaller than 50 nm.

The addition of H_2 caused etching or uncatalytic deposition at all investigated temperatures except for 900°C. At this temperature, additional Si from $SiCl_4$ becomes available (see 2.1.5). The 30 minute tempering step, which proved critical for epitaxy with the former catalysts, was skipped as the high diffusion rate would dissolve the Ni completely into the substrate before NW nucleation could occur; especially at high temperatures. Also the flow rate played an important role in determining the NWs' appearance (Figure 55).

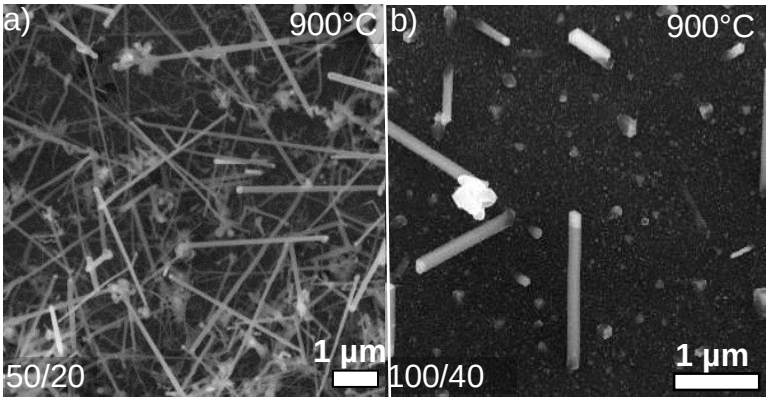

Figure 55: SEM images of OCTS grown NWs catalysed by $NiSi_2$ and nanostructures grown at temperatures of 900°C:

a) OCTS was applied with $He:H_2$: 50:20 sccm to the growth atmosphere; Densely populated samples with uncatalytic deposits between the NWs were encountered
b) OCTS was applied with $He:H_2$: 100:40 sccm to the growth atmosphere; Square shaped NWs with remarkable bright tips were found across the sample

A flow rate of $He:H_2$: 50:20 sccm resulted in densely with NWs covered samples. The NWs were remarkably long (up to 10 µm) with diameters ranging from 100 nm to 200 nm (Figure 55a). Their appearance was straight, and every NW clearly featured a bright catalyst particle atop. Increasing the flow rate to $He:H_2$: 100:40 sccm reduced the number of NWs, but completely changed their crystallographic habitus to square shaped (Figure 55b). Now the NWs also grow epitaxial, but still showed the bright tip, which differed strongly in length for different NWs. Their diameters ranged from 80 to 200 nm and they were up to 5 µm long.

4.2.1 Prismatic $NiSi_2$ catalysed NWs

As the NWs in Figure 55 appeared to be prismatic, a rather unusual shape for a VLS-grown NWs, a thorough characterisation of their crystallographic properties and characteristics was conducted.

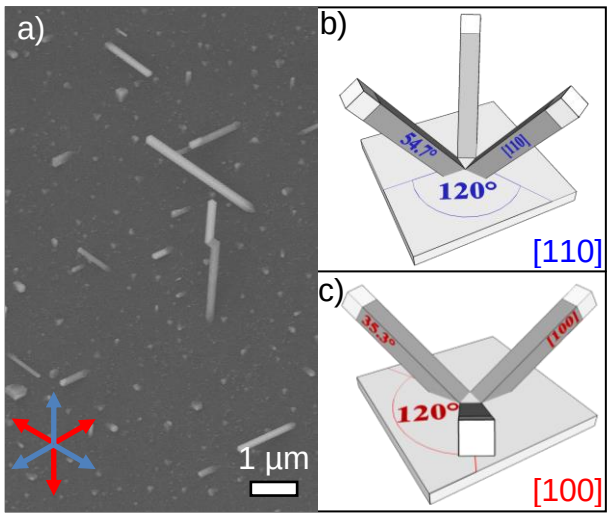

Figure 56: a) SEM image of epitaxial Si-NWs with OCTS as precursor catalyzed by OCTS;

b) Schematic of epitaxially grown [110] Si-NWs featuring an azimuth of 120° between the NWs and an angle of 54.7° with respect to the Si (111) substrate

c) Schematic of epitaxially grown [100]-NWs featuring an azimuth of 120° between them and an angle of 35.3° with respect to the (111) substrate.

Remarkably, two types of growth directions were observed on the very same sample and therefore under identical growth conditions (see Figure 56a). The first group of epitaxial Si-NWs with an azimuth of 120° between them and an angle of 54.7° with respect to the Si (111) substrate forms a triangular network in the top view SEM image. According to the schematic shown in Figure 56b, these nanowires are of [110] growth orientation. The second group that can be identified with the same azimuth but an angle of 35.3° to the substrate are predictable to be [100]-oriented NWs. As shown in the schematic of Figure 56c, such [100] oriented NWs form also a triangular network, shifted by 60° in comparison to the [110] oriented NWs, in the top view SEM image (see Figure 56a).

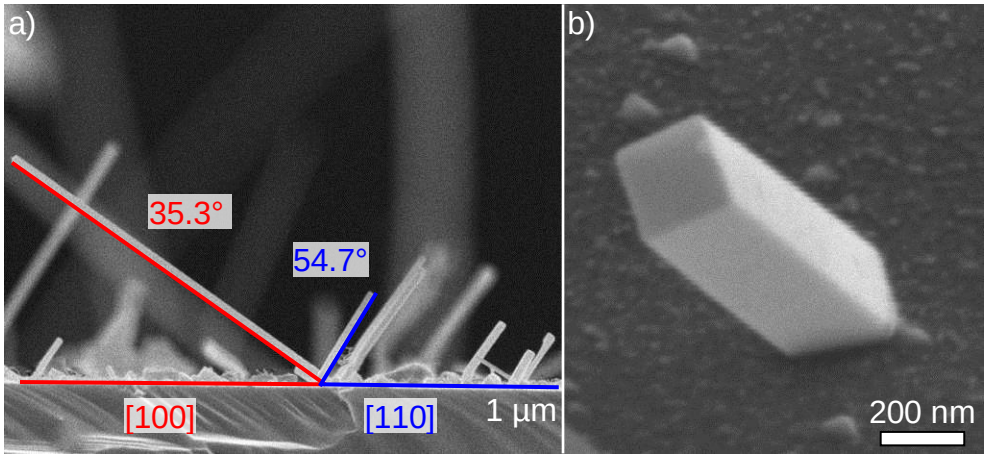

Figure 57: a) Side view SEM image of OCTS grown, $NiSi_2$ catalyzed [100] and [110] oriented Si-NWs with azimuths to the substrate of 35.3° and 54.7°, respectively
b) Highly resolved SEM image of an individual, prismatic OCTS grown, $NiSi_2$ catalyzed Si-NW.

Tilted SEM pictures in Figure 57a confirmed the calculated angles between the NWs and the substrate of 35.3° for [100] NWs and 54.7° for [110] NWs. Also the prismatic habitus of such grown NWs is unambiguously shown this way (Figure 57b).

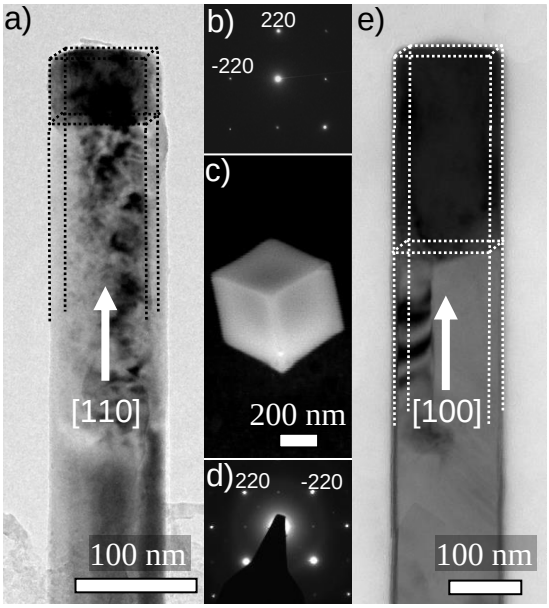

Figure 58: TEM-images of the OCTS grown, $NiSi_2$-catalysed square-shaped Si-NWs show [110] (a) and [100] (e) growth orientations. The dark speckles within the wires below the catalytic particles arise from diffraction contrast produced by lattice defects. SAED patterns in b) and d) proves the growth directions of [110] and [100] of the NWs respectively. c) displays a clear impression of the square habitus of the catalytic particles.

The TEM investigations in Figure 58 confirmed the deduced orientations of the two kinds of NWs (Figure 58b and d), but also revealed a lot of stacking faults and dislocation loops along the whole NW, but especially subsequent to the catalytic particle (Figure 58a and e). As these defects were encountered beneath practically every catalyst particle this may also be the limiting factor in terms of length wise growth. So a high concentration of defects terminates the longitudinal growth of the NW, what would explain the wide length distribution, which ranges from 5 µm down to stubs of just a few nm (Figure 55b). Also the square habitus can be deduced from the lack of thickness contour across the NW, which would not be the case for a non-rectangular cross section. The dark-field image in Figure 58c then clarifies the rectangular habitus by viewing a short, but definitely square NW. EDX measurements and SAED investigations of the catalytic particle showed a composition of about 33% Ni and 66% Si and revealed the space group to be Fm-3m/225 with a lattice constant to be 5.406 Å, in good agreement to cubic α-$NiSi_2$ [106].

Further TEM investigations were performed to investigate the alignment of the catalyst particle with respect to growth orientations of the Si-NWs. The alignment

between the catalyst tip and the NW itself and the facets of the prismatic NWs were of special interest in this case. The results of these measurements can be seen in Figure 59.

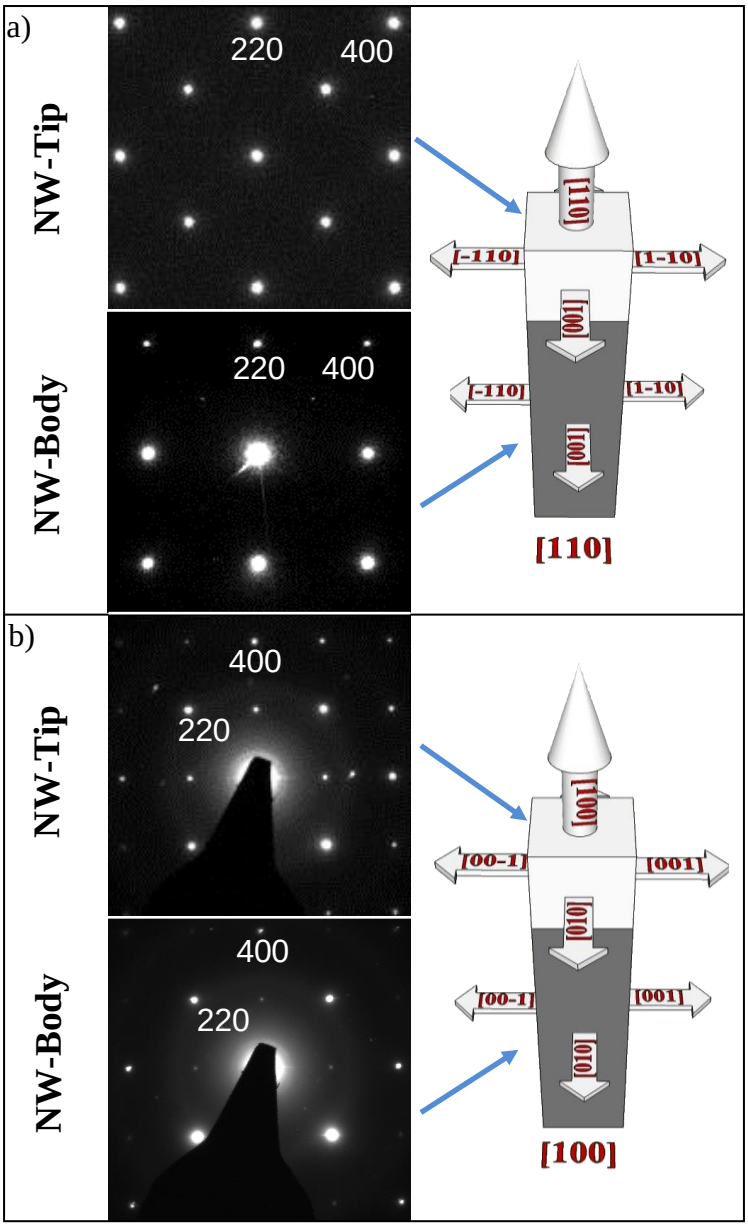

Figure 59: SAED images of the tip and body of the respective OCTS grown, $NiSi_2$ catalysed Si-NWs show the same alignment for body and tip. The schemata to the right illustrate the growth- and facet-orientation of the NWs.

a) [110] growth direction
b) [100] growth direction

It turned out, that in both cases the α-$NiSi_2$ tips were aligned in the same direction as the Si NWs. In case of the [110] oriented NWs the investigations revealed <100> as well as <110>, facets which were aligned perpendicular to each other, forming the

square habitus (Figure 59a). For the [100] oriented NWs a combination of <100> plains formed the square habitus (Figure 59b). The indexed SAEDs in Figure 59 clearly show the facets aligned in these directions.

After having confirmed the growth orientations and the square habitus by TEM investigations, naturally the question about the growth mechanism of these unusual NWs came up. Keeping in mind that the lowest eutectic point in the Si/Ni system lays at 966°C, one cannot assume a classic VLS mechanism, but a VSS mechanism. At the beginning of the process the catalyst particle consists of pure Ni. According to Figure 60a (a detailed section of Figure 10e) the growth temperature of 900°C is sufficient to form α–$NiSi_2$. The precursor continously supplies Si, which is dissolved into the catalyst particle until it reaches supersaturation, pure Si will be precipitated, what forms the NW. In this context one should expect a strong lattice mismatch which cause severe stress in the crystal and therefore instability, but in fact the difference in lattice constants between pure Si (5.4282 Å) and α–$NiSi_2$ (5.4080 Å) is just 0.37 %. So it is still possible for this binary compounds to precipitate crystalline structures. Unfortunately the TEM investigations revealed a very high concentration of defects all over the NW, which is very likely due to this mismatch of the lattice constants (Figure 60b).

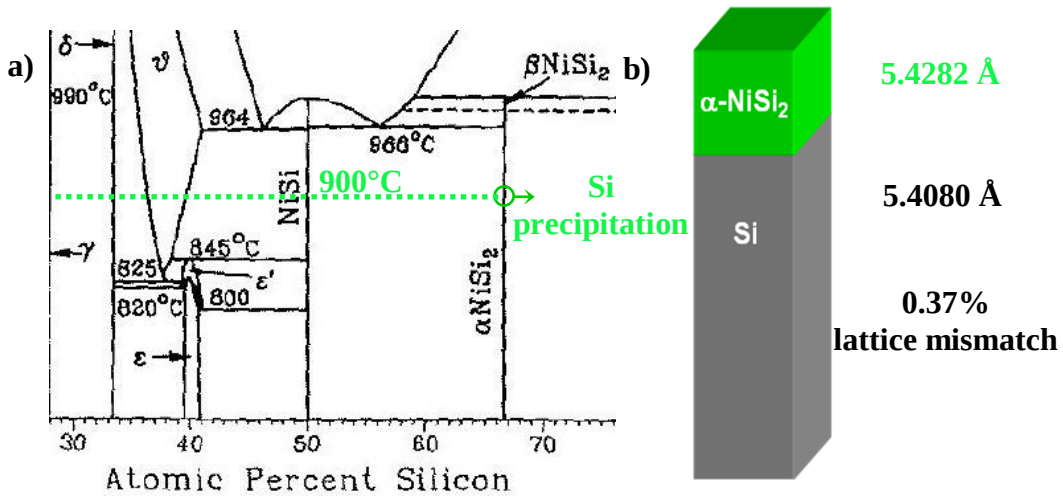

Figure 60: Schemata of the phase transitions during the $NiSi_2$ catalysed growth of Si-NWs with OCTS as precursor (a) and the lattice mismatch between NW and catalyst particle (b).

Although the explanation of the growth mechanism in Figure 60 is sound, it does not explain the presence of two different growth orientations with very similar diameters and not even the square habitus completely. In contrast Schmidt et al. [59] stated that

larger diameter Si-NWs most likely grow along the [111] directions. Silicon atoms precipitating upon the (111) surface during growth produce the largest decrease in Gibbs free energy, as these planes of Si have the largest density of surface atoms [107]. For thinner NWs, the free energy of the side faces must be taken into account and the [110] growth direction becomes more favorable. In this context Ciobanu et al.[108] have calculated that it is energetically possible to grow square shaped [110]-NWs, although they have to be extremely thin and H-passivated.

In this work the experiments were conducted at 900°C, below the lowest eutectic point of 966°C. The NWs were grown via a VSS-mechanism, where the usual thermodynamic preferences of a classical VLS growth do not apply anymore. Also the NWs' diameters (80 to 200 nm) are not small enough [11] to cause a drop in the melting temperature and push it to the liquid regime, which usually occurs at 10 nm and below. Therefore the usual thermodynamic preferences of a classical VLS growth do not apply anymore. It can be assumed that the catalyst particle is in the solid state during growth of Si-NWs, and that a solid-phase diffusion process, either in the bulk or on the surface, or both, must be responsible for NW formation. Nominally sub-eutectic NW synthesis using Au as catalyst has been achieved for several semiconductor materials, including Ge [109], InP [110], GaAs [111] and ZnSe [112]. For Si-NWs synthesis the results are conceptually similar to a previous report by Kamins et al. [113] of Ti-promoted Si-NW growth for temperatures below the Si-Ti eutectic point.

Theoretical calculations about a NW's habitus and growth direction were conducted by Zhang et al. [114], who revealed [100], [110], [111] and [112] as the most probable directions of H-terminated Si-NWs. Also different shapes of the cross section, hexagonal, square shaped, octagonal and triangular to name a few, are possible for Si-NWs of these orientations. The H-passivation in Zhang's work would explain the necessary high amount and flow rate of H_2, which was crucial to stabilize the square cross section. Another reason for the prismatic habitus lies in the cubic crystal system of the α–$NiSi_2$ particle, which seems to force its shape onto the NW. Such cubic particles were encountered even at the low temperature of 400°C (Figure 54a) without the addition of H_2.

Concerning the two different growth orientations, Tung et al. [115] observed the formation of $NiSi_2$-layers, by annealing thin Ni films on Si (111), with two different crystallographic orientations. The formation of these two directions, named A and B in Tung's work, depends on the initial thickness of the Ni film (Figure 61). With the

sputtering device used in this work nominally 2 nm of Ni were deposited, but experience showed that a closed layer cannot be expected at this thickness. Therefore it can be assumed that the two orientations Tung found, but did not identify, are [100] and [110], the orientations the α–$NiSi_2$ catalysed Si-NWs grow into.

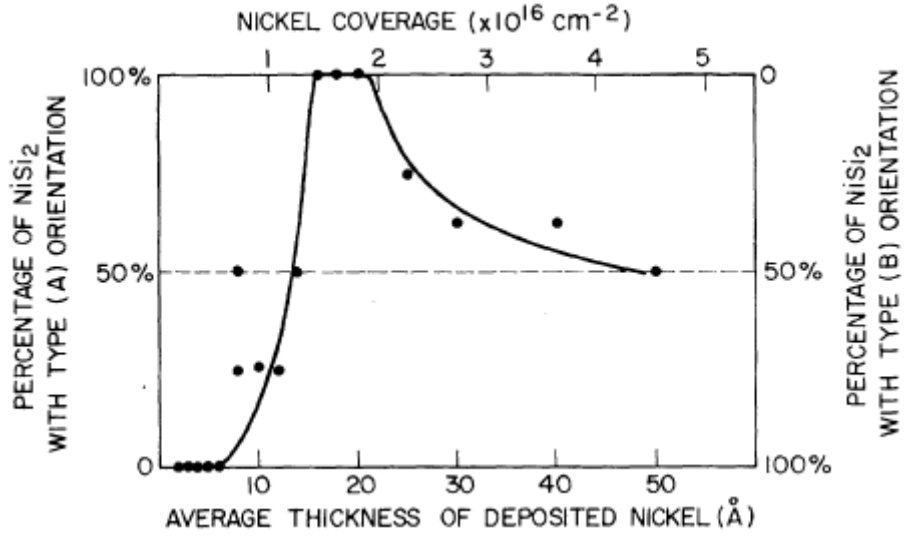

Figure 61: Crystallographic orientation dependency of the $NiSi_2$ layer by thickness of the deposited Ni layer [115].

4.3 Au, Cu, Ni and Pt catalysed Si-NW synthesis with BBr_3-doped OCTS

After successful experiments with pure OCTS, the next step was to add a doping agent to grow NWs with tuneable electrical properties. So about 100 ppm BBr_3 were added to pure OCTS and distilled within a very narrow temperature interval (~1°C).

4.3.1 In-situ B doped Au catalysed Si-NWs with OCTS as precursor

Although the addition of BBr_3 was in the ppm region, it soon turned out, that the growth behaviour was affected vigorously. Without the addition of H_2, proper NW growth with Au as catalyst was prevented at all investigated temperatures (400-900°C, Figure 62). All of these experiments were conducted with 80 nm Au colloids as catalyst.

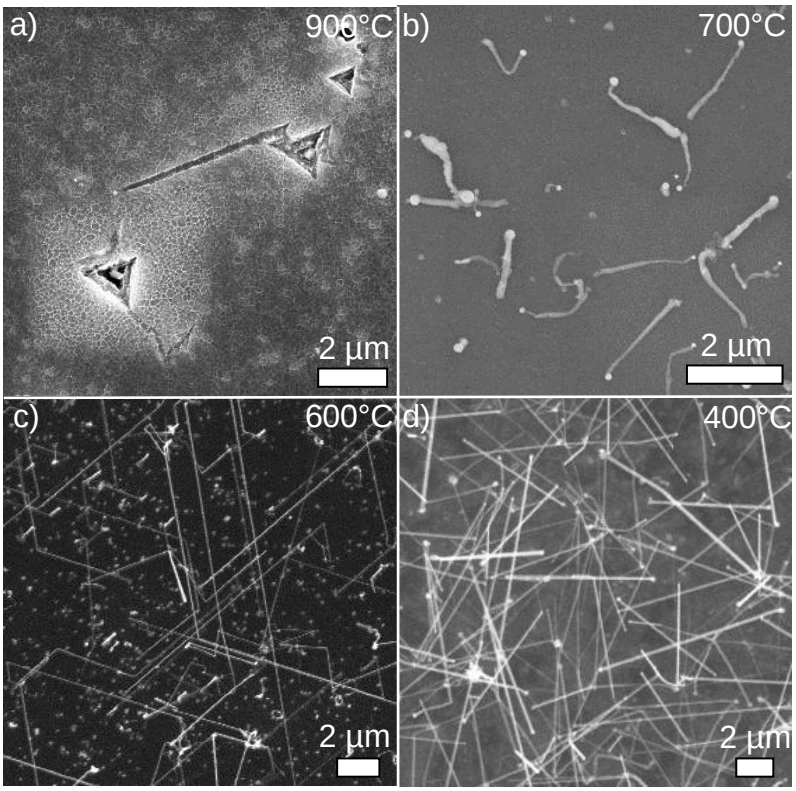

Figure 62: SEM images of OCTS grown Si-NWs catalysed by 80 nm Au colloids and nanostructures grown with BBr_3 doped OCTs at temperatures of:

a) 900°C; Only etching was encountered
b) 700°C; The sample was dominated by twisted and curved NWs
c) 600°C; Perfectly rod-like, epitaxial NWs were found
d) 400°C; Same rod-like NWs as at 600°C were encountered, although less epitaxial and more numerous.

At the highest temperature of 900°C, just triangular etching pits could be observed (Figure 62a). Although when using pure OCTS, the samples grown at this temperature yielded the most, epitaxial and defect free NWs, not a single NW was found under these conditions. Lowering the temperature to 700°C (Figure 62b) led to very twisted and curved NWs with 100 nm in diameter and more than 2 µm in length. Their habitus was strongly irregular in most cases, what also showed in the uneven diameter along the NWs. At 600°C (Figure 62c) the NWs were clearly epitaxial and very uniform in diameter (70 to 200 nm), while up to 20 µm long. Although there were still many unreacted colloids encountered on the substrate, the sample was well populated with NWs. Most surprisingly, at the lowest temperature of 400°C (Figure 62d) NWs were

still found in great numbers, actually more than at any other temperature. With 70 to 120 nm in diameter and up to 10 µm in length they were very similar to the NWs grown at 600°C, but their epitaxy was deteriorated.

Subsequent TEM investigations (Figure 63) of the epitaxial NWs grown at 600°C revealed a thick amorphous shell wrapping around the crystalline core, which covered about half of the NW's diameter. The roughness of the shell in Figure 63a may originate from a plasma clean, which was necessary before the actual TEM measurements. Longitudinal stripes, which represent stacking faults, run along the growth axis from bottom to top of the NW. Figure 63b shows a HRTEM from the crystalline core, giving a better look at the stacking faults, and the SAED clearly indicating a [112] growth direction.

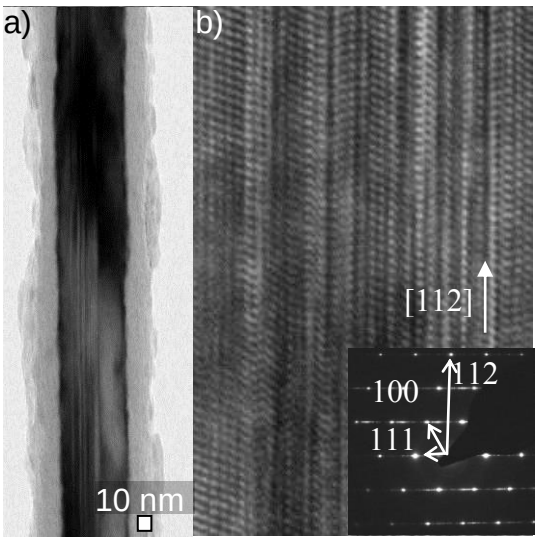

Figure 63: TEM images of a typical Au catalysed NWs grown with B-doped OCTS:

a) HRTEM; The amorphous shell and longitudinal stripes representing stacking faults are clearly visible
b) HRTEM revealing good crystallinity though stacking faults. The SAED in the inset confirms a growth direction of [112]

To summarize, even small amounts (~ppm) of doping agent can change the growth-behaviour considerably. Compared to the synthesis with pure OCTS, where effective Si-NWs growth was achieved in the temperature regime from 600°C to 900°C without any H_2, though with varying quality, the addition of BBr_3 limited NW growth to 400-600°C and made the addition of 20 sccm H_2 obligatory. Also the growth direction was changed from [111] with pure OCTS to [112]. Another remarkable feature was the thick

amorphous shell. Lauhon et al. [75] have shown a very similar amorphous shell of Si in their work wrapping around a p-doped core when adding B to the growth atmosphere. Briand et al.[116] mentioned the reduction of growth temperature by adding B as it promotes the decomposure of the precursor and therefore increases the growth rate, enabling lower growth temperatures. Although both of them used SiH_4, B seems to have the same effects on OCTS.

4.3.2 In-situ B doped Cu catalysed Si-NWs

Analogously to the experiments with pure OCTS, Au substitutes were investigated with B addition too. So a 2 nm thick Cu layer was sputter deposited on the cleaned samples and the same temperature interval and growth parameters were investigated as in previous growth experiments. The results of these experiments can be observed in Figure 64.

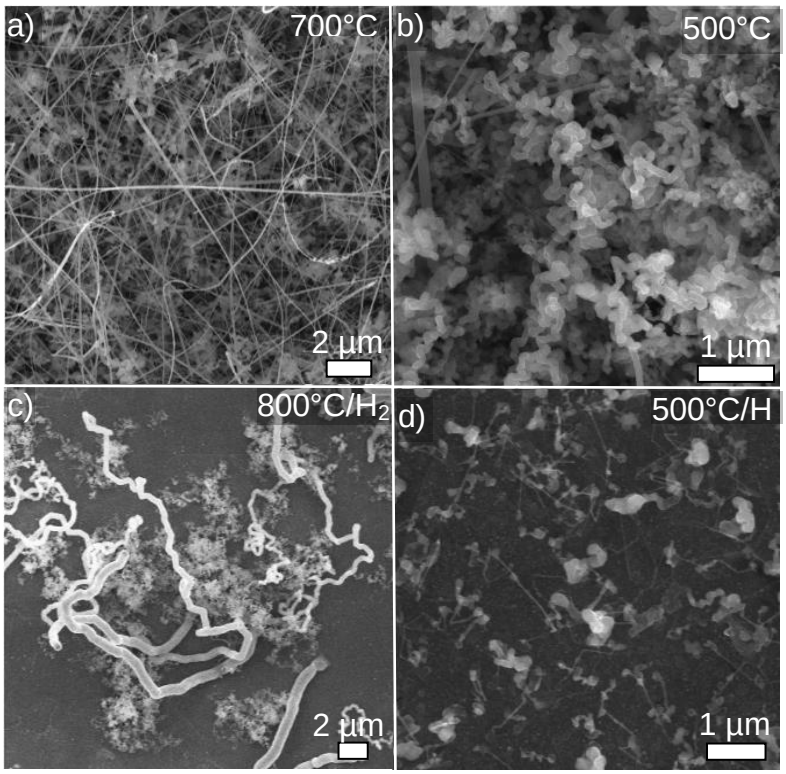

Figure 64: SEM images of growth experiments with Cu as catalyst and B-doped OCTS as precursor grown at temperatures of:

a) 700°C
b) 500°C
c) 800°C 20 sccm H_2 added
d) 500°C 20 sccm H_2 added

Although a decent number of NWs were yielded at 700°C (Figure 64a), they were strongly bent and twisted. The NWs' lengths were well beyond 20 µm and their diameters around 100 nm. Also uncatalytic deposits were found between the NWs in large quantities. Lowering the temperature to 500°C (Figure 64b) increases the share of

the uncatalytic deposits, which practically overgrew the NWs. At this temperature the NWs feature large diameters of up to 200 nm. The length is hard to determine as the uncatalytic deposits grow over the NWs, but can be assumed to be up to 5 µm and longer. The addition of 20 sccm H_2 reduced the amount of NWs and uncatalytic deposits as well. At 800°C (Figure 64c) the NWs were much thicker (up to 1 µm) than without H_2, but they were still strongly bent and twisted. Also uncatalytic deposits were found entangled with the NWs. At 500°C (Figure 64d) the NWs grew much thinner (~50 nm) and shorter (2 µm) than at 800°C, but they were still twisted and entangled with uncatalytic deposits. Epitaxial NWs were not encountered.

Compared to the experiments with pure OCTS, the addition of B had some serious effects on NW growth. Similar to the experiments with Au and B doped OCTS the growth temperatures were shifted to lower values. At 500°C the phase from which NWs nucleate is no longer the η phase, but the η‘ phase. Therefore strongly changed surface tensions and diffusion rates compared to the growth with pure OCTS can be assumed. Also the influence of the B itself must be taken into account. Practically the growth mechanism cannot be deduced from the binary phase diagram anymore, because a three phase system has to be considered now. It has been mentioned earlier that the addition of B causes an accelerated decomposition of OCTS during growth and is also responsible for a large amorphous shell when working with Au as catalyst. This may be an explanation for the low crystallinity and strong bending of the NWs as Cu seems to favor the formation of amorphous NWs even more than Au; especially at high temperatures.

4.3.3 In-situ B doped Pt catalysed Si-NWs

The experiments with Pt and pure OCTS yielded long, epitaxial NWs with a practically flawless crystal structure, so similar results with a B-doped NW were hopefully expected. The results can be seen in Figure 65.

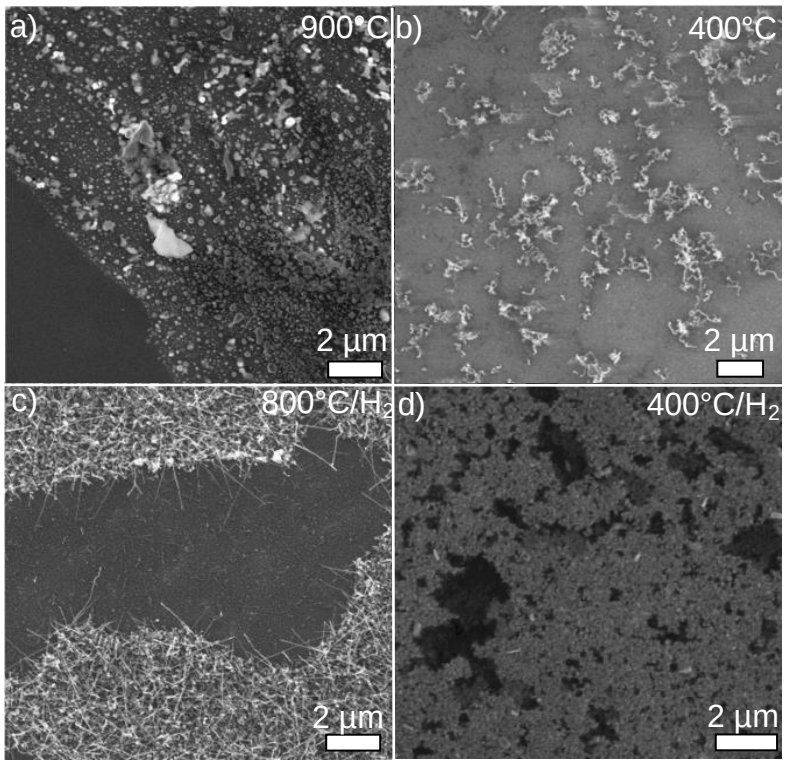

Figure 65: SEM images of samples grown with B-doped OCTS and catalyzed by a 2 nm Au film at temperatures of:

a) 900°C
b) 400°C
c) 800°C with 20 sccm H_2 added
d) 400°C With 20 sccm H_2 added

At the highest temperature of 900°C (Figure 65a), just uncatalytic deposits in various sizes and shapes were found on the samples. Lowering the temperature to 400°C (Figure 65b) resulted in densely populated samples with further uncatalytic deposits. In this case the deposits are strongly bent and some of them feature a high aspect ratio, although none of them resembles a proper NW. The addition of 20 sccm H_2 to the gas feed positively changed the growth behaviour. At 800°C (Figure 65c) NWs with ~50 nm in diameter and up to 3 µm long, which grew from islands with dense uncatalytic deposits, were encountered. Unfortunately these NWs did not feature epitaxy. At 400°C

(Figure 65d) only a mixture between etching and uncatalytic deposition was encountered.

Similar to the experiments with other catalysts and B-doped OCTS, the growth behaviour was also severely changed. At nearly all temperatures, irrespective of whether H_2 was added or not, only uncatalytic deposits, sometimes combined with etching, could be found. Only at 800°C with 20 sccm H_2 added, proper NWs could be produced, although even in this case epitaxy could not be achieved. Like the experiments with Cu and Ni before, this degrading change can be attributed to the alteration B introduces into the Pt/Si system by modifying surface tension and acceleration of the decomposition mechanism.

4.3.4 In-situ B doped Ni catalysed Si-NWs

After the impressive results from the experiments with Ni catalyst and in conjunction with pure OCTS earlier it was also attempted to generate square shaped, B-doped NWs and subsequently NWs with tuneable electrical properties. The results of these experiments are shown in Figure 66. Also in this case the 30 minute annealing step previous to growth was skipped as the diffusion rate of Ni in Si was considered to too high to form the desired α-$NiSi_2$.

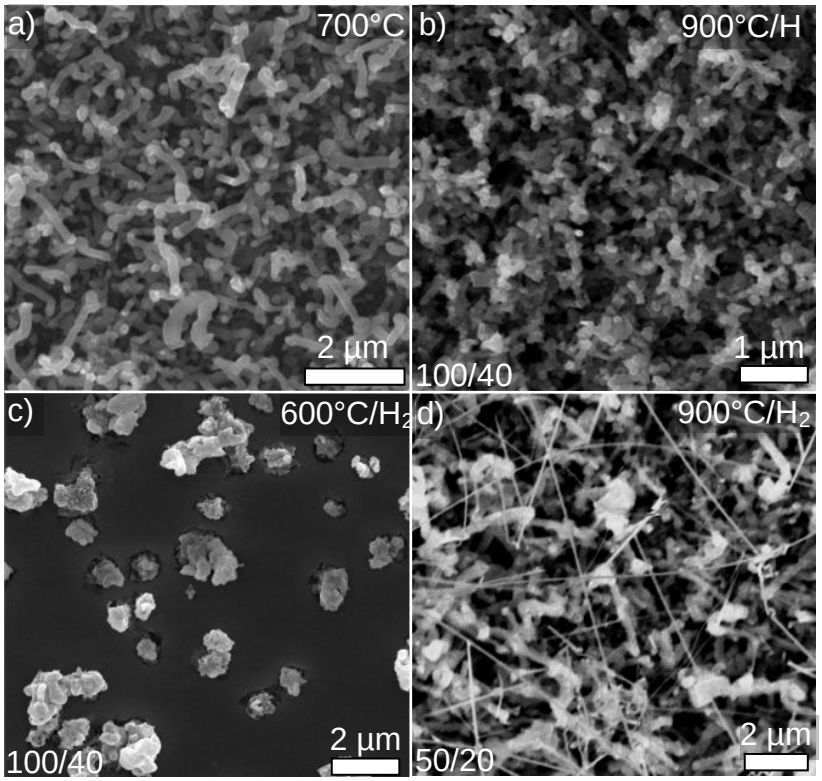

Figure 66: SEM images of growth experiments with Ni as catalyst at temperature of using Boron doped OCTS as precursor:

a) 700°C
b) 900°C with He/H_2:100/40
c) 600°C with He/H_2:100/40
d) 900°C with He/H_2:50/20

Figure 66a shows the results of Ni catalysed growth at 700°C without the addition of H_2. Only intertwined nanostructures were produced without H_2 and no NWs were encountered at any temperature. Nonetheless the nanostructures covered the whole sample and were about 200 nm thick, while measuring up to 2 µm in length. At 900°C

(Figure 66b) the nanostructures grew more dense compared to Figure 66a, but were less edged. Surprisingly some NWs were encountered on this sample with 100 nm in diameter, although they were almost completely concealed by other nanostructures. At the lower temperature of 600°C (Figure 66c) just clumps with diameters up to 1.5 µm were discovered and signs of etching were observed next to them. Changing the flow rate to He/H_2:50/20 (Figure 66d) resulted in mainly edged nanostructures covering the sample, but also a fair number of very thin (~50 nm) and long (10 µm and longer) NWs were generated. Unfortunately these NWs were not square shaped and in nearly all cases strongly bent.

The reasons for the failure to produce square shaped NWs, like it was done before with pure OCTS, can be attributed to the presence of B during growth. From earlier discussions it is known that B changes surface energies and accelerates the decomposition of OCTS, which has a tremendous effect on the NW growth with Cu as catalyst. Actually it can no longer be considered a binary phase diagram, but a ternary one. A change in surface energy, perhaps the most determining factor of NW growth, can be assumed due to the presence of B. Another important aspect is that no bright α-$NiSi_2$ tips were observed. So it can be assumed that the presence of B changess the phase diagram to a degree where α-$NiSi_2$, which proved so immensely important for epitaxial, square shaped NW growth with pure OCTS, is no longer the nucleating phase for NW growth. Concluding it can be said that the addition of B suppressed the formation of square shaped or even epitaxial NWs with Ni as catalyst and favors the deposition of irregular uncatalytic nanostructures.

4.4 Au, Pt and Ni catalysed NW synthesis with PCl_3-doped OCTS

Based on the results, which were obtained with B as catalyst, only the three most promising catalysts were investigated with P-doped (PCl_3) OCTS. Au was chosen because of its small sensitivity to process parameters and good reproducibility, Ni for the promising square shaped NWs with α-$NiSi_2$ tip and Pt because of the practically flawless crystal structure and straight habitus which were obtained using pure OCTS.

4.4.1 In-situ P doped Au catalysed Si-NWs

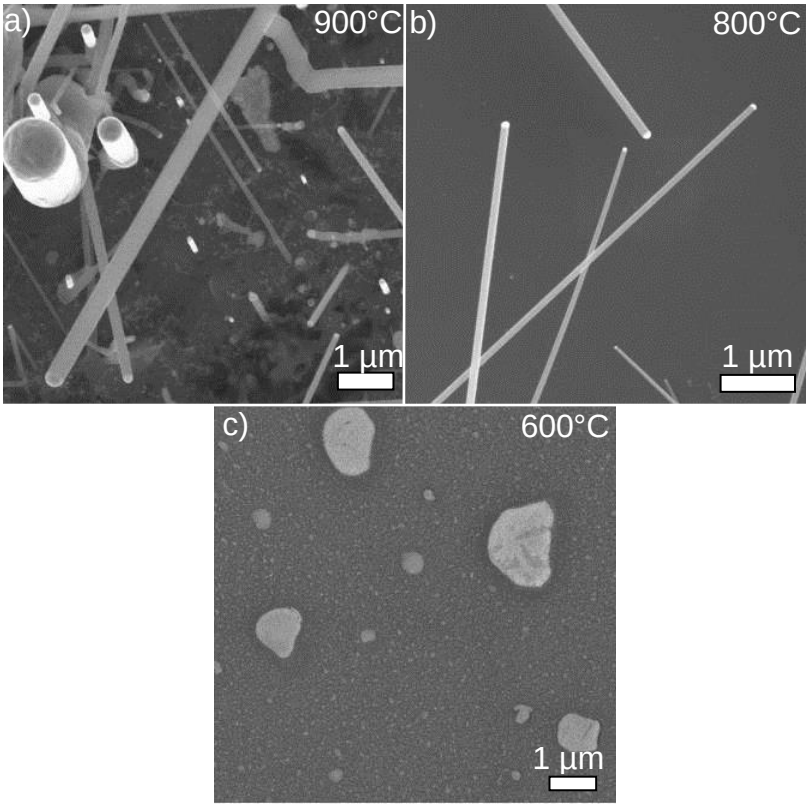

Figure 67: SEM images of samples grown with P-doped OCTS and 9 nm Au as catalyst at temperatures of:

a) 900°C, epitaxial NWs
b) 800°C
c) 600°C

At 900°C (Figure 67a) epitaxial NWs with a very wide range of diameter, 50 to 1000 nm, were yielded. Their sometimes huge diameter originated from the big amount of Au (9 nm layer), that had to be used to enable growth, otherwise samples were received,

where etching was the dominant process. Nonetheless etching is also visible at 900°C when the Au layer was used. Lowering the temperature to 800°C (Figure 67b) resulted in much thinner NWs, around 50 nm. Also the etching of the substrate was strongly reduced. At the lowest temperature of 600°C (Figure 67c) only clumps of Au-Si-alloys could be found. Subsequent to these experiments, 20 sccm of H_2 were added to the feed gas to improve growth behaviour. The results can be seen in Figure 68

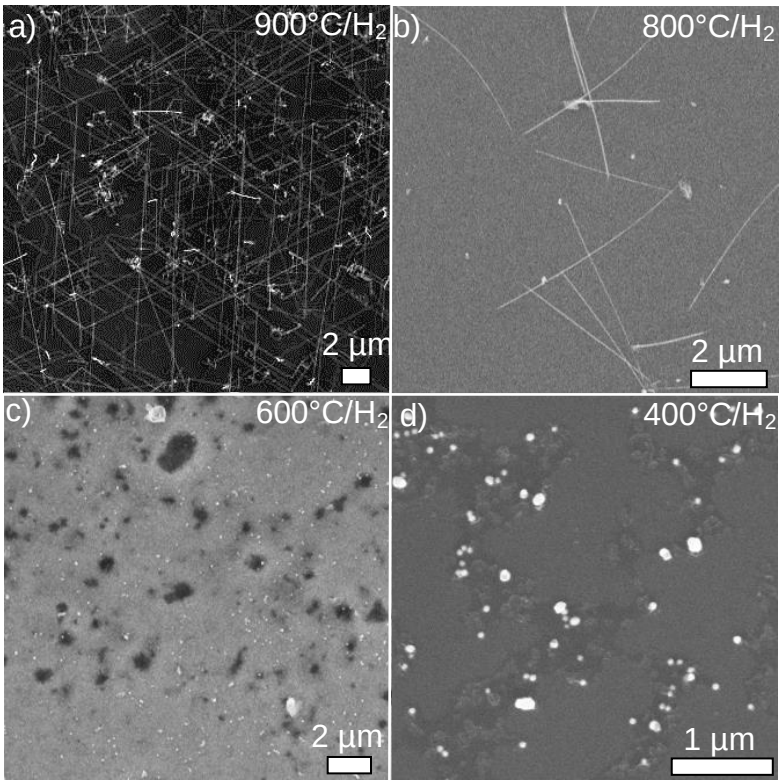

Figure 68: SEM images of samples grown with P-doped OCTS and 9 nm Au film at temperatures of:

a) 900°C
b) 800°C
c) 600°C
d) 400°C

In these cases 20 sccm H_2 were added to the gas feed, what favored etching strongly and eliminated NW growth at all temperatures below 800°C.

By the addition of 20 sccm H_2, etching was strongly reduced at 900°C (Figure 68a). The NWs became epitaxial with about 60 nm to 150 nm in diameter and up to 30 µm long. At 800°C (Figure 68b) NWs were encountered in small numbers with lengths of up to 3 µm and diameters of 50 nm. These NWs were also bent in most cases.

Downwards at 600°C and 400°C (Figure 68c and d), no NWs were encountered, although etching could be observed at 600°C. Figure 69 shows TEM images, which were obtained from Au catalysed, P-doped NWs grown at 900°C with 20 sccm H_2 added.

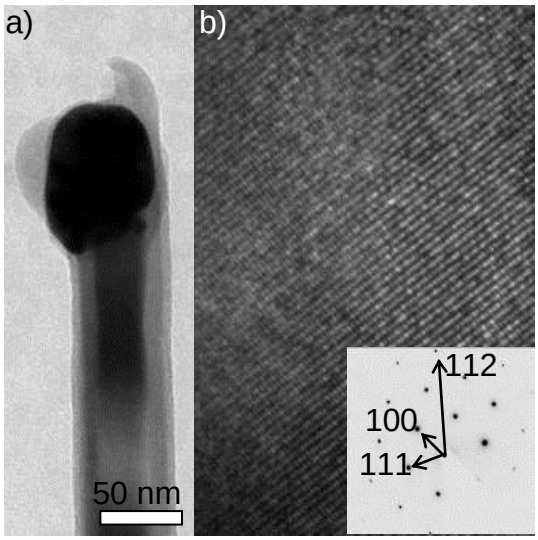

Figure 69: TEM images of a NW grown with PCl_3 doped OCTS and Au as catalyst:

a) HRTEM image showing thickness contours across the NW's body and the catalyst particle
b) HRTEM revealing the NW's crystal structure. The inset indictes a [112] growth direction

Figure 69a demonstrates a typical NW grown at 900°C with a diameter of 60 nm. Strong thickness contours can be observed as well as a Si shell around the catalytic Au particle, which formed during the cooling process. The image in Figure 69b shows that also PCl_3 affects NW growth by changing the growth direction. Such epitaxial NWs grow preferentially along the [112] direction like their B-doped counterparts. The NWs themselves are rodlike, of good crystallinity and feature no observable defects or stacking faults.

It can be said, that also PCl_3 affects the NW growth severely, when using Au as catalyst. The optimal growth conditions shifted to higher temperatures (≥800°C). 80 nm Au particles which were very convenient in handling and successful in matter of growth with pure and B doped OCTS unsuitable when P was involved. A 9 nm Au layer was necessary to yield a decent amount of NWs, thus leading to a much bigger diameter and

size distribution. In this context Schmid et al. [29] investigated the effect of different concentrations of P dopant on NW growth. The results revealed that PH_3 reduces NW growth and even suppresses it at high partial pressures by blocking the absorption spots on the catalyst particles. The same seems to happen in this case. Growth was only observed with a 9 nm layer of Au, while test with 80 nm colloids were also conducted, but were unsuccessful due to the absorption space blocking of P. The 9 nm Au layer simply offers a much bigger amount of Au than the 80 nm colloids, so that still enough absorption spots remain free for the precursor. The higher temperatures and therefore higher reaction rates were necessary to compensate for the decrease in absorption area. The etching at the highest temperatures can be explained by the decomposition of $SiCl_4$ into Si and HCl. In retrospective there must be a temperature between 800°C and 900°C, where $SiCl_4$ breaks up and delivers additional Si, but also additional etching species. The 20 sccm of H_2, which were added in later experiments confirm this, as etching intensifies further, especially at the highest temperature of 900°C. This also explains the absence of any NWs at temperatures lower than 800°C, as the reaction rates cannot compensate for the reduced absorption area and only clumps were encountered. The effects on morphology are not as profound as the addition of BBr_3 causes, but the growth orientation changes into [112] analogously. Compared to the B addition no stacking faults or other defects could be observed.

4.4.2 In-situ P doped Pt catalysed Si-NWs

Considering the successful growth of highly crystalline Si-NWs with pure and B-doped OCTS, using Pt as catalyst, it was expected to generate similar results with P-doping. The results of these experiments can be seen in Figure 70.

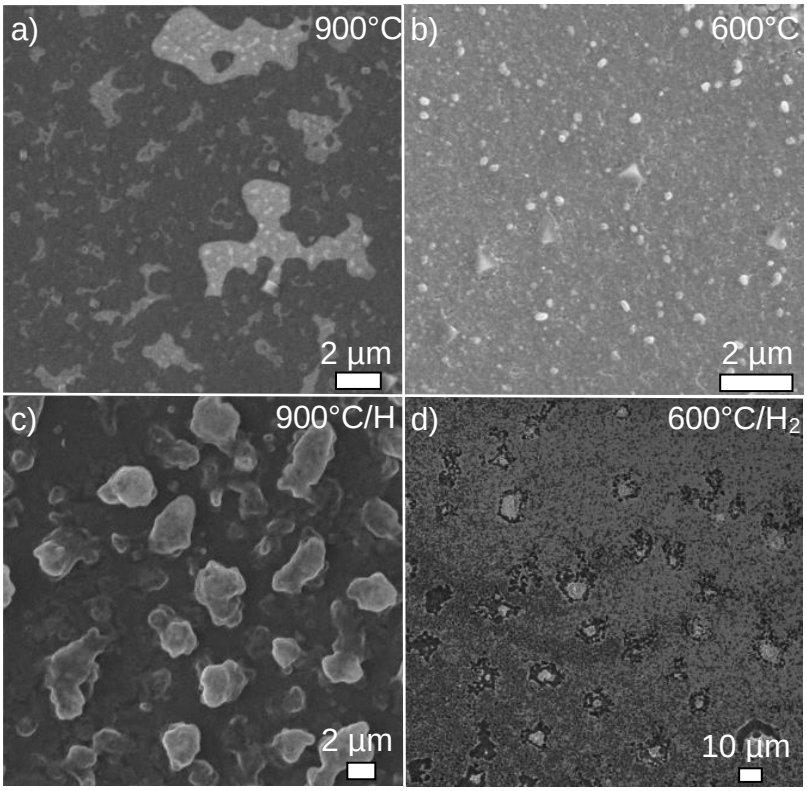

Figure 70: SEM images of samples grown with P-doped OCTS and Pt as catalyst at temperatures of:

a) 900°C
b) 600°C
c) 900°C with 20 sccm H_2
d) 600°C with 20 sccm H_2

The addition of PCl_3 suppressed formation of NWs at all examined temperatures independently of the presence of H_2.

Despite the earlier promising results, the addition of PCl_3 prevented NW growth at any investigated temperature independently of the presence of H_2. At high temperatures (900°C, Figure 70a) the initial Pt layer was clearly melted and formed either a flat, incomplete layer on the surface or big clumps with 20 sccm H_2 added (Figure 70c). At

the lower temperature of 600°C (Figure 70d), etching could be observed in the vicinity of the Pt particles when H_2 was present. Without H_2 (Figure 70c) no etching was detected. When comparing these results with the Au/PCl_3 combination it seems that P affected the Pt catalyst more. In this case the adsorption points on the surface were not just reduced, like with Au, but practically completely covered by P during the growth process and therefore eliminating NW growth.

4.4.3 In-situ P doped Ni catalysed Si-NWs

Ni was also tested with PCl_3 doped OCTS to generate doped NWs at temperatures between 400°C and 900°C without H_2 (Figure 71) and with 20 sccm H_2 added (Figure 72). In both cases the 30 minute annealing step was skipped due to the high diffusion rate of Ni in Si.

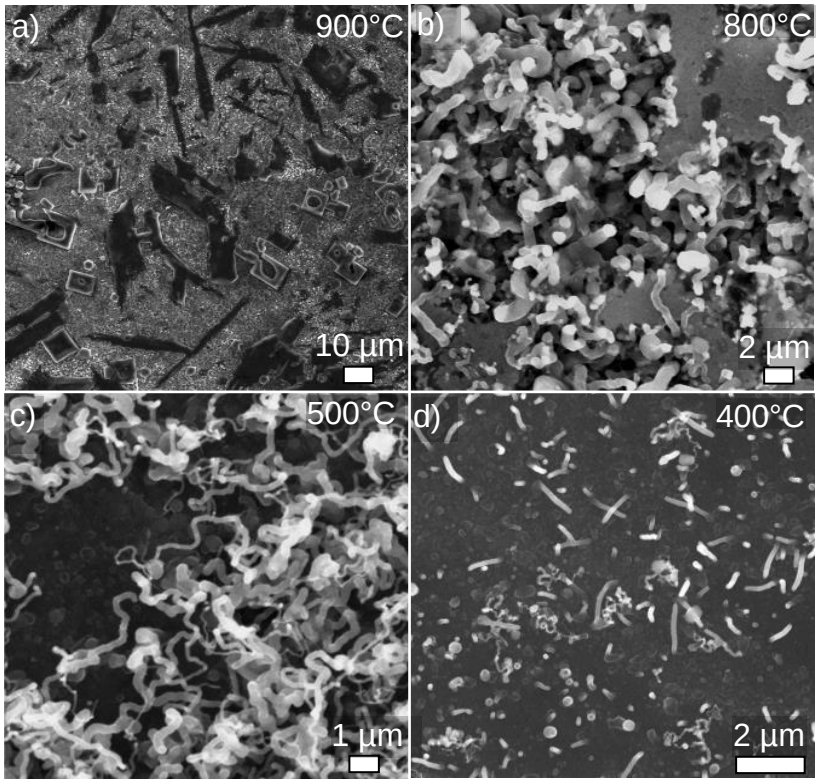

Figure 71: SEM images of samples grown with Ni as catalyst and OCTS/PCl_3 as precursor at temperatures of:

a) 900°C
b) 800°C
c) 500°C
d) 400°C

Although rectangular structures could be observed at the highest growth temperature of 900°C (Figure 71a), no NWs growing from them were encountered. At the lower growth temperature of 800°C (Figure 71b), nanostructures were found in plenty numbers growing in pits. The nanostructures were growing exclusively in these pits, but not on the remaining pieces of intact surface. Cuscuná [117] has reported growth of Si-

NWs by chemical and/or physical roughened surfaced, which would explain the preference of the etching pits as origin of growth. The nanostructures themselves are up to 3 µm long, around 500 nm thick and strongly irregularly shaped. At 500°C (Figure 71c) the nanostructures get longer and become more twisted, although their diameter remains around 500 nm and they still prefer to grow from roughened surfaces. Finally at 400°C (Figure 71d) NWs were encountered in considerable numbers with up to 2 µm in length, 100 nm in diameter and a much less twisted shape than at higher temperatures. Unfortunately no signs of epitaxial growth were found.

As it proved to be very beneficial for NW growth in earlier experiments 20 sccm of H_2 were added to the gas feed. The results of these experiments can be seen in Figure 72.

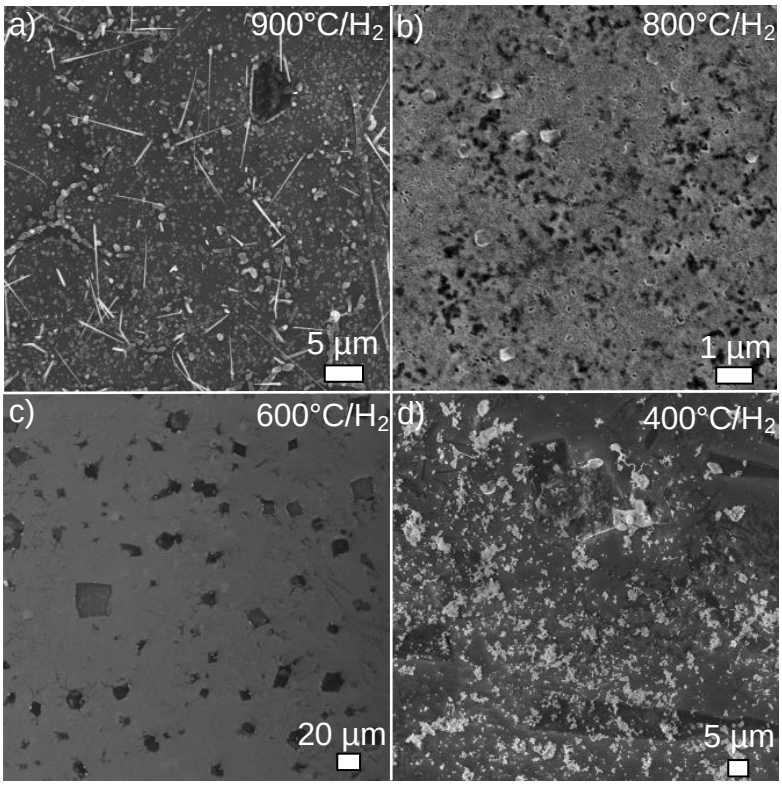

Figure 72: SEM images of samples grown with Ni as catalyst and OCTS/PCl_3 as precursor at temperatures of:

a) 900°C
b) 800°C
c) 500°C
d) 400°C

During all of these growth experiments 20 sccm of H_2 was added to the gas feed

NWs were successfully grown at 900°C (Figure 72a). These NWs were up to 5 µm long, about 100 nm thick and strongly tapered. This might originate from uncatalytic deposition on the sidewalls and is also supported by the work of Krylyuk et al. [118]. They demonstrated the influence of partial pressure of the precursor on a NW's tapering behaviour involving $SiCl_4$ and H_2. It was also mentioned earlier, that Si from $SiCl_4$, a byproduct of OCTS decomposition, becomes available at temperatures of 900°C and higher, which would further support the assumption of sidewall-deposition. The NWs produced this way did not feature epitaxy. At lower temperatures only different intensities of etching could be observed. At 800°C (Figure 72b) and 600°C (Figure 72c) etching was clearly visible over the whole sample. In the latter ones also rectangular structures could be observed, originating from cubic nickelsilicide crystals. At the lowest temperature of 400°C (Figure 72d) only uncatalytic deposits covered the sample.

4.5 Electrical properties of VLS-grown Si-NWs

4.5.1 Resistance and contact resistance of Si-NWs grown with pure OCTS

As described in chapter 3.3, modules with integrated NWs were prepared by electron beam lithography and lift off techniques. With these modules it was possible to investigate the electrical properties of NWs synthesised in this work. Figure 74, Figure 76 and Figure 78 show I/V curves of NWs grown with pure OCTS for different catalysts.

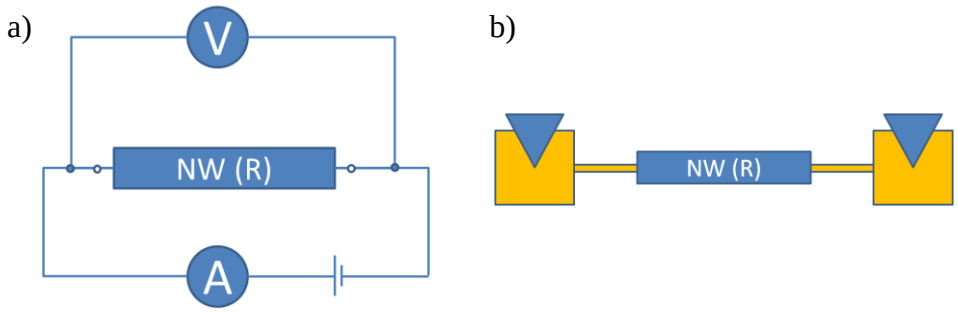

Figure 73: Schematic (a) and setup (b) of a 2-point electric measurement utilised for characterisation of NWs

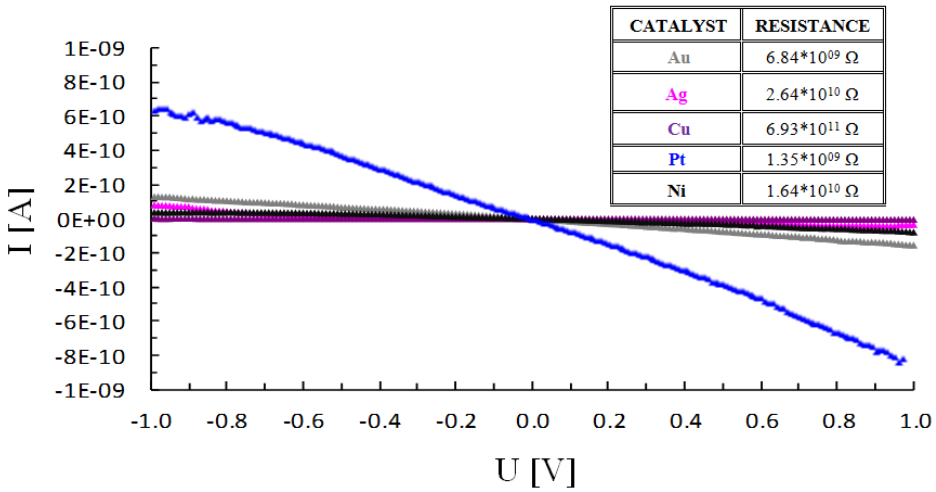

Figure 74: I/U curves of 2-point measurements of differently catalysed NWs. The inset shows thereof calculated resistance (including contact resistance) of the respective NWs.

Measured between -1 V and +1 V, Pt catalysed NWs with OCTS as precursor show by far the smallest resistivity ($1.35*10^9$ Ω), while Au catalysed NWs also show a low

resistivity with $6.84*10^{9}$ Ω. Ag, Ni and Cu catalysed NWs feature a comparable high resistivity, what can be attributed to strong incorporation of catalyst material during growth and formation of severe defects as determined by TEM investigation. Of course the values shown in Figure 74 are composed of the actual resistivity of the measured NW and the contact resistance of the interfaces of the contacts. To determine the resistivity of the NWs and the contact resistance, 4-point measurements were also conducted on the very same NWs (results in Figure 76 and Table 2).

Table 2: Contact resistivity and actual NW resistivity of differentially catalysed NWs grown with OCTS as precursor

Catalyst	Contact resistance	NW's resistance per unit length
Au	$6.55*10^{08}$ Ω	$3.48*10^{02}$ Ω/cm
Ag	$2.52*10^{10}$ Ω	$1.41*10^{05}$ Ω/cm
Cu	$6.49*10^{11}$ Ω	$4.17*10^{02}$ Ω/cm
Pt	$1.28*10^{09}$ Ω	$9.21*10^{03}$ Ω/cm
Ni	$8.49*10^{09}$ Ω	$8.64*10^{03}$ Ω/cm

Au ($6.55*10^{8}$ Ω) and Pt ($1.28*10^{09}$ Ω) catalysed NWs feature the lowest contact resistivity. Au is unable to form silicides, which could increase the contact resistance. Pt can form silicides, what explains the higher contact resistance compared to Au catalysed NWs. Pt catalysed NWs feature a flawless crystal structure, what still results in a comparably low contact resistance. Contrary, Ni can form several silicides, what explains the higher contact resistance ($8.49*10^{09}$ Ω). Ag catalysed NWs feature a high contact resistivity ($2.52*10^{10}$ Ω) due to the tendency of twinning, what deteriorates crystallinity. Cu catalysed NWs exhibit a very high contact resistance ($6.49*10^{11}$ Ω), what is in agreement with the work of Wu et al.[119]. Wu observed a very high resistance at interfaces during annealing due to the formation of Cu_3Si, the phase the NW actually precipitates from.

4.5.2 Specific resistivity and mobility of Si-NWs grown with pure OCTS

The I/V curves were measured at gate voltages between -5 V and +5 V and showed very different specific resistivities. Cu ($7.8*10^4$ Ωcm) and also Ni ($1.57*10^4$ Ωcm) feature a very high specific resistivity, what can be attributed to deep level traps and incorporation of the catalyst in the NW during growth, upon which mixed crystals are formed. The presence of high resistivity Cu_3Si, which was incorporated from the catalyst particle during growth, further underlines the high values Cu catalysed NWs experience in these tests. The investigations of Au catalysed NWs revealed a specific resistivity of $5.96*10^3$ Ωcm, which is comparable with the results of Heath et al. [33]. They reported a specific resistivity of intrinsic NWs, grown with SiH_4 as precursor, of about 1 kΩcm. These NWs are just slightly tapered and feature a next to flawless crystal structure (Figure 44a), which indicates low catalyst incorporation during growth. Nonetheless deep level traps also play in important role when catalysing with Au as it is one of the most potent deep level trap benefactors in Si [3]. Given the fact that Au is definitely a stronger deep level trap benefactor than Cu or Ni, it can be said that the influence of crystal structure and mixed crystal formation outranks the influence of deep level traps within this experiments. Ag experienced, contrary to the other catalysts, a strong non ohmic behaviour. This is most likely a result of the twin crystals that were encountered during TEM investigation, but can also be attributed to contacting problems. The specific resistivity of these NWs ($4.23*10^3$ Ωcm) is also a little lower than their Au catalysed counterparts. Finally Pt catalysed Si NWs feature by far the lowest specific resistivity ($9.72*10^2$ Ωcm). The reason for this is the practically flawless crystal structure and Pt's advantageous deep level trap behaviour.

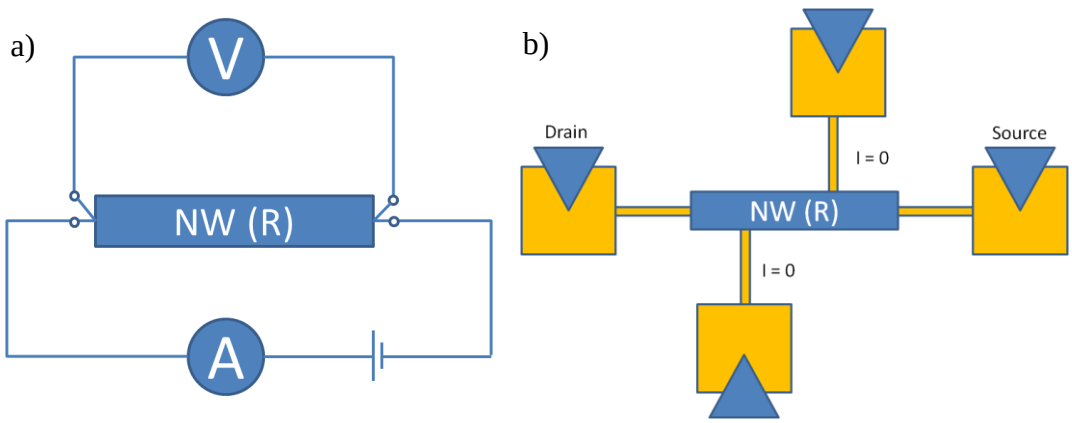

Figure 75: Schematic (a) and setup (b) of a 4-point electric measurement utilised for characterisation of NWs

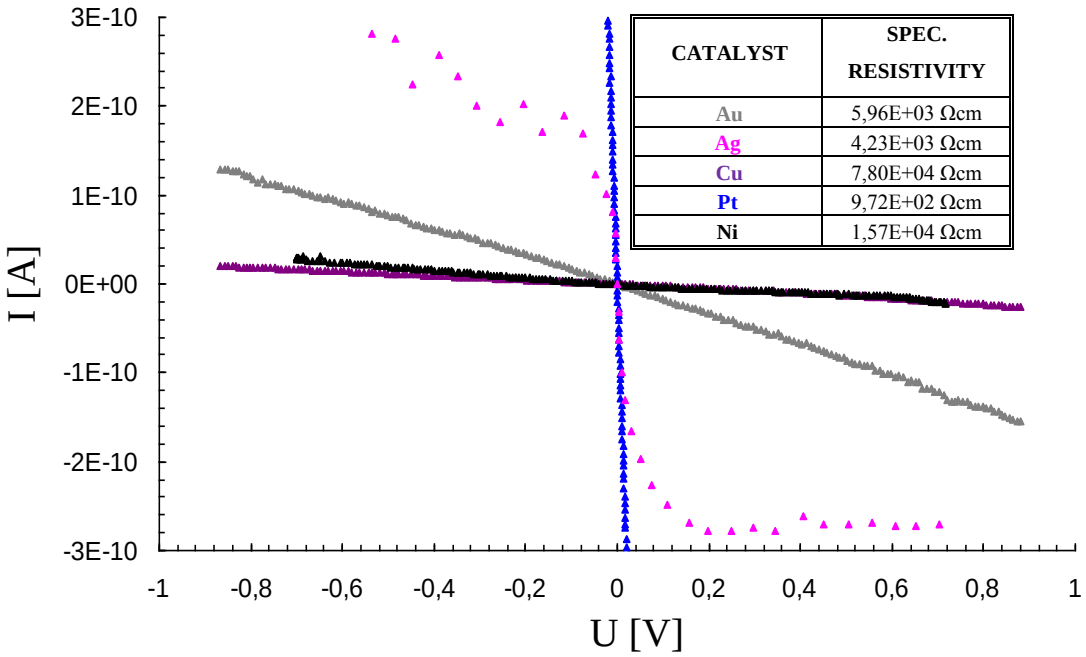

Figure 76: I/U curves of NWs catalysed with Pt, Ag, Au, Ni and Cu grown with pure OCTS. The x-axis shows the voltage difference between the inner two contacts of the 4-point measurement. The specific resistivity of these NWs is noted in the inset.

4.5.3 Specific resistivity and mobility of Si-NWs grown with pure OCTS

Following the I/V measurements, the back gated measurements again revealed very different behaviour for Pt, Ag, Au, Ni and Cu catalysed Si NWs (Figure 78, Table 3). The schematic and setup for these measurements are shown in Figure 77. Although all NWs experienced intrinsic p-type behaviour, their threshold voltages and trans-conductance varied strongly.

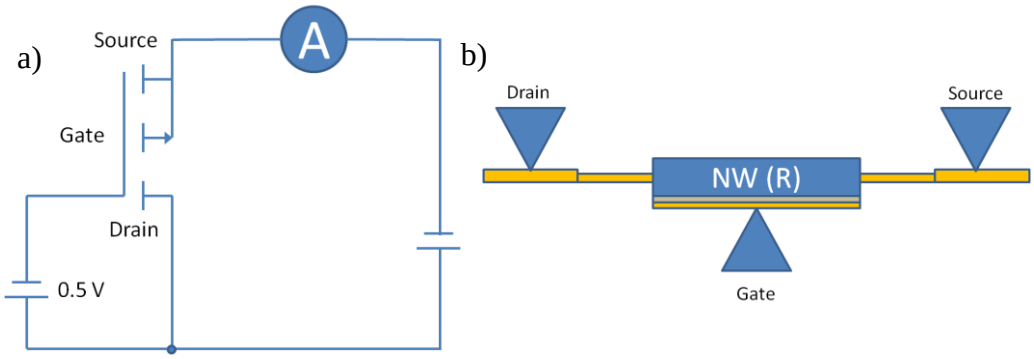

Figure 77: Schematic (a) and setup (b) of a FET measurement utilised for characterisation of NWs

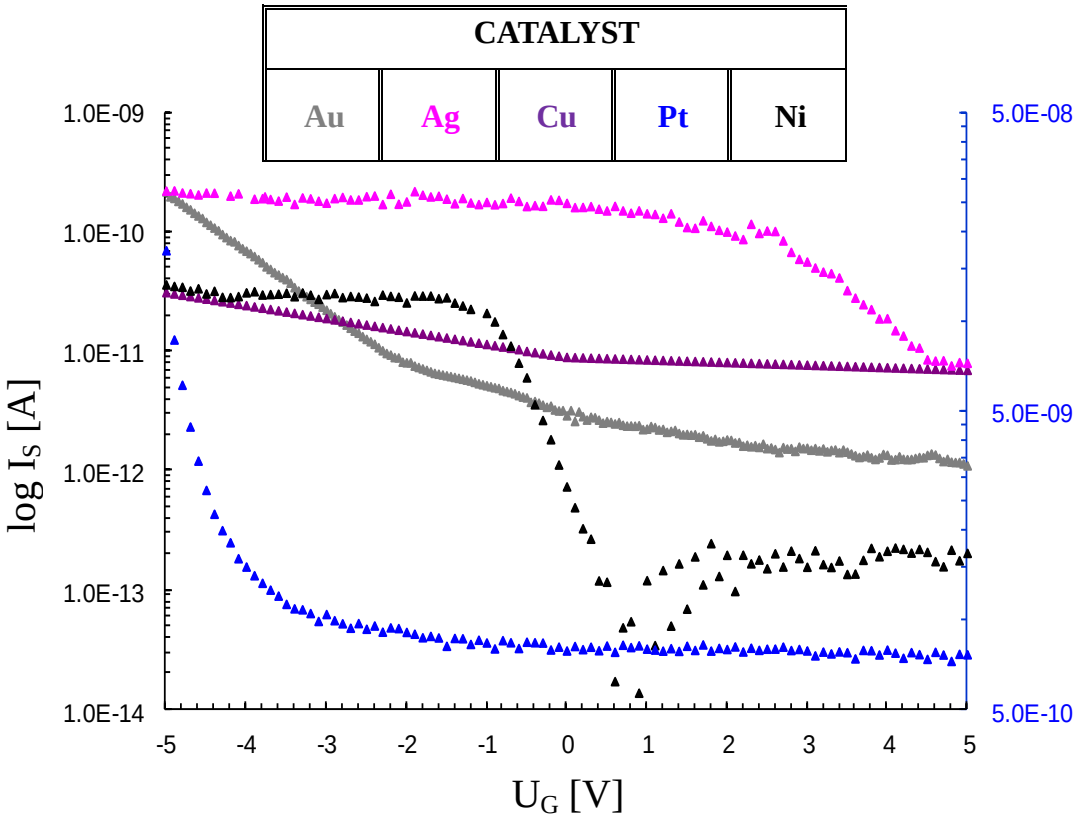

Figure 78: Back gated measurements of the differently catalysed NWs grown with pure OCTS. The current of the Pt catalysed NWs is correlated with the secondary y-axis as it outperforms any other NW by at least two orders of magnitude. All NWs show a more or less pronounced p-type behaviour and very differing thresholds.

Table 3: Characteristic values of catalysed FET- NWs along with their respective mobility

Catalyst	I_{on} [A]	I_{off} [A]	U_{on} [V]	U_{off} [V]	μ [cm²/V*s]	Threshold [V]
Au	$2.20*10^{-10}$	$7.51*10^{-12}$	-5.0	-2.0	0.106	-4.5
Ag	$1.94*10^{-10}$	$8.58*10^{-12}$	-1.3	4.5	0.024	+4.4
Cu	$3.32*10^{-11}$	$7.55*10^{-12}$	-5.0	-0.5	0.015	+2.0
Pt	$1.73*10^{-08}$	$8.70*10^{-10}$	-5.0	-1.6	3.441	-4.5
Ni	$2.84*10^{-11}$	$2.66*10^{-12}$	-1.5	-0.3	0.030	-0.4

Although the thresholds of Cu and Ni were different with +2 V and -0.4 V respectively, the resistance drop was very low with both catalysts. Au and Pt feature a comparably large drop in resistance (about one order of magnitude) with the same threshold of -4.5 V. Finally Ag catalysed Si NWs changed their resistance at a threshold of +4.4 V, what may be due to twin crystal formation. The resistance drop of these NWs ranges between that of Ni and Au.

From the investigated NWs only Ag and Ni catalysed Si-NWs show a promising behaviour for use as NW-FETs as they offer a reasonable increase in current within a rather small voltage interval.

Similar p-type behaviour is observed for most intrinsic VLS grown Si-NWs and can be attributed to surface hole accumulation due to trapped negative surface charge, although contribution of impurities like Au and O cannot be excluded completely [120].

To calculate the channel mobility (μ) a model used by Khanal et al. [121] was used, with the vacuum permittivity (ε_0=8.854*10^{-12} C/Vm), the relative permittivity ($\varepsilon_r(SiO_2)$=3.9), the length of the respective NW (L), the height of the respective NW (h) and the drain voltage (U_D=0.5V).

$$g_m = \frac{\partial I_D}{\partial U_G} \approx \frac{\mu 2\pi\varepsilon_0\varepsilon_r}{L * \ln\left(\frac{2h}{r}\right)} * U_D$$

The transconductance (g_m) along with the voltage difference U_D for the respective NWs were derived from Figure 78. The calculated values for the NWs' channel mobility shown in Table 3 agree quite well with the value of 0.1 cm²/V*s Byon et al. have received for their Si-NW FETs [122]. Only the Pt catalysed NWs show a

comparable large mobility. This high value may be attributed to the formation of platinum silicides, which feature a very high I_{ON}/I_{OFF} ratio; also described by Jang et al. [123] with greater than 10^6. This is still far less than the hole mobility of bulk Si (450 $cm^2/V*s$).

4.5.4 Electrical characterisation of Si-NWs grown with doped OCTS

As mentioned earlier only Au as catalyst could provide epitaxial NWs with pure OCTS and the B and P doped mixtures. So only these NWs were measured and showed very different specific resistivities due to the different precursor mixtures used (Figure 79).

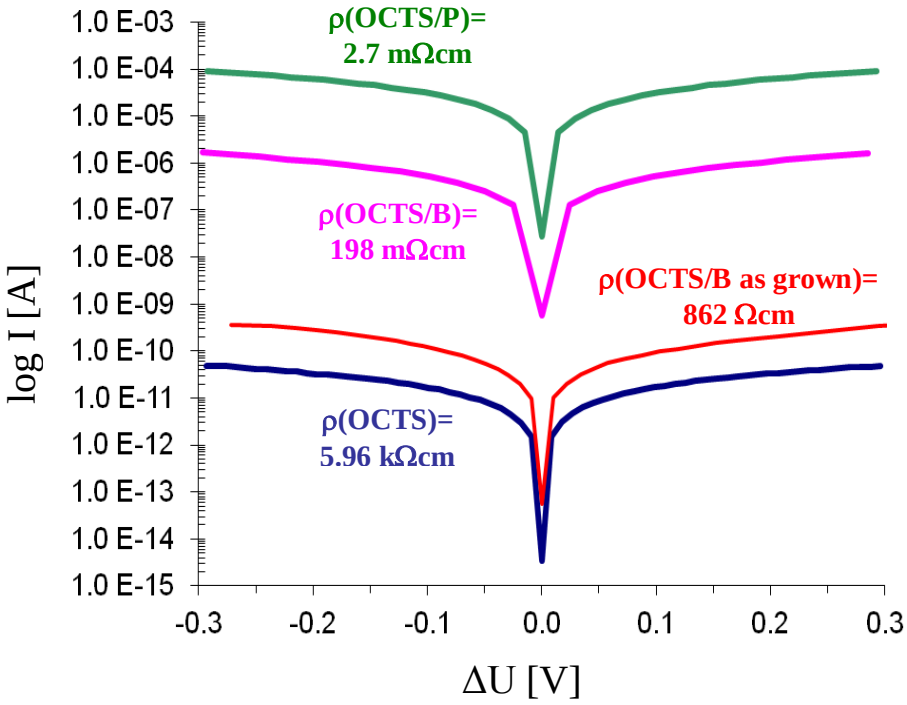

Figure 79: Semi-logarithmic I/V-plot of intrinsic, p- and n-type NWs. Thereof calculated specific resistivity values are shown next to the respective curves. Values of the annealed and unannealed B doped NWs are shown to view the impact of contacting problems and the amorphous shell on the NWs resistivity.

As expected, NWs grown with pure OCTS exhibited the highest specific resistivity ($5.96*10^3$ Ωcm). B doped NWs feature a rather high specific resistivity with $8.62*10^2$ Ωcm, what is due to the large amorphous shell and stacking faults (Figure 63a), which were caused by the addition of BBr_3 during growth. Annealing at 470°C for 2 min

reduced the specific resistivity considerably to $1.98*10^{-1}$ Ωcm, or by a factor of ~4350. According to Lauhon et al. [75] the annealing causes the amorphous shell to crystallize and improves conductibility. P finally shows the best doping activation of all three mixtures, which results in a specific resistivity of $2.4*10^{-3}$ Ωcm. Comparing these values with active dopant concentrations in bulk Si, leads to $2*10^{12}$ cm^{-3}, 10^{17} cm^{-3} and $3*10^{19}$ cm^{-3} for intrinsic, B-doped and P-doped NWs, respectively [54]. Unfortunately the high conductibility of the doped NWs completely prevented channel modulation when they were integrated into back-gated FETs.

The contact resistance was calculated analogously to the intrinsic NWs described before. Unannealed B-doped NWs feature a high contact resistance of $2.96*10^{9}$ Ω. Once annealed, the contact resistance dropped to $9.28*10^{4}$ Ω, what can be attributed to the amorphous Si shell deteriorating the contact interface. P-doped NWs feature a smaller contact resistance of $9.18*10^{3}$ Ω, what probably originates from the already low specific resistance.

4.5.5 Characterisation of an in-situ grown pn-diode

The good activation and incorporation of dopants during growth, led to the idea of an in-situ grown diode processed according to 3.4. A semi-logarithmic I/U curve of such a measured diode can be seen in Figure 80a.

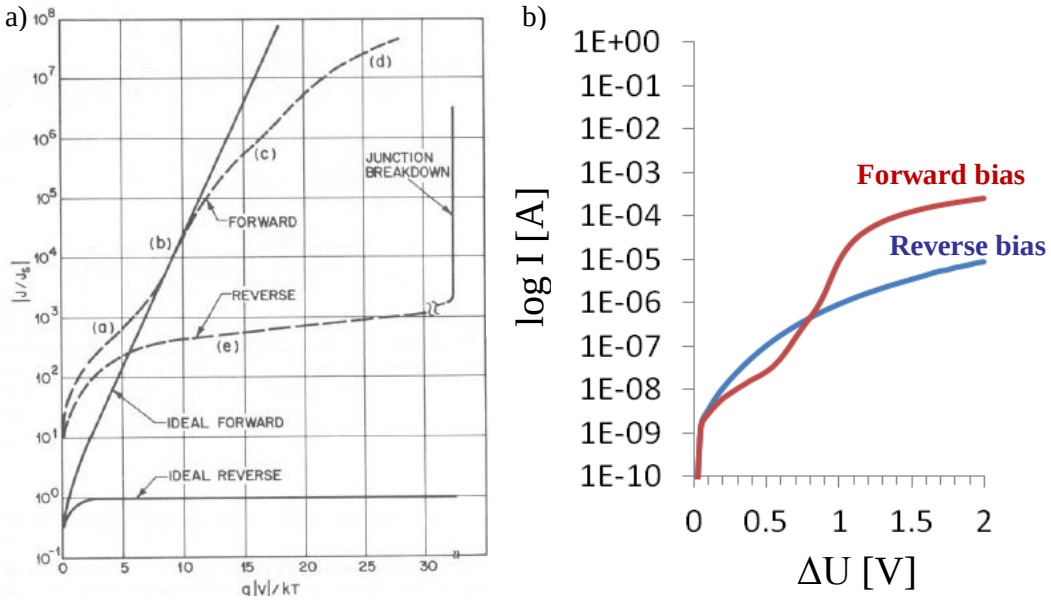

Figure 80: The semi-logarithmic I/U diagram pn-diodes with forward bias and reverse bias:

a) pn-diode curve from literature [54]

b) In-situ grown pn-diode

The most striking differences in the curve are due to:

(a) Generation-recombination-currents

(b) Diffusion currents

(c) Injection currents

(d) Serial resistance

(e) Generation-recombination-leakage-currents

The I/U diagram shows clearly the behaviour of a real pn-diode according to Figure 80b [54] with the influences of generation-recombination-currents (a), diffusion currents (b), injection currents (c) and serial resistance (d) for the forward bias. The increase in the reverse bias can be attributed to generation-recombination-leakage-currents (e), which is comparably high in case of the in-situ pn-diode. The initial expectations of creating a tunnel- or Esaki-diode with an atomic sharp interface via the VLS-mechanism

did not occur, which is most likely due to the high diffusion rates at a growth temperature of 800°C, which created a very gentle pn-gradient.

An analysis of the emission coefficient showed an unusual value of around 7, what is too far off from the expected 1 to 4 for a usual Si-diode. The high current in reverse direction supports the assumption of a very gentle gradient, what renders the Schockley model invalid for this specific diode.

5 Conclusion

NWs are seen as an ideal candidate for integration in future micro- and nano-scale electronic devices by increasing packaging density, adjusting properties to applications and growing structures in desired locations. Of course a well understood growth mechanism and a suitable precursor, along with adjusted process parameters, are necessary to achieve such devices.

Hence, this thesis focuses on the capabilities of OCTS to grow Si-NWs and investigation of their electrical and crystalline properties. To achieve these goals the influence of temperature, H_2 addition, flow rates, sample preparation, alternative catalysts and doping agents were examined. The epitaxial NWs achieved this way were subsequently characterized for their properties involving SEM, I/U measurements and TEM investigation, including crystallographic analysis. A selected portion of these NWs were also used to create an in-situ grown pn-diode.

The second chapter covers the theoretical aspects of this work, presenting basic understanding for electrical and TEM characterization, but also providing a thorough understanding of the VLS-mechanism and relevant subject, like precursor properties, phase diagrams and epitaxy. The NW growth is influenced not only by easily accessible parameters like temperature and total pressure, but also by partial pressure of the precursor, amount of H_2, catalyst, pre growth tempering and age of the used quartz glass tube of the reactor. The epitaxy of the NWs, which was an important goal of this thesis, also depends on very different parameters depending on the used dopant and kind of catalyst. Furthermore NWs do not grow necessarily via a VLS mechanism, but also by the VSS mechanism, thus requiring good understanding of phase diagrams, surface energies and utilization of those.

Electric properties of Si-NWs can be explained by the work of Schottky, although surface atoms play an increasing role considering a NWs tiny size. Surface charges can profoundly decrease a NW's conducting area by forming a depleted shell near the nanowire surface resulting in a reduced charge-carrying area and therefore alter a NW's electrical properties. The effects of doping agent on growth and of course on electrical properties are also basically explained in this section. B is not only a popular dopant, but alters the growth behaviour severely by accelerating precursor decomposition, while P decelerates NW growth by occupying adsorption spots on the catalyst.

The theoretical part concludes by providing a basic understanding of analysing and interpreting a Si Sample by TEM investigation. This incorporates basic setup of a TEM,

as well as Bragg's law, the importance of the Ewald sphere and examples for thickness contours and the most common defects encountered in Si. The indicating of a diffraction pattern is also basically explained.

Chapter three explains the experimental setup and sample preparation of Si-NW growth conducted in this thesis. A detailed illustration of the used hot wall furnace atmospheric pressure chemical vapor deposition is shown, accompanied by an explanation of growth sample preparation and subsequent preparing for TEM investigations. NW growth was researched at temperatures between 400°C and 900°C with different feed gases and catalysts. In later stages also doping agents were introduced into the gas flow to grow in-situ doped NWs. Samples for subsequent electrical investigation were made by removal with ultra-sonic sound and contacting with electron beam lithography. A detailed illustration and description how the in situ grown pn-diode was processed concludes the experimental part.

Chapter number four presents the results of the conducted experiments and a subsequent discussion of them.

First growth experiments with pure OCTS were conducted with Au as the catalyst and 100 He sccm as carrier gas only. Au proved itself as a very versatile catalyst as NWs were found in good quantities between 600°C and 900°C. The addition of 20 sccm H_2 had mostly negative effects on NW growth. Except for a temperature of 900°C, where NWs with a diameter up to 2 µm were encountered, only etching was observed. By tweaking growth parameters it turned out, that epitaxy could be achieved by a 30 min annealing step prior to growth at 800°C in pure He. The growth itself took place at 700°C and yielded a large share of upright NWs. An increase in OCTS partial pressure completely supressed the growth of upright NWs and only inclined ones were found. Crystallinity with no observable defect along with a [111] growth orientation was later verified by TEM investigations.

Alternative catalysts were also successfully utilized for NW growth. In all cases a flow rate of He:H_2 : 100.20 sccm was necessary to achieve the best results. Ag catalysed NWs were 100 to 200 nm in diameter and 1 to 5 µm in length grown at 800°C, while featuring an strongly facetted appearance. At 800°C, Cu catalysed NWs were yielded with diameters of 50 to 200 nm and lengths of up to 20 µm. Finally Pt yielded epitaxial NWs with about 5 µm in length and 30 to 100 nm in diameter at 900°C. Also in these cases, [111] directions were confirmed for all alternately catalysed NWs by TEM investigations, but crystallinity differed among them. Ag caused a strong tendency for

twining, Cu was incorporated during growth, which resulted in strongly tapered NWs, while Pt contrarily caused a crystal structure without observable defects. Along with these catalysts also Al, Ti and In were investigated, but successful growth was not achieved.

A special feature was produced when Ni was used as catalyst. At 900°C with a gas flow of $He:H_2$: 100:40 sccm square shaped Si-NWs were produced contrary to the usually irregular hexagonal ones. The square shape derives from the cubic structure of α-$NiSi_2$, which forces its shape onto the NW during growth. Also two different growth orientations, namely [100] and [110], were encountered on the very same sample, what depends on the thickness of the used Ni layer. The Ni layer used in this thesis cannot be expected to cover the whole sample equally, thus leading to different orientations of the initial nickelsilicide particle the NW grows from.

After growth with pure OCTS, it was also tried to add BBr_3 to the gas feed and grow in-situ p-doped NWs. In this case it proved necessary to add 20 sccm H_2 to the gas flow to improve NW growth. BBr_3 changed the growth behaviour considerably by acceleration precursor decomposition, what resulted in NWs with a thick shell of amorphous Si wrapping around a crystalline core. The amorphous shell accounted for about half of the NW's diameter in this case. This was later confirmed by TEM investigation, which also revealed a growth direction of [112]. Also the growth temperatures were shifted to lower values. NW growth was observed between 400°C and 700°C, with epitaxy achieved at 600°C. For the alternative catalysts Cu, Ni and Pt the results were far from achieving epitaxy, although NWs were achieved. In general their quantity and quality dropped considerably.

For the final grow experiments a P containing component, PCl_3, was added to the gas flow. Au again proved itself the most versatile catalyst and epitaxial NWs were achieved at 900°C with 20 sccm of H_2 added. These NWs were about 60 nm to 150 nm in diameter and up to 30 µm long and were also yielded in numerous quantities. NWs were also found at 800°C, but quality and numbers were noticeably decreased. At lower temperatures no NWs were encountered. Contrary to the experiments with BBr_3 NWs could also be grown without the addition of H_2. At temperatures of 800°C and higher successful growth could be achieved, although no epitaxy was realised.

The work is concluded by the electrical characterisation of the epitaxial NWs grown with different catalysts, including doped ones. Cu ($7.8*10^4$ Ωcm) and Ni catalysed ($1.57*10^4$ Ωcm) NWs feature the highest resistivity as both catalysts incorporate

themselves during growth and deteriorate crystal structure. Au catalysed NWs feature a resistivity of $5.96*10^{3}$ Ωcm, what is in range of values obtained in literature. Ag ($4.23*10^{3}$ Ωcm) and Pt ($9.72*10^{2}$ Ωcm) produce NWs with even lower resistivity. This is most likely due to their favorable deep level trap behaviour and good crystal structure. In subsequent experiments Au was used to grow in situ doped NWs. B doped NWs feature a resistivity of $8.62*10^{2}$ Ωcm as prepared, while annealing at 470°C for 2 min reduced resistivity to $1.98*10^{-1}$ Ωcm. The difference can be attributed to the enormous amorphous shell around the NW, which the addition of B causes to form during growth. P proved to be an even more potent dopant by reducing the NW's resistivity to $2.4*10^{-3}$ Ωcm. Comparing these values with active dopant concentrations in bulk Si, leads to $2*10^{12}$ cm^{-3}, 10^{17} cm^{-3} and $3*10^{19}$ cm^{-3} for intrinsic, B-doped and P-doped NWs respectively. Finally also an in situ doped pn diode was grown and electrically characterized. This diode featured classical behaviour and a high leakage current at the reverse bias, which is due to the extremely soft gradient at the interface.

6 References

[1] R. G. Treuting and S. M. Arnold. Orientation habits of metal whiskers. *Acta Met.*, 5, 598, 1957.

[2] R. S. Wagner and W. C. Ellis. Vapor Liquid Solid Mechanism of single crystal growth. *Appl. Phys. Lett.*, 4, 89, 1964.

[3] V. Schmidt, J. V. Wittemann, S. Senz and U. Gösele. Silicon Nanowires: A Review on Aspects of their Growth and their Electrical Properties. *Advanced Materials*, 21, 2681-2702, 2009.

[4] Y. Huang, X. Duan, Y. Cui, L. J. Lauhon, K. H. Kim and C. M. Lieber. Logic Gates and Computation from Assembled Nanowire Building Blocks. *Science*, 294, 1313, 2001.

[5] M. H. Huang, S. Mao, H. Feick, H. Yan, Y. Wu, H. Kind, E. Weber, R. Russo and P. Yang. Room-Temperature Ultraviolet Nanowire Nanolasers. *Science*, 292, 1897, 2001.

[6] B. M. Kayes, H. A. Atwater and N. S. Lewis. Comparison of the device physics principles of planar and radial p-n junction nanorod solar cells. *J. Appl. Phys.*, 97, 114302, 2005.

[7] Y. Cui, Q. Wei, H. Park and C. M. Lieber. Nanowire Nanosensors for Highly Sensitive and Selective Detection of Biological and Chemical Species. *Science*, 293, 1289, 2001.

[8] C. K. Chan, H. Peng, G. Liu, K. McIlwrath, X. F. Zhang, R. A. Huggins and Yi Cui. High-performance lithium battery anodes using silicon nanowires. *Nature Nanotechnology*, 3(31), 35, 2008.

[9] M. Valden, X. Lai and D. W. Goodman. Onset of Catalytic Activity of Gold Clusters on Titania with the Appearance of Nonmetallic Properties. *Science*, 281, 1647, 1998.

[10] Patolsky, F.; Timko, B. P.; Zheng, G.; Lieber, C. M. Nanowire-based nanoelectronic devices in the life sciences. *MRS Bull.*, 32, 142–9, 2007.

[11] C. N. R. Rao, A. Müller and A. K. Cheetham. *The Chemistry of Nanomaterials*. Wiley-VCH Verlag, 1st edition, 2004.

[12] Y. Xia, P. Yang, Y. Sun, Y. Wu, B. Mayers, B. Gates, Y. Yin, F. Kim and H. Yan. One-Dimensional Nanostructures: Synthesis, Characterization, and Applications. *Advanced Materials*, 15(5), 353-389, 2003.

[13] J. Westwater, D. P. Gosain, S. Tomiya and S. Usui. Growth of silicon nanowires via gold/silane vapor-liquid-solid reaction. *Journal of Vacuum Science and Technology B*, 15, 554-557, 1997.

[14] T. R. Hogness, T. L. Wilson and W. C. Johnson. The Thermal Decomposition of Silane. *J. Am. Che. Soc.*, 58, 108-112, 1936.

[15] H. Pan, S. Lim, C. Poh, H. Sun, X. Wu, Y. Feng and J. Lin. Growth of Si nanowires by thermal evaporation. *Nanotechnology*, 16, 417-421, 2005.

[16] J.C. Harmand, M. Tchernycheva, G. Patriarche, L. Travers, F. Glas and G. Cirlin. GaAs nanowires formed by Au-assisted molecular beam epitaxy: Effect of growth temperature. *Journal of Crystal growth*, 301-302, 853-856, 2007.

[17] N. Wang, Y.H. Tang, Y.F. Zhang, C.S. Lee and S.T. Lee. Nucleation and growth of Si nanowires from silicon oxide. *Physical Review*, B 58, R16024, 1998.

[18] A. T. Heitsch, D. D. Fanfair, H.-Y. Tuan and Brian A. Korgel. Solution−Liquid−Solid (SLS) Growth of Silicon Nanowires. *J. Am. Che. Soc.*, 130, 5436-7, 2008.

[19] H. Fang, J. Wu, Y. Zhao and J Zhu. Silver catalysis in the fabrication of silicon nanowire arrays. *Nanotechnology*, 17(15), 3768, 2006.

[20] L. Brus. Luminescence of Silicon Materials: Chains, Sheets, Nanocrystals, Nanowires, Microcrystals, and Porous Silicon. *J. Phys. Chem.*, 98, 3575, 1994.

[21] H. Yorikawa, H. Uchida and S. Murmatsu. Energy gap of nanoscale Si rods. *J. Appl. Phys.*, 79, 3619, 1996.

[22] J.L. Mozos, E. Machado, E. Hernandez and P. Ordejon. Nanotubes and nanowires: the effect of impurities and defects on their electronic properties. International Journal of Nanotechnology, 2, 114, 2005.

[23] Yi. Cui, L. J. Lauhon, M. S. Gudiksen, J. Wang and C. M. Lieber. Diameter-controlled synthesis of single-crystal silicon nanowires. *Applied Physics Letters* 78, 2214, 2001.

[24] W. I. Park, G. Zheng, X. Jiang, B. Tian and C. M. Lieber. Controlled Synthesis of Millimeter-Long Silicon Nanowires with Uniform Electronic Properties. *Nanoletters* 8, 3004-3009, 2008.

[25] A. I. Hochbaum, F. Rong, H. Rongrui and Y. Peidong. Controlled Growth of Si Nanowire Arrays for Device Integration. *Nanoletters* 5, 457-460, 2005.

[26] V. Schmidt, H. Riel, S. Senz, S. Karg, W. Riess and U. Gösele. Realization of a Silicon Nanowire Vertical Surround-Gate Field-Effect Transistor. *Small*, 2, 85-88, 2006.

[27] M. T. Björk, J. Knoch, H. Schmidt, H. Riel and W. Riess. Silicon nanowire tunneling field-effect transistors. *Appl. Phys. Lett.*, 92**,** 193504, 2008.

[28] K.-K. Lew, L. Pan, T. E. Bogart, S. M. Dilts, E. C. Dickey, M. Redwing, Y. F. Wang, M. Cabassi, T. S. Mayer and S. W. Novak. Structural and electrical properties of trimethylboron-doped silicon nanowires. *Appl. Phys. Lett.*, 85**,** 3101, 2004.

[29] H. Schmid, M. T. Björk, J. Knoch, S. Karg, H. Riel and W. Riess. Doping Limits of Grown in situ Doped Silicon Nanowires Using Phosphine. *Nano Lett.*, 9(1), 173-177, 2009.

[30] P. Xie, Y. Hu, Y. Fang, J. Huang and C. M. Lieber. Diameter-dependent dopant location in silicon and germanium nanowires. *PNAS*, 106(36), 15254-8, 2009.

[31] Y. Cui, X. Duan, J. Hu and C. M. Lieber. Doping and Electrical Transport in Silicon Nanowires. *J. Phys. Chem. B* 104, 22, 5213-5216, 2000.

[32] H. Suzuki, H. Araki, M. Tosa and T. Noda. Electrical conductivity measurement of silicon wire prepared by CVD. *Chemical Physics Letters*, 468, 211-215, 2009.

[33] J.-Y. Yu, S.-W. Chung and J. R. Heath. Silicon Nanowires: Preparation, Device Fabrication, and Transport Properties. *J. Phys. Chem. B* 104, 11864-11870, 2000.

[34] D. P. Yu, Y. J. Xing, Q. L. Hang, H. F. Yan, J. Xu, Z. H. Xi and S.Q. Feng. Controlled growth of oriented amorphous silicon nanowires via a solid-liquidsolid (SLS) mechanism. *Physica E*, 9(2), 305-309, 2001.

[35] J. D. Holmes, K. P. Johnston, R. C. Doty, and B. A. Korgel. Control of Thickness and Orientation of Solution-Grown Silicon Nanowires. *Science*, 287(5457), 1471-1473, 2000.

[36] T. I. Kamins, R. S. Williams, Y. Chen, Y. L. Chang, and Y. A. Chang. Chemical vapor deposition of Si nanowires nucleated by $TiSi_2$ islands on Si. *Appl. Phys. Lett.*, 76, 562-564, 2000.

[37] R. Q. Zhang, Y. Lifshitz, and S. T. Lee. Oxide-Assisted Growth of Semiconducting Nanowires. *Advanced Materials*, 15(7-8), 635-640, 2003.

[38] V. A. Nebol'sin and A. A. Shchetinin. Role of Surface Energy in the Vapor-Liquid-Solid Growth of Silicon. *Inorg. Mater.* 39, 899-903, 2003.

[39] Y. Wang, V. Schmidt, S. Senz and U. Gösele. Epitaxial growth of silicon nanowires using an aluminium catalyst. *nature nanotechnology* Vol. 1, 186-189, 2006.

[40] Y. Miyamoto and M. Hirata. Role of Agents in Filamentary Growth of Amorphous Silicon. *Jpn. J. Appl. Phys.* 15, 1159-60, 1976.

[41] R. S.Wagner, W. C. Ellis, K. A. Jackson und S. M. Arnold. Study of the filamentary growth of silicon crystals from the vapor. *J. Appl. Phys.* 35(10), 2993–3000, 1964.

[42] R. S. Wagner and W. C. Ellis. Vapor-Liquid-Solid Mechanism of Single Crystal Growth. *Appl. Phys. Lett.* 4, 89-90, 1964.

[43] V. Schmidt, S. Senz and U. Gösele. UHV chemical vapour deposition of silicon nanowires. *Z. Metallkd.* 96, 427-428, 2005.

[44] M. K. Sunkara and S. Sharma. Direct synthesis of single-crystalline silicon nanowires using molten gallium and silane plasma. *Nanotechnology* 15, 130-134, 2004.

[45] S. Sharma, T. I. Kamins and R. S. Williams. Diameter control of Ti-catalysed silicon nanowires. *Journal of Crystal Growth* 267, 613-618, 2004.

[46] R. R. He, D. Gao, R. Fan, A. I. Hochbaum, C. Carraro, R. Maboudian and P. D. Yang. Si Nanowire Bridges in Microtrenches: Integration of Growth into Device Fabrication. *Advanced Materials* 17, 2098-2102, 2005.

[47] M. H. Huang, Y. Wu, H. Feick, N. Tran, E. Weber, P. Yang. Catalytic Growth of Zinc Oxide Nanowires by Vapor Transport. *Advanced Materials* 13, No. 2, 113–116, 2001.

[48] J. Nordiek. Schmelzen von Clustern: Ein Beispiel für die statistische Thermodynamik kleiner Systeme. Albert-Ludwigs-Universitaet Freiburg im Breisgau, Muenchen, 1999.

[49] F. F. Abraham. *Homogenous nucleation theory.* Academic Press NY, 1974.

[50] N. Wang, Y. Cai and R. Q. Zhang. Growth of nanowires. *Materials Science and Engineering R* 60, 1-51, 2008.

[51] P. W. Atkins. *Physikalische Chemie*. *WILEY-VCH*, 3rd edition, 2001.

[52] W. J. Moore. Grundlagen der physikalischen Chemie. *De Gruyter*, 1990.

[53] T. B. Massalski. *Binary alloy phase diagrams.* American Society for Metals, 1st edition, 1986.

[54] M. S. Sze. *Physics of semiconductor devices.* John Wiley and Sons, 2nd edition, 1981.

[55] O. Madelung, U. Rössler and M. Schulz. Landolt-*Börnstein - Group III Condensed Matter, Volume: 41A2a, Impurities and Defects in Group IV Elements, IV-IV and III-V Compounds. Part a: Group IV Elements*. Springer- Verlag, 2002.

[56] Y. Wu, H. Yan, M. Huang, B. Messer, J. H. Song and P. Yang. Inorganic Semiconductor Nanowires: Rational Growth, Assembly, and Novel Properties. *Chem. Eur. J.* 8, No. 6, 1261-1268, 2002.

[57] A. Lugstein, M. Steinmair, Y. J. Hyun, G. Hauer, P. Pongratz and E. Bertagnolli. Pressure-Induced Orientation Control of the Growth of Epitaxial Silicon Nanowires. *Nanoletters* Vol. 8, No. 8, 2310-2314, 2008.

[58] H. Schmid, M. T. Bjork, J. Knoch, H. Riel, W. Riess, P. Rice and T. Topuria. Patterned epitaxial vapor-liquid-solid growth of silicon nanowires on Si(111) using silane. *J. Appl. Phys.* 103, 024304-7, 2008.

[59] V. Schmidt, S. Senz, U. Gösele. Diameter-Dependent Growth Direction of Epitaxial Silicon Nanowires. *Nanoletters* Vol. 5, No. 5, 931-935, 2005.

[60] S. A. Fortuna and X. Li. Metal-catalysed semiconductor nanowires: a review on the control of growth directions. *Semicond. Sci. Technol.* 25, 024005, 2010.

[61] A. Lugstein, Y. J. Hyun, M. Steinmair, B. Dielacher, G. Hauer and E. Bertagnolli. Some aspects of substrate pretreatment for epitaxial Si nanowire growth. *Nanotechnology* 19, 485606, 2008.

[62] B. Tian, P. Xie, T. J. Kempa, D. C. Bell and C. M. Lieber. Single crystalline kinked semiconductor nanowire superstructures. *Nature Nanotechnology* 4, 824 – 829, 2009.

[63] S. Ge, K. Jiang, X. Lu, Y. Chen, R. Wang and S. Fan. Orientation-controlled growth of single crystal silicon-nanowire arrays. *Adv. Mater.* 17, 56-61, 2005.

[64] K. A. Dick, K. Deppert, L. Samuelson, L. R. Wallenberg and F. M. Ross. Control of GaP and GaAs nanowire morphology through particle and substrate chemical modification. *Nanoletters* 8, No. 11, 4087-4091, 2008.

[65] M. K. Sunkara and S. Sharma. Direct synthesis of single-crystalline silicon nanowires using molten gallium and silane plasma. *Nanotechnology* 15, 130-134, 2004.

[66] T. Baron, M. Gordon, F. Dhalluin, C. Ternon, P. Ferret and P. Gentile. Si nanowire growth and characterization using a microelectronics-compatible catalyst: PtSi. *Applied Physics Letters* 2006, 89, 233111.

[67] J. V. Wittemann, W. Münchgesang, S. Senz and V. Schmidt. Silver catalysed ultrathin silicon nanowires grown by low-temperature chemical-vapor-deposition. *Journal of Applied Physics* 107, 096105, 2010.

[68] J. Arbiol, B. Kalache, P. R. i Cabarrocas, J. R. Morante and A. F. i Morral. Influence of Cu as a catalyst on the properties of silicon nanowires synthesized by the vapour–solid–solid mechanism. *Nanotechnology* 18, 305606, 2007.

[69] R. Walsh. Bond Dissociation Energy Values in Silicon Containing Compounds and Some of Their Implications. Acc. Chem. Res.**,** 14, 246-252, 1981.

[70] Y. S. Ezhov, E. P. Simonenko and V. G. Svast'yanov. The Thermodynamic Properties and Thermal Decomposition of Octachlorotrisilane Si3Cl8. *Russian Journal of Physical Chemistry A*, 83(2), 179-181, 2009.

[71] G. Martin. Researches on silicon compounds. Part VI. Preparation of silicon tetrachloride, disilicon hexachloride, and the higher chlorides of silicon by the action of chlorine on 50 per cent. Ferrosilicon, together with a discussion on their mode of formation *J. chem. Soc.*, 105, 2936, 1914.

[72] F. Iacopi, P. M. Vereecken, M. Schaekers, N. Caymax, N. Moelans, B. Blanpain, O. Richard, C. Detavernier and H. Griffiths. Plasma-enhanced chemical vapour deposition growth of Si nanowires with low melting point metal catalysts: an effective alternative to Au-mediated growth. *Nanotechnology*, 18, 505307, 2007.

[73] P. Das Kanungo, N. Zakharov, J. Bauer, O. Breitenstein, P. Werner und U. Gösele. Controlled in situ boron doping of short silicon nanowires grown by molecular beam epitaxy. *Appl. Phys. Lett.*, 92, 263107-9, 2008.

[74] Y. H. Tang**,** T. K. Sham**,** A. Jürgensen**,** Y. F. Hu**,** C. S. Lee and S. T. Lee**.** Phosphorus-doped silicon nanowires studied by near edge x-ray absorption fine structure spectroscopy. *Appl. Phys. Lett.*, 80, 3709-11, 2002.

[75] L. J. Lauhon, M. S. Gudiksen, D. Wang and C. M. Lieber. Epitaxial core–shell and core–multishell nanowire heterostructures. *Nature* 420, 57-61, 2002.

[76] A. J. Learn and D. W. Foster. Deposition and electrical properties of in situ phosphorus- doped silicon films formed by low-pressure chemical vapor deposition. *J. Appl. Phys.* 61 (5), 1898-1904, 1987.

[77] E. Koren, N. Berkovitch and Y. Rosenwaks. Measurement of Active Dopant Distribution
and Diffusion in Individual Silicon Nanowires. *Nano Letter*, 10, 1163-67, 2010.

[78] H. Peelaers, B. Partoens and F. M. Peeters. Formation and Segregation Energies of B and P Doped and BP Codoped Silicon Nanowires. *Nano Lette,* 6, 2781, 2006.

[79] W. Schottky. Zur Halbleitertheorie der Sperrschicht- und Spitzengleichrichter. *Zeitschrift für Physik*, 113(5-6), 367–414, 1939.

[80] A. Dimoulas, P. Tsipas and A. Sotiropoulos. Fermi-level pinning and charge neutrality level in germanium. *Appl. Phys. Lett.*, 89:252110–252112, 2006.

[81] D. Kuzum, K. Martens, T. Krishnamohan, and K. C. Saraswat. Characteristics of surface states and charge neutrality level in Ge. *Appl. Phys. Lett.*, 95(25), 252101-252101, 2009.

[82] R. S. Muller and T. I. Kamins. *Device Electronics for Integrated Circuits*. John Wiley and Sons, 1970.

[83] S. Wolf and R. N. Tauber. *Silicon Processing for the VLSI Era, vol. 1*, Sunset Beach, CA: Lattice Press, p. 289, 2000.

[84] S. Ingole, P. Manandhar, S. B. Chikkannanavar, E. A. Akhadov and S. T. Picraux. Charge Transport Characteristics in Boron-Doped Silicon Nanowires. *IEEE Transactions on Electron Devices* 55(11), 2931-2938, 2008.

[85] V. Schmidt, S. Senz and U. Gösele. Influence of the Si/SiO_2 interface on the charge carrier density of Si nanowires. Appl. Phys. A 86, 187–191, 2007.

[86] T. I. Kamins, S. Sharma, A. A. Yasseri, Z. Li and J. Straznicky. Metal-catalysed, bridging nanowires as vapour sensors and concept for their use in a sensor system. *Nanotechnology* 17, 291, 2006.

[87] S. M. Eichfeld, T.-T. Ho, C. M. Eichfeld, A. Cranmer, S. E. Mohney, T. S. Mayer and J. M. Redwing. Resistivity measurements of intentionally and unintentionally template-grown doped silicon nanowire arrays. *Nanotechnology* 18, 315201-315206, 2007.

[88] S. Koo, M.D. Edelstein, Q. Li, C.A. Richter and E.M. Vogel. *Silico Nanowires as enhancement-mode schottky barrier Field-Effect Transistors. Nanotechnology*, 16:1482–1485, 2005.

[89] D. B. Williams and C. B. Carter. *Transmission Electron Microscopy – A Textbook for Material Science*. Springer Science+Business Media, LLC, 2nd edition, 2009.

[90] http://www.nanolabtechnologies.com/fe-tem-stem. Last visited 07.11.2013.

[91] E. I. Givargizov. Fundamental aspects of VLS growth. *Journal of Crystal Growth*, 31(20), 1975.

[92] S. Y. Li, C. Y. Lee and T. Y. Tseng. Copper-catalysed ZnO nanowires on silicon (100) grown by vapor–liquid–solid process. *Journal of Crystal Growth,* 247, 357–362, 2003.

[93] G.Chen, L.Wang, X. Sheng, H. Liu, X. Pi, Y. Zhang, D. Li and D. Yang. Growth of In_2O_3 Nanowires Catalysed by Cu via a Solid–Liquid–Solid Mechanism. *Nanoscale Research Letters*, 5, 898-903, 2010.

[94] C.-Y. Wen, M. C. Reuter, J. Tersoff, E. A. Stach, F. M. Ross. Structure, Growth Kinetics, and Ledge Flow during Vapor-Solid-Solid Growth of Copper-Catalysed Silicon Nanowires. *Nano Lett.*, *10*, 514-519, 2010.

[95] R. S.Wagner and W. C. Ellis. The Vapor- Liquid-Solid Mechanism of Crystal Growth and Its Application to Silicon. *Trans. Met. Soc. AIME, 233*, 1053, 1965.

[96] V. A. Nebol'sin, A. A. Shchetinin, A. A. Dolgachev, V. V. Korneeva. Effect of the Nature of the Metal Solvent on the Vapor-Liquid-Solid Growth Rate of Silicon Whiskers. *Inorg. Mater.*, *41*, 1256, 2005.

[97] F. Geiger, C. A. Busse, R. I. Loehrke. The vapor pressure of indium, silver, gallium, copper, tin, and gold between 0.1 and 3.0 bar. *Int. J. Thermophys.*, *8*, 425, 1987.

[98] Y. Tatsumi, M. Shigi, M. J. Hirata. Visual Observation of Whisker Growth in Amorphous Silicon. *Phys. Soc. Jpn.*, *45*, 703, 1978.

[99] L. Weber. Equilibrium solid solubility of silicon in silver. *Metall. Mater. Trans. A*, *33A*, 1145, 2002.

[100] E. C. Garnett, W. Liang, P.Yang. Growth and Electrical Characteristics of Platinum-Nanoparticle- Catalysed Silicon Nanowires. *Adv. Mater., 19,* 2946–2950, 2007.

[101] P. K. Sekhar, S. N. Sambandam, D.K. Sood, S. Bhansali. Selective growth of silica nanowires in silicon catalysed by Pt thin film. *Nanotechnology*, 17, 4606–4613, 2006.

[102] A. Lugstein, A. M. Andrews, M. Steinmair, Y.-J. Hyun, E. Bertagnolli, M. Weil, P. Pongratz, M. Schramböck, T. Roch, G. Strasser. Growth of branched single-crystalline GaAs whiskers on Si nanowire trunks. *Nanotechnology*, *18,* 355306, 2007.

[103] B. A. Wacaser, M. C. Reuter, M. M. Khayyat, C.-Y.Wen, R. Haight, S. Guha, F. M. Ross. Growth System, Structure, and Doping of Aluminum-Seeded Epitaxial Silicon Nanowires. *Nano Lett.*, 9, 2009.

[104] L.Yu, B. O'Donnell, P.-J. Alet, S. Conesa-Boj, F. Peiro, J. Arbiol, and P. R. i Cabarrocas. Plasma-enhanced low temperature growth of silicon nanowires and hierarchical structures by using tin and indium catalysts. *Nanotechnology*, 20, 225604, 2009.

[105] Z. W. Wang, Z. Y. Li. Structures and Energetics of Indium-Catalysed Silicon Nanowires. *Nano Lett.*, Vol. 9, No. 4, 2009.

[106] H. Fujitani, S. Asano. Full-potential total-energy investigation on the lattice relaxation at the two types of NiSi2/Si(111) interface. *Physical Review B*, 51, 18019-18021, 1995.

[107] S.K. Ghandhi. VLSI Fabrication Principles: *Silicon and Gallium Arsenide*, 1st edition, Wiley, New York 1983, Ch 1.

[108] C. V. Ciobanu, T.-L. Chan, F.-C. Chuang, N. Lu, C.-Z. Wang, K.-M. Ho. Magic Structures of H-Passivated 110 Silicon Nanowires. *Nanoletters*, 6(2), 277-281, 2006.

[109] A.B. Greytak, L.J. Lauhon, M.S. Gudiksen, C.M. Lieber. Growth and transport properties of complementary germanium nanowire field-effect transistors. *Appl. Phys. Lett.*, 84, 4176, 2004.

[110] K.A. Dick, K. Deppert, T. Martensson, B. Mandl, L. Samuelson, W. Seifert. Failure of the Vapor-Liquid-Solid Mechanism in Au-Assisted MOVPE Growth of InAs Nanowires. *Nanoletters*, 5, 761, 2005.

[111] A. I. Persson, M. W. Larsson, S. Stenström, B. J. Ohlsson, L. Samuelson, L. R. Wallenberg. Solid-phase diffusion mechanism for GaAs nanowire growth. *Nat. Mater.*, 3, 677, 2004.

[112] A. Colli, S. Hofmann, A.C. Ferrari, C. Ducati, F. Martelli, S. Rubini, S. Cabrini, A. Franciosi, *J.* Robertson. Low-temperature synthesis of ZnSe nanowires and nanosaws by catalyst-assisted molecular-beam epitaxy. *Appl. Phys. Lett.*, 86, 153 103, 2005.

[113] T. I. Kamins, R. S. Williams, D. P. Basile, T. Hesjedal, J. S. Harris. Ti-catalysed Si nanowires by chemical vapor deposition: Microscopy and growth mechanisms. *J. Appl. Phys.*, 89, 1008, 2001.

[114] R. Q. Zhang, Y. Lifshitz, D. D. D. Ma, Th. Frauenheim, S. T. Lee, S. Y. Yong. Structures and energetics of hydrogen-terminated silicon nanowire surfaces. *The Journal of Chemical Physics,* 123, 144703, 2005.

[115] R. T. Tung, J. M. Gibson, J. M. Poate. Formation of Ultrathin Single-Crystal Silicide Films on Si: Surface and Interfacial Stabilization of Si-NiSi2 Epitaxial Structures. *Physical Review Letters,* 50(6), 429, 1983.

[116] D. Briand, M. Sarret, K. Kis-Sion, T. Mohammed-Brahim, P. Duverneuil. In situ doping of silicon deposited by LPCVD: pressure influence on dopant incorporation mechanisms. *Semiconductor Science and Technology*, 14, 173-180, 1999.

[117] M. Cuscunà, A. Convertino, L. Mariucci, G. Fortunato, L. Felisari, G. Nicotra, C. Spinella, A. Pecora, F. Martelli. Low-temperature, self-catalysed growth of Si nanowires. *Nanotechnology,* 21, 255601, 2010.

[118] S. Krylyuk, A. V. Davydov , I. Levin. Tapering Control of Si Nanowires Grown from $SiCl_4$ at Reduced Pressure. *ACS Nano,* 5 (1), 656–664, 2011.

[119] W.-F. Wu, K.-L. Ou, C.-P. Chou and C.-C. Wu. Effects of Nitrogen Plasma Treatment on Tantalum Diffusion Barriers in Copper Metallization. *Journal of The Electrochemical Society,* 150(2), G83-G89, 2003.

[120] S. Zhang, E. R. Hemesath, D. E. Perea, E. Wijaya, J. L. Lensch-Falk, L. J. Lauhon. Relative Influence of Surface States and Bulk Impurities on the Electrical Properties of Ge Nanowires. *Nano Letters,* 9(9), 3268-3274, 2009.

[121] D.R. Khanal, J. Wu. Gate coupling and charge distribution in Nanowire Field Effect Transistors. *Nano Letters,* 7(9):2778–2783, 2007.

[122] K. Byon, D. Tham, J.E. Fischer, A.T. Johnson. Systematic study of contact annealing:Ambipolar silicon Nanowire transistor with improved performance. Applied Physics Letters, 90:143513–143515, 2007.

[123] M. Jang, M. Jun, T. Zyung. Effective mobility characteristics of platinum-silicided p-type Schottky

barrier metal-oxide-semiconductor field-effect transistor. J. Vac. Sci. Technol. B 28, 799-801, 2010.

List of own publications

a) Journal Publications

1.) Subeutectic Synthesis of Epitaxial Si-NWs with Diverse Catalysts Using a Novel Si Precursor

W. Molnar, A. Lugstein, P. Pongratz, N. Auner, C. Bauch, and E. Bertagnolli

in Nano Letters 2010, 10(10), p. 3957–3961.

2.) Synthesis and electrical characterization of intrinsic and in situ doped Si nanowires using a novel precursor

Wolfgang Molnar, Alois Lugstein, Tomasz Wojcik, Peter Pongratz, Norbert Auner, Christian Bauch, Emmerich Bertagnolli

in Beilstein J. Nanotechnol. 2012, 3, 564–569.

3.) A General Approach toward Shape-Controlled Synthesis of Silicon Nanowires

W. Molnar, A. Lugstein, P. Pongratz, M. Seyring, M. Rettenmayr, C. Borschel, C. Ronning, N. Auner, C. Bauch, and E. Bertagnolli

in Nano Letters 2013, 13 (1), p. 21–25.

b) Conference Contributions

1.) Junior Scientist Conference 2010 7.-9.04. 2010 at Vienna University of Technology

Poster presentation

Si-NW synthesis by using octachlorotrisilane as novel precursor

2.) 2011 MRS Fall Meeting 28.11-2.12. 2011 in Boston

Oral presentation

Synthesis and electrical characterisation of APCVD-grown epitaxial SiNWs by using OCTS as a novel precursor

3.) Informationstagung Mikroelektronik ME12 23.-24.2012 in Vienna

Oral presentation

Synthesis and electrical characterization of intrinsic and in-situ doped Si nanowires using Si_3Cl_8 as precursor

Curriculum Vitae

DI Wolfgang Molnar

Date of Birth: 28.02.1983

Place of Birth: Oberwart

Nationality: Austria

Marital status: single

Education:

01/2009 Master Thesis: *Korrelation zwischen fraktographisch ermittelten Gefügekenngrößen und Eigenschaften von Sinterstahl.*

09/02 – 01/09 Studies in technical chemistry at TU Vienna

09/93 – 07/01 BG/BRG/BORG Oberschützen

09/89 – 07/93 Elementary school Oberwart